X-ray and Gamma-ray Emission Properties of Pulsars Detected by the *Fermi Gamma-ray Space Telescope*

Yoshikazu KANAI

Doctoral Thesis

Department of Particle-, Nuclear-, and Astro-Physics,
Graduate School of Science and Engineering,
Tokyo Institute of Technology

March, 2010

Abstract

Recent observations with the Large Area Telescope (LAT) onboard *Fermi Gamma-ray Space Telescope* have shown that pulsars are the primary population found along the Milky Way in the gamma-ray regime from 20 MeV to 300 GeV. The LAT has discovered 24 new pulsars only with the gamma-ray data. As most of them lack radio emission, they look similar to a peculiar gamma-ray pulsar named Geminga, whose radio emission has not been confirmed. Our question is that radio-selected pulsars (discovered in the radio band first) and gamma-selected pulsars (discovered in the gamma-ray band first) belong to the same population or not. A number of gamma-ray pulsars brought about by the *Fermi* LAT allow us the first survey to search for clues to answer the above question.

Since the gamma-selected pulsars cannot be seen in the radio wavelengths, X-ray observations should play a key role in their multi-wavelength studies. In this study, therefore, a survey is conducted with X-ray and gamma-ray observations. X-ray observations with *Suzaku* have been performed for 9 gamma-selected pulsars and a radio-selected pulsar recently discovered. Plausible X-ray counterparts have been found for all those sources. In addition to the *Suzaku* data, archival data of *XMM-Newton*, *Chandra* and the *Fermi* LAT have been systematically analyzed. All X-ray spectra can be modeled with featureless spectral functions, i.e. an absorbed power-law or that with a blackbody component. Gamma-ray spectra are represented with a power-law function with an exponential cutoff at a few GeV. We have discovered spectral parameters (X-ray and gamma-ray photon indices and the gamma-ray cutoff energies) vary with the spin-down luminosity. These trends can be explained within the framework of the "outer gap" emission model. We also have found that their X-ray luminosities have a strong correlation with the spin-down luminosities. Both the radio- and gamma-selected pulsars well follow the same relation. On the other hand, the gamma-ray luminosities have a large dispersion and show no correlation with the spin-down luminosities, which suggests that the X-ray emission is much less beamed than the gamma-ray emission.

We also investigate if these two groups of pulsars follow the same distributions of physical parameters that are derived from the rotation period and the period derivative. As a result, they follow almost the same distributions but the averages are slightly different; gamma-selected pulsars have lower spin-down luminosities and a larger characteristic ages on average. We have a candidate explanation on this result that a gamma-ray beam becomes wider with the pulsar spin-down, which is supported by a theoretical calculation. Our results can give suggestions on the evolution of gamma-ray beams.

As a conclusion, we find no evidence implying that radio-selected pulsars and gamma-selected pulsars belong to different populations.

Contents

List of Figures

List of Tables

Chapter 1

Introduction

The discovery of a pulsar by Bell and Hewish in 1968 [1] gave the first observational proof for existence of neutron stars, which had been proposed soon after the discovery of neutrons [2]. Pulsars are rapidly rotating magnetized neutron stars and, therefore, are enormously powerful particle accelerators in which particles can be accelerated along the magnetic field line up to $\sim 10^{12}$ eV [3]. Accelerated particles produce synchrotron emission in a very limited region near the magnetic pole. The emission has a narrow conical geometry co-aligned with the magnetic dipole axis. Since the magnetic dipole is inclined from the spin axis and the narrow emission beam crosses our line of sight every rotation period, a pulsar looks like a "lighthouse" in the space.

A significant fraction of pulsars has been discovered in radio observations but some pulsars also can be observed in the X-ray and gamma-ray bands. Especially in the gamma-ray band, the Energetic Gamma Ray Experiment Telescope (EGRET) onboard *Compton Gamma Ray Observatory* (*CGRO*) detected gamma-ray pulsations from six pulsars in the energy range of 20 MeV – 30 GeV [4]. While five pulsars out of six had been detected in the radio wavelengths before the gamma-ray detections, the other one, called Geminga pulsar, had long been known as a very bright unidentified gamma-ray source since its first detection in 1975 [5].

In the EGRET era, the primary candidate as the X-ray counterpart of Geminga was found to pulsate with the spin period of 237 ms by *Röentgen Satellite* (*ROSAT*) observations [6]. Succeeding gamma-ray timing analysis utilizing the reported ephemeris showed that Geminga is also pulsating in the gamma-ray band [7]. In 1997, the first detection of pulsed radio emission was reported where the flux density largely varies within 5 – 500 mJy at 102.5 MHz [8]. Subsequent radio observations, however, failed in detecting radio emission [9, 10, 11]. Therefore, Geminga has been commonly considered as a unique "radio-quiet" pulsar until the launch of *Fermi Gamma-ray Space Telescope* (*Fermi*) in

2008.

The Large Area Telescope (LAT) onboard *Fermi* has detected 55 gamma-ray pulsars as of December 2009 thanks to its unprecedented sensitivity [12, 13, 14]. Surprisingly there are 24 new pulsars discovered using only the LAT data out of 55 pulsars while the others including Geminga were detected using known ephemerides. Radio pulsed emission have been detected in follow-up radio observations from only 3 out of 24 new pulsars and moreover the detected emissions are faint [15, 16]. These pulsars first discovered by gamma-ray observation including Geminga are called gamma-ray−selected (or gamma-selected in short) pulsars and the radio pulsars with gamma-ray pulsation are called radio-selected pulsars.

Here a simple question must be raised: Do the gamma-selected pulsars and the radio-selected pulsars belong to different populations? A emission model of pulsars called outer gap model [17], which is currently most successful, can explain that they are completely of the same population and their difference is caused by the viewing angle; observers are just missing the narrow radio beams for gamma-selected pulsars. There is no observational results answering this prediction because we had only Geminga as a unique sample of the gamma-selected pulsar in the EGRET era. Now the *Fermi* LAT has significantly increased the number of samples to 25. Together with 21 radio-selected pulsars, the larger number of samples may allow us to perform a systematic survey of gamma-ray pulsars.

Since radio observations are of limited use to study gamma-selected pulsars, we performed X-ray observations for some of the new gamma-selected pulsars utilizing *Suzaku*. The results from *Suzaku* observations and analysis of archival data with *XMM-Newton*, *Chandra* and *Fermi* LAT are presented and discussed in this work.

In chapter 2, theoretical background of pulsar physics and historical observation results are shown. In chapter 3, observatories and their onboard instruments utilizing in this study are briefly summarized. Dataset, analysis methods and the results are presented in chapter 4 and 5. The obtained results are discussed in chapter 6 and we give our conclusion in chapter 7.

Chapter 2

Review

2.1 Neutron stars

A neutron star is a compact core left behind a supernova explosion of a massive main sequence star heavier than $8M_\odot$. After exhaustion of the hydrogen fuel at the center of a star, there is a core of helium ash. Since energies are no longer produced from nuclear fusions, the core starts the gravitational contraction and the inner temperature arises. Helium start to burn at 2×10^8 K and heavier elements start to burn at higher temperatures. Stars with mass of $8 - 12M_\odot$ end up a onion-like structure with a core made of oxygen, neon and magnesium and layers of carbon and helium. In the case of $> 12M_\odot$ stars, at last, the inner temperature becomes $> 3 \times 10^9$ K where silicon burn to produce iron, the most stable atoms, and there will be a iron core with its mass of $1.3 - 2M_\odot$ surrounded by layers of nickel and silicon.

The core stops burning in either cases and the gas pressure cannot sustain the core's self-gravity. The core contracts and the temperature goes up until the degeneracy pressure of electrons start to support the gravity. The Fermi energy of degenerate electrons gets higher and higher and exceeds the difference between the rest mass energies of neutrons and protons (1.3 MeV) under the density of $> 10^7$ g cm^{-3}. Consequently neutrons have lower energies than the state of separated protons and electrons, thus electron capture reactions

$$\mathrm{p} + \mathrm{e}^- \rightarrow \mathrm{n} + \nu_\mathrm{e} \tag{2.1}$$

occur, which is called neutronization. The produced neutrinos take out most of energies into the space and the inner pressure decreases further. Finally the core collapses.

In addition to the neutronization, photolysis of atoms contributes the core contraction. Regarding iron atoms, photolysis reactions

$$^{56}\mathrm{Fe} + \gamma \rightarrow 13\,^4\mathrm{He} + 4\mathrm{n} - 124.4 \text{ MeV} \tag{2.2}$$

begin under the temperature of $\sim 10^{10}$ K. The produced helium atoms dissolve into protons and neutrons in the higher temperature,

$$^4\mathrm{He} \rightarrow 2\mathrm{p} + 2\mathrm{n} - 28.3 \text{ MeV}. \tag{2.3}$$

As they are endothermic reactions, the pressure of the core lowers.

The core collapses rapidly (within ~ 0.1 s) because of the decreased pressure until the density equals that of a nucleus, 10^{14} g cm^{-3}. Gases of outer layers freely fall onto the contracted core and rebound on the hard surface of the core. The recoiled gas flux produces shock waves to blow off the star assisted by the neutrino radiation pressure, and the collapsed compact core is left. This is a core-collapse supernova explosion. The total kinetic energy of gases is 10^{51} erg and the initial speed of gases is $\sim 10^4$ km s^{-1}. The explosion scatters heavy elements synthesized in the explosion as well as lighter elements from nuclear fusions in the main sequence into the interstellar space. This type of the supernova is spectroscopically observed as the type Ib, Ic or II.

The core left behind the core-collapse supernova becomes a neutron star. A neutron star is very compact such that matter with a solar mass filled within a radius of ~ 10 km. Matter with the size of a lump of sugar inside the neutron star weighs a billion tons and the strength of the gravitational force on the neutron star surface is a hundred billion times larger then that on the earth surface. A neutron star itself is highly dense and like a huge nuclear atom, where matter is in an extreme state. The inner part of a neutron star is neutron-rich unlike normal nuclei due to the neutronization expressed above, which contains 90 % neutrons and 10 % protons.

Neutrons are Fermi particles with a spin of 1/2. It is the degenerate pressure of neutrons that sustains the star against the self-gravitational contraction. Even the degenerate pressure cannot support the star if the star is too heavy. It is difficult to seek the upper limit of the mass, which is called the Chandrasekhar limit for neutron stars. Inside neutron stars, the density is high enough for neutrons to touch other neutrons and the nuclear force interacting between neutrons becomes important. As well as the degenerate pressure, the effects of the nuclear force have to be considered in equations of states. Studies are in progress for nuclear forces under an extra-high density. General-relativistic effects should be included as well for the very strong gravitation. The prediction of the limit mass depends on nuclear force models, varying between 1.5 to $3M_\odot$. If a core left behind the supernova explosion is heavier than the mass limit, it cannot exist as a neutron star and collapses further to a black hole. The initial mass of the main sequence star which leaves a black hole is thought to be $> 30M_\odot$.

2.2 Variety of pulsars

After the discovery of a pulsed radio source [1], Gold (1968) [18] and Pacini (1968) [19] proposed it is a rotating magnetic neutron star. It is natural to suppose that the stable repetition of pulses are due to the rotation of the star. However the rotation suggested by the pulse period is fast enough to disrupt normal stars. Only neutron stars can escape the centrifugal disruption thanks to their strong gravity.

Over 1800 rotation-powered pulsars are listed in the ATNF pulsar catalog [20]. Figure 2.1 shows the distribution of the rotational period P and its time derivative $\dot{P}$ for all cataloged pulsars. There is a main group around $P \sim 1$ s and $\dot{P} \sim 10^{-15}$ s s^{-1}, which are called normal or ordinary pulsars. Normal pulsars are considered to be in the stage of slowing down and converting their rotational energy into radiation.

A significant number of sources span the smaller P and $\dot{P}$ region. They are called millisecond pulsars after their period of ~ 1 ms. When the rotational energy of normal pulsars runs out, they are thought to become "dead pulsars". Millisecond pulsars are considered to be reborn from these dead pulsars due to spinning-up by the mass accretion from their binary companion stars. Therefore millisecond pulsars are also called "recycled pulsars".

In addition to these two main populations, there are a few pulsars showing an anomalous feature of the spin-down with $P = 6 - 12$ s and $\dot{P} \sim 10^{-11} - 10^{-10}$ s s^{-1}. A very strong surface magnetic field ($10^{14} - 10^{15}$ G) is derived with these parameters (see the next section). Those pulsars are called "magnetars" after their strong magnetic field. Some of the magnetars were discovered as X-ray pulsars with a long rotation period (called anomalous X-ray pulsars; AXPs), the others were first found as bright bursts in X-rays and gamma-rays (called soft gamma repeaters; SGRs). Since SGRs also show the X-ray pulsations and some of AXPs also show bursts, they are collectively called magnetars. A possible mechanism of the energy release of magnetars is a magnetic reconnection, which can be observed in the solar flares.

Neutron stars or pulsars are born in supernova explosions as described in §2.1. However pulsations cannot be observed in a handful of point sources near the center of young ($\sim$ 1000 yr) supernova remnants like Cassiopeia A, Puppis A and so on. The point sources are called central compact objects (CCOs). CCOs are characterized by constant, unpulsed X-ray emission with thermal-like spectrum and lack of radio/infrared/optical counterparts, as well as of surrounding diffuse nebulae. Although these features are different from those of normal pulsars and magnetars, CCOs are supposed to be neutron stars because of their locations at the center of the supernova remnants. Studies on CCOs

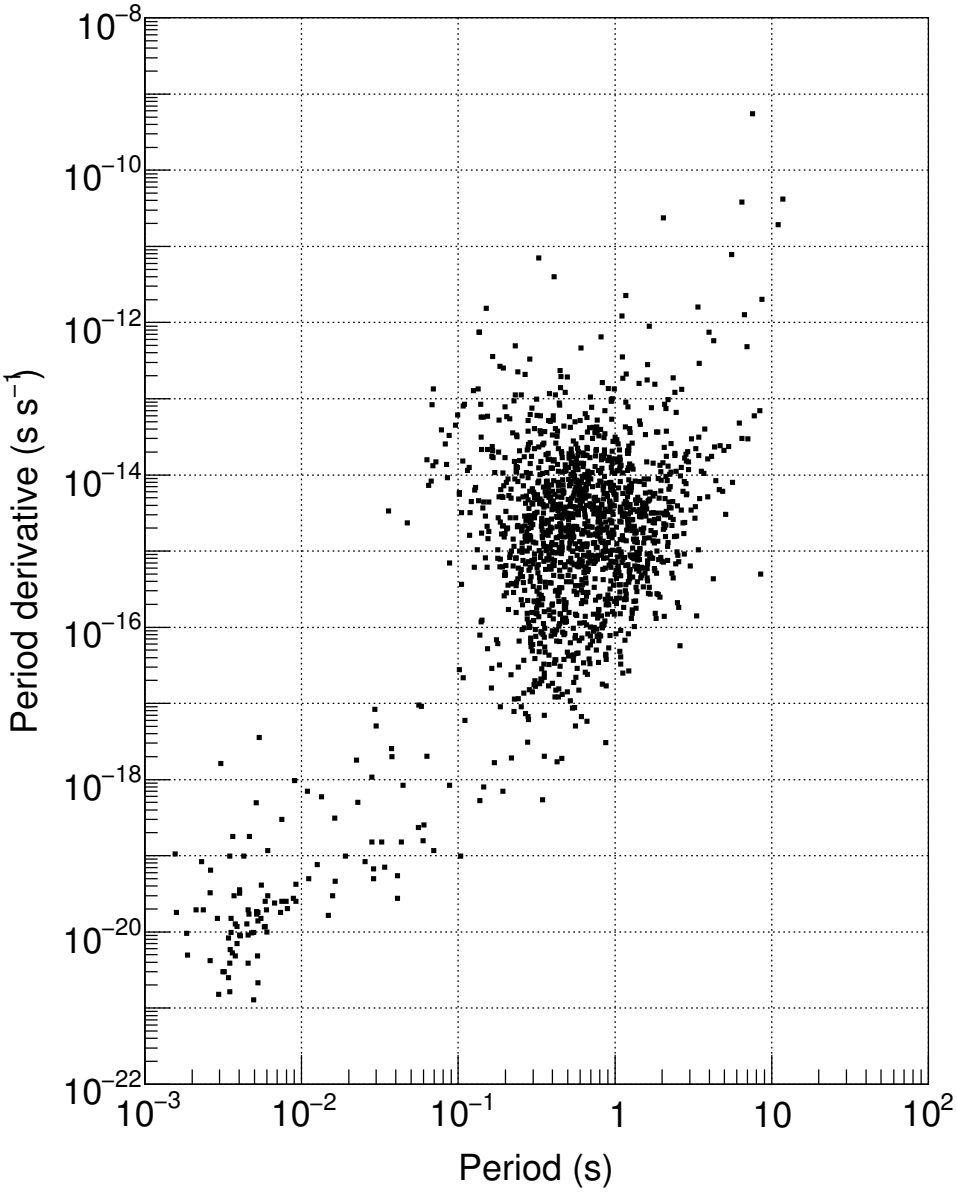

Figure 2.1: Period–period derivative diagram of pulsars listed in the ATNF catalog [20].

are important because understanding the birth properties of neutron stars would be crucial to describe evolutionary paths of different species of pulsars and their connection.

2.3 Characteristic parameters of pulsars

The general pulsar characteristics are commonly described by only the two spin parameters, P and $\dot{P}$. Energy loss by the slowdown of the rotation is supposed to be converted into its emission. A rotating object has a rotation energy of

$$E = \frac{1}{2} I \Omega^2, \tag{2.4}$$

where E is the rotation energy, I is the moment of inertia and Ω is the angular velocity. The time derivative of E is

$$\dot{E} = I\Omega\dot{\Omega}. \tag{2.5}$$

In case of pulsars, $\dot{E}$ is usually negative because pulsars lose their rotational energy. In the point of view of energy release, $-\dot{E}$ is called a "spin-down luminosity", which is denoted by $L_{\rm sd}$ in this thesis. The typical spin-down luminosity for normal pulsars is derived as

$$L_{\rm sd} = \frac{4\pi^2 I\dot{P}}{P^3} \sim 4\times10^{31}\left(\frac{I}{10^{45}\ {\rm g\ cm^2}}\right)\left(\frac{P}{1\ {\rm s}}\right)^{-3}\left(\frac{\dot{P}}{10^{-15}\ {\rm s\ s^{-1}}}\right)\ {\rm erg\ s^{-1}}. \tag{2.6}$$

Neutron stars generally have a quite strong magnetic field on their surfaces. When a simple dipole field is assumed, the absolute value of the magnetic dipole moment $\vec{m}$ is related to the surface magnetic field strength $B_{\rm s}$ as

$$|\vec{m}| = \frac{1}{2}B_{\rm s}R_{\rm s}^3, \tag{2.7}$$

where $R_{\rm s}$ is the radius of the neutron star. If a magnetic dipole rotates in vacuum around the rotation axis $\vec{\Omega}$ with the inclination angle α, its radiation power is

$$P_{\rm rad} = \frac{2\ddot{\vec{m}}^2}{3c^3} = \frac{2\vec{m}^2\Omega^4\sin^2\alpha}{3c^3} = \frac{8B_{\rm s}^2R_{\rm s}^6\Omega^4\sin^2\alpha}{3c^3}, \tag{2.8}$$

where c is the speed of light. Assuming the pulsar loses all energy by the dipole radiation, the surface magnetic field is obtained by

$$B_{\rm s} = \left(\frac{3c^3IP\dot{P}}{8\pi^2R_{\rm s}^6\sin^2\alpha}\right)^{1/2} \tag{2.9}$$

and its typical value is

$$B_{\rm s} \sim 1\times10^{12}\left(\frac{P}{1\ {\rm s}}\right)^{1/2}\left(\frac{\dot{P}}{10^{-15}\ {\rm s\ s^{-1}}}\right)^{1/2}\ {\rm G} \tag{2.10}$$

when $\alpha = 90^\circ$ is assumed. This strong magnetic field could be explained as coming from a progenitor main sequence star of the neutron star. If the progenitor's magnetic field keep confined in the star after the supernova explosion, there is a conserved quantity of BR^2. If we think about the sun ($B_\odot \sim 100$ G and $R_\odot = 7\times10^5$ km), the magnetic field of a neutron star is expected to be

$$B_{\rm NS} = B_\odot\frac{R_\odot^2}{R_{\rm NS}^2} \sim 5\times10^{11}\ {\rm G}. \tag{2.11}$$

Charged particles around a pulsar is frozen in the strong magnetic field and can co-rotate within the radius where the speed of particles reaches the speed of light. This boundary is called a "light cylinder" and its radius is

$$R_{\rm lc} = \frac{c}{\Omega}. \tag{2.12}$$

Since the dipole field strength decreases inversely proportional to the third power of the distance, the magnetic field at the light cylinder and its typical value are

$$B_{\rm lc} = B_{\rm s}\left(\frac{R_{\rm s}}{R_{\rm lc}}\right)^3 \sim 9\left(\frac{P}{1\ {\rm s}}\right)^{-5/2}\left(\frac{\dot{P}}{10^{-15}\ {\rm s\ s^{-1}}}\right)^{1/2}\ {\rm G}. \tag{2.13}$$

If we assume the time derivative of angular velocity $\dot{\Omega}$ evolves according to a simple power-law

$$\dot{\Omega} = -k\Omega^n, \tag{2.14}$$

where k is a constant and n is called a "breaking index". The breaking index is expected to be $n = 3$ in case of the magnetic dipole radiation in the vacuum, and $2 < n < 3$ in the plasma. By integrating the equation above, we obtain an indicator of the age of a pulsar as

$$t = -\frac{\Omega}{(n-1)\dot{\Omega}}\left[1 - \left(\frac{\Omega}{\Omega_0}\right)^{n-1}\right], \tag{2.15}$$

where Ω_0 is the initial angular velocity at $t = 0$. If $\Omega \ll \Omega_0$ and $n = 3$ are assumed, we obtain a "characteristic age"

$$\tau_{\rm c} = -\frac{\Omega}{2\dot{\Omega}} = \frac{P}{2\dot{P}} \sim 2\times 10^7\left(\frac{P}{1\ {\rm sec}}\right)\left(\frac{\dot{P}}{10^{-15}\ {\rm s\ s^{-1}}}\right)\ {\rm yr}. \tag{2.16}$$

The actual breaking index can be observed with

$$n = \frac{\Omega\ddot{\Omega}}{\dot{\Omega}^2}, \tag{2.17}$$

if one can measure $\ddot{\Omega}$. There are a few pulsars which have been measured the breaking index; Crab pulsar ($n = 2.509 \pm 0.001$) [21], PSR B1509−58 ($n = 2.8 \pm 0.2$) [22], PSR B0540−69 ($n = 2.01 \pm 0.02$) [23] and Vela pulsar ($n = 1.4 \pm 0.2$) [24].

2.4 Pulsar magnetosphere

Some pulsars do emit optical, X-ray and gamma-ray pulsed radiation. Soon after the famous Crab pulsar was discovered in radio observations, its pulsation is also observed in the optical and X-ray ranges [25]. The origin of these non-thermal emission is thought to be the particles accelerated in the pulsar magnetosphere.

Let us assume a no-rotating neutron star in vacuum with a dipole magnetic field. The dipole field is expressed in the polar coordinate setting z-axis toward the dipole axis as

$$B_r = B_{\rm s}\left(\frac{R_{\rm s}}{r}\right)^3\cos\theta \tag{2.18}$$

$$B_\theta = \frac{B_\mathrm{s}}{2}\left(\frac{R_\mathrm{s}}{r}\right)^3 \sin\theta, \tag{2.19}$$

where θ is the polar angle to the dipole axis, B_r and B_θ are the radial and azimuthal components of the surface magnetic field B_s, respectively. Then consider a neutron star rotating with an angular velocity Ω, setting the spin axis aligned to the z-axis. This system is a unipolar inductor in which maximum potential difference is induced between the equator and the pole. Since neutron stars are supposed to be perfect conductors, Ohm's law holds as

$$\vec{E} + \frac{\vec{\Omega}\times\vec{r}}{c}\times\vec{B} = 0. \tag{2.20}$$

The induced electric field has the quadrapole field form, and the electric potential is described as

$$\Phi = -\frac{Q}{r^3}\left(3\cos^2\theta - 1\right), \tag{2.21}$$

where $Q = \mu R_\mathrm{s}^2\Omega/3c = B_\mathrm{s}\Omega R_\mathrm{s}^5/6c$ is the quadrapole moment.

The electric field parallel to the magnetic field at the surface is so large that charged particles are extracted from the stellar surface to fill the atmosphere and the charged particles screen the electric field component parallel to the magnetic field. The charge density is

$$\rho = -\frac{\vec{\Omega}\cdot\vec{B}_\mathrm{s}}{2\pi c}\frac{1}{1-\left(\frac{\Omega r}{c}\sin\theta\right)^2}. \tag{2.22}$$

Number density

$$n_\mathrm{GJ} = \frac{\rho}{e} \sim 7\times10^{10}\left(\frac{B_\mathrm{z}}{10^{12}\ \mathrm{G}}\right)\left(\frac{P}{1\ \mathrm{s}}\right)^{-1}\ \text{particles cm}^{-3}, \tag{2.23}$$

where B_z is the z-axis component of the magnetic field and $\Omega r\sin\theta \ll c$ is assumed, is called Goldreich-Julian density [3]. Apparently the magnetosphere consists of the positive charge region and a negative charge region. A neutral surface between their boundary ($\vec{\Omega}\cdot\vec{B}_\mathrm{s} = 0$) is called a "null surface".

The magnetic field lines closed within the light cylinder can co-rotate while the others cannot; the latter are called the "open field lines". Particles can escape by only moving along the open field lines and form a "pulsar wind". Focusing the root of open field lines on the neutron star surface, they occupy a region near the magnetic pole called the "polar cap". Since $\sin^2\theta/r$ conserves for the dipole field lines, the radius of the polar cap is

$$R_\mathrm{pc} = R_\mathrm{s}\sin\theta_\mathrm{pc} = R_\mathrm{s}\left(\frac{\Omega R_\mathrm{s}}{c}\right)^{1/2}. \tag{2.24}$$

The particle acceleration is caused by the potential drop between the spin axis and the edge of the polar cap. The maximum potential drop is

$$\Delta\Phi \quad = \quad \Phi|_{(\mathrm{polarcapedge})} - \Phi|_{(\mathrm{rotationaxis})} \tag{2.25}$$

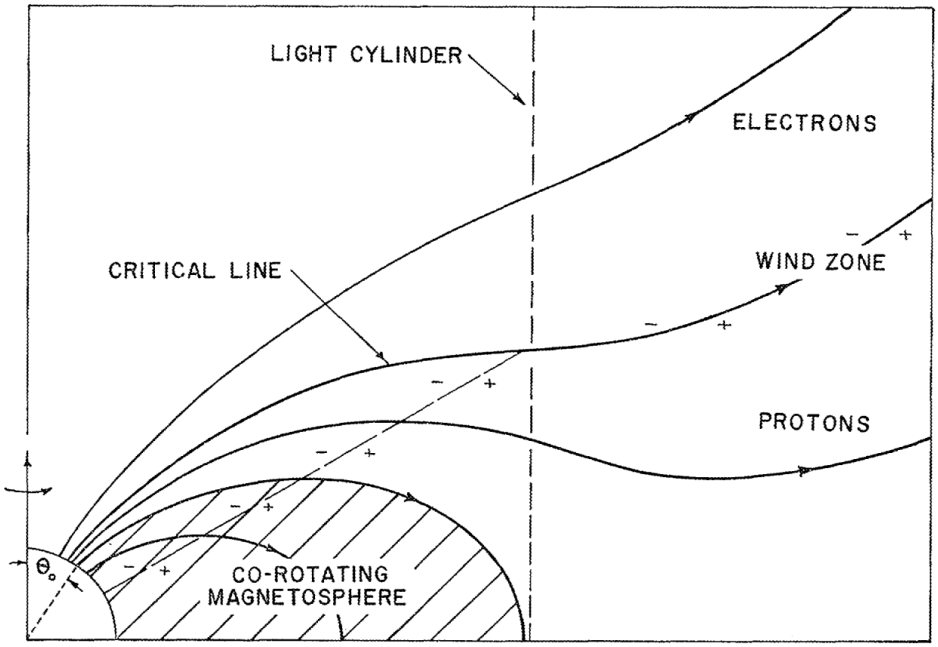

Figure 2.2: A schematic diagram showing the co-rotating magnetosphere and the wind zone beyond the light cylinder. Neutron star is at lower left [3].

$$= -\frac{Q}{R_{\rm s}^3}\left(3\cos^2\theta_{\rm pc} - 3\right) \tag{2.26}$$

$$= \frac{3Q}{R_{\rm s}^3}\sin^2\theta_{\rm pc} \tag{2.27}$$

$$= \frac{B_{\rm s}\Omega^2 R_{\rm s}^3}{2c^2} \tag{2.28}$$

$$\sim 7\times10^{12}\left(\frac{B}{10^{12}\ {\rm G}}\right)\left(\frac{P}{1\ {\rm s}}\right)^{-2}\ {\rm V} \tag{2.29}$$

$$\sim 1\times10^{13}\left(\frac{\left|\dot{E}\right|}{10^{32}\ {\rm erg\ s^{-1}}}\right)^{1/2}\ {\rm V}. \tag{2.30}$$

A schematic diagram of the pulsar magnetosphere is shown in Figure 2.2.

2.5 Observations of gamma-ray pulsars

The first indications for gamma-ray emission were obtained for the Crab pulsar by balloon-borne detectors [26], and confirmed by the second Small Astronomy Satellite (SAS-2) [27], which also discovered the Vela pulsar [28]. The *COS-B* satellite provided details about these two gamma-ray pulsars. The *COS-B* confirmed that the Vela pulsar gamma-ray pulse is not in phase with the radio pulse and does not have the same pulse pattern as that in the radio [29].

The number of gamma-ray pulsars were increased with the *Compton Gamma Ray Observatory* (*CGRO*). Six pulsars were clearly seen and three pulsars were detected with low confidence levels by the Energetic Gamma Ray Experiment Telescope (EGRET). Another pulsar was detected in the lower energy range by the Imaging Compton Telescope (COMPTEL) onboard the *CGRO*. Hereafter we briefly describe characteristics of gamma-ray pulsars based on a summary by Thompson (2004) [30].

Important features seen in the light curves (Figure 2.3) are:

- They do not have the same shapes at all wavelengths. Some combination of the geometry and the emission mechanism is energy-dependent. In soft X-rays, for example, the emission in same cases appears to be thermal, probably from the surface of the neutron star; thermal emission does not contribute to radio or gamma radiation.

- Not all the seven pulsars are seen at the highest energies. PSR B1509−58 (which has the strongest magnetic field among the gamma-ray pulsars) is seen up to 10 MeV by COMPTEL, but not above 100 MeV by EGRET.

- The six seen by EGRET all have a common feature - they show a double peak in their light curves. Because these high-energy gamma-rays are associated with energetic particles, it seems likely that the particle acceleration and interactions are taking place along a large hollow cone or other surface. Models in which emission comes from both magnetic poles of the neutron star appear improbable in light of the prevalence of double pulses.

Broadband spectra for the seven gamma-ray pulsars are shown in Figure 2.4. The presentation in νF_ν format indicates the observed power per frequency interval across the spectrum. In all cases, the maximum power output is in the gamma-ray band. Other noteworthy features on this figure are:

- The distinction between the radio emission (which originates from a coherent process) and the high-energy emission (probably from individual charged particles in an incoherent process) is visible for some of these pulsars, particularly Crab and Vela.

- Vela, Geminga and PSR B1055−52 show an evidence of a thermal component in X-rays, thought to be from the hot neutron star surface.

- The gamma-ray spectra of known pulsars are typically flat, with most having photon power-law indices of about 2 or less. Energy breaks are seen in the $1-4$ GeV band

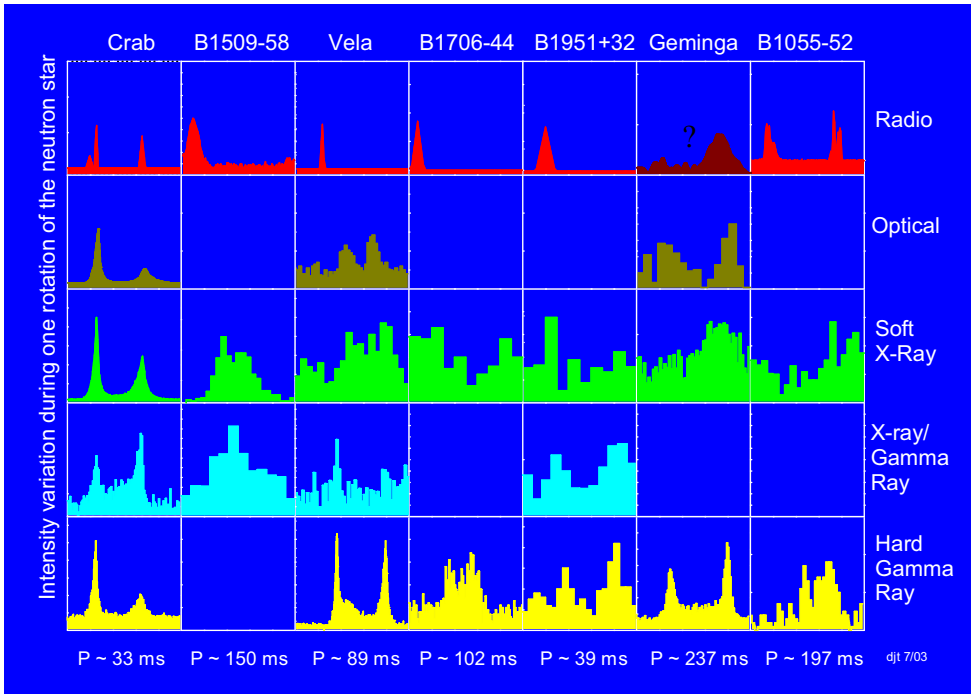

Figure 2.3: Light curves of seven gamma-ray pulsars in five energy bands; radio, optical, soft X-ray (< 1 keV), hard X-ray /soft gamma-ray (~ 10 keV $- 1$ MeV), and hard gamma-ray (> 100 MeV). Each panel shows one full rotation of the neutron star [30].

for several of these pulsars. These changes in the cutoff energy appear to be related to the calculated surface magnetic field of the pulsar.

- No pulsed emission is seen above 30 GeV, near the upper limit of EGRET. The nature of the high-energy cutoff is an important feature of pulsar models.

- Although Figure 2.4 shows a single spectrum for each pulsar, the pulsed energy spectrum varies with pulsar phase. A study of the EGRET data by Fierro et al. (1998) of the phase-resolved emission of Vela, Geminga and Crab showed no simple pattern of variation of the spectrum with phase [31].

Several sources seen in gamma-rays have characteristics that strongly resemble those of the known gamma-ray pulsars, but without evidence of gamma-ray pulsation. 3EG J1835+5918 is thought to be a Geminga-like pulsar from its gamma-ray and X-ray spectral features and no detection of optical nor radio counterparts. Two unknown sources (3EG J2020+4127 and 3EG J0010+7309) positionally associated with supernova remnants and their X-ray counterparts show spectra like pulsars. In addition, a number of young radio pulsars have been found in EGRET error boxes but non gamma-ray pulsation was detected.

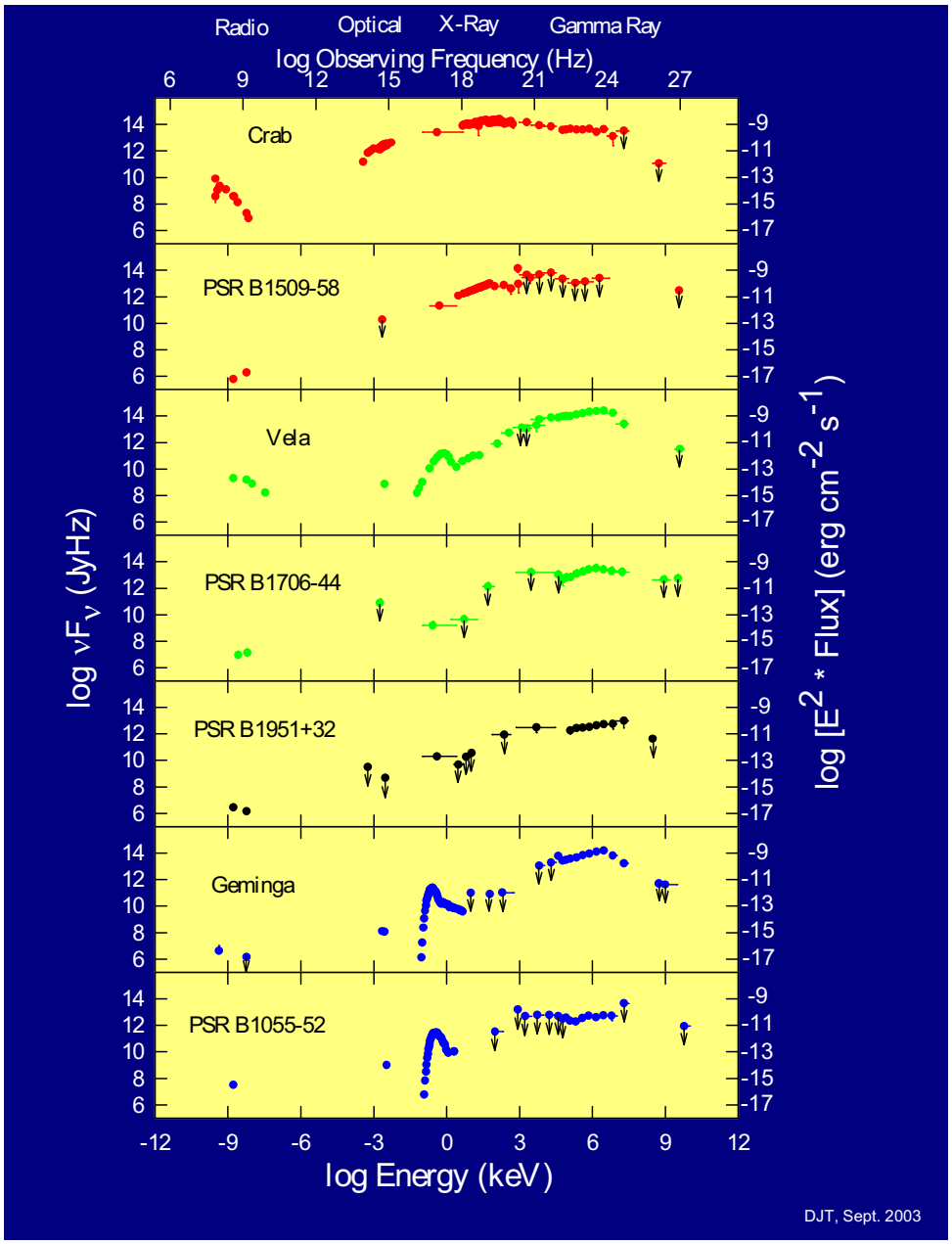

Figure 2.4: Multiwavelength spectra of seven gamma-ray pulsars [30].

Gamma-ray pulsars tend to be in a group with younger characteristic ages, higher magnetic fields and higher open field line voltages. Furthermore, gamma-ray luminosity is proportional to the open field line voltage, thus the square root of the spin-down luminosity. These facts suggest that particles are being accelerated electromagnetically.

2.6 Magnetospheric emission models

Discovery of high energy emission from the Crab pulsar has given evidences for non-thermal radiation of magnetospheric origin. The emission in the radio band is not more than 10^{-5} of the spin down luminosity. Most of rotation energy is converted into the particle acceleration which originate high energy pulsation ranging from X-rays to GeV gamma-rays. High energy emission implies the existence of efficient acceleration mechanism.

Several models have been proposed for the particle acceleration and the photon emission mechanism. As described below, they are roughly classified into the "polar cap" model, the "outer gap" model and the "slot gap" model. Their clear difference appears in regions where the emission occurs. Figure 2.5 illustrates the emission regions. The radiation takes place closer to the neutron star in the polar cap model, and farther out in the magnetosphere in the outer gap or the slot gap model. They are called vacuum gaps or vacuum regions. Vacuum gaps are filled with plasma but its density is lower than the Goldreich-Julian density, where the magnetically induced electric field is saturated and therefore electrons can be accelerated to very high energies.

The polar cap model [33, 34, 35] sets the particle acceleration region just above the polar cap, where primary particles are accelerated and create pairs. The primary particles are accelerated by the potential drop, which is comparable to that between the pole and the edge of the polar cap, and cause cascades of electron-positron pairs. These secondary particles emit the high energy radiation through the curvature radiation, the synchrotron radiation or the Compton up-scattering of of soft photons from the stellar surface. The emission is in a hollow cone defined by the tangent to the last open field line, which has a difficulty for reproducing observed wide pulse profiles.

The outer gap model [17, 36] assumes a gap with a strong electric field parallel to the magnetic field line is developed in the outer magnetosphere along the last closed field line between the null surface and the light cylinder. Primary particles radiate curvature or inverse Compton emission. Radiated gamma-ray photons go through a dense photon field and create secondary electron-positron pairs when another photon hits. These secondary particles attribute the high-energy emission via curvature or synchrotron radiation. The

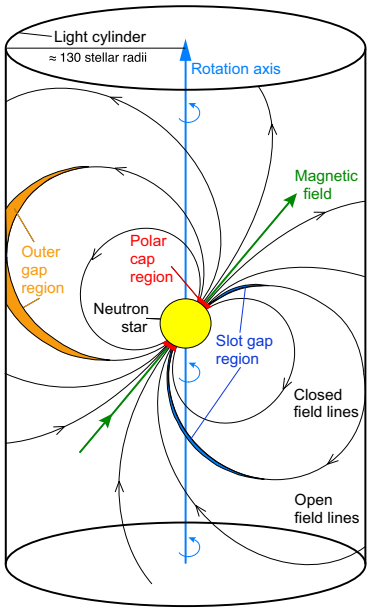

Figure 2.5: Emission regions proposed by the polar cap, outer gap and slot gap models. The radius of the light cylinder is for the Crab pulsar [32].

spectrum of the accelerated primary particles reproduces the softer (photon index $\sim 1.5 - 2$) observed spectrum when convolved with the hard curvature spectrum (photon index 2/3). This model predicts fan gamma-ray beams, which well reproduce the observed light curves with widely separated double peaks and the "bridge" structure between the peaks seen in the light curves of the Vela and the Geminga (Figure 2.3).

The slot gap model [37, 38, 39] proposes the gap as a narrow pair-free space between the last open field lines and the boundary of the pair plasma column that is expected to develop above the polar cap. A narrow beam of high-energy emission originates from the low-altitude cascade on field lines interior to the slot gap. A broader hollow cone beam originates from the high-altitude cascade above the interior edge of the slot gap. In this model, the high-energy cutoff arises due to the magnetic pair creation.

These models have been just proposals or assumptions. However, recently Hirotani (2008) [40] showed three dimensional solutions of Maxwell and Boltzmann equations and the high-energy emissions in the pulsar magnetosphere for the first time. In his results, the outer gap and the polar cap regions were produced without any additional assumptions but the slot gap needed assumptions for the distribution of plasmas.

2.7 Recent observations by the *Fermi* LAT

The high sensitivity of *Fermi* LAT now brings us a large number of gamma-ray pulsars. Before publishing the pulsar catalog paper [12], brand-new discoveries of pulsars with only the gamma-ray data [41, 42] and pulsed gamma-ray detection of known millisecond pulsars [43] are reported. The number of the LAT pulsars has increased from 46 at the time of the pulsar catalog paper to 55 as of December 2009, as listed in Table 2.1. These additional discoveries will be reported soon [13, 14]. The detected pulsars include 21 radio-selected, 25 gamma-selected and 9 millisecond pulsars.

Two distinct pulsation searches of the LAT data have been conducted. One search uses the ephemerides of known pulsars obtained from radio and X-ray observations. The other method, called "blind period searches" searches for periodicity in the arrival times of gamma-rays coming from the direction of neutron star candidates and unknown bright sources.

The search method with known ephemerides is useful to find pulsars with low gamma-ray flux. Since the best candidates for gamma-ray emission are the pulsars with high spin-down luminosity, contemporaneous pulsar ephemerides should be measured regularly. The *Fermi* Pulsar Timing Consortium has obtained 762 pulsar ephemerides, which include 218 pulsars with higher spin-down luminosity and 544 normal, and also millisecond pulsars over the entire $P - \dot{P}$ plane (Figure 2.1) so as to avoid biased detections. These results are found in Smith et al. (2008) [44] and Weltevrede et al. (2009) [45].

The blind period searches are used for new pulsar discoveries. Pulsation searches with gamma-ray photons are difficult because the photon arrivals are very sparse. Additionally, a very broad parameter space of the frequency and the frequency derivative requires huge computation resources. Atwood et al. (2006) resolved these problems with a computationally efficient time-difference technique and made the blind searches possible [46]. However, there is a loss in sensitivity and higher photon flux is necessary for a statistically significant detection than with the method using known ephemerides. Several hundred LAT sources have been examined with the blind pulse search. The parameter space is $0.5 \sim 64$ Hz in frequency and $-3.7 \times 10^{-10} \sim 0$ Hz s^{-1} in frequency derivative, which covers ~ 86 % of pulsars listed in the ATNF database. After the pulse detection, TEMPO2 [47] was used to derive more precise ephemerides and the location of the source. Of the 16 pulsars reported in the first blind search paper [42], 13 pulsars are associated with the "unidentified" EGRET sources. As predicted by Yadigaroglu and Romani (1995) [48], most of the unknown point sources in the Galactic plane may be gamma-ray pulsars without radio emission like the Geminga.

Obtained light curves are consistent with both a single broad peak or with double narrow peaks. Spectra are described with a flat power-law with a natural exponential cutoff at a few GeV. These results of light curves and spectra agree with the high-altitude emission (i.e. outer gap or slot gap). Furthermore the shapes of the light curves apparently depend on the energy range for some bright pulsars. These information should be important helps for understanding high-energy emission geometry precisely.

Abdo et al. (2009) [49] reported the early observations of the Vela pulsar, which is the brightest gamma-ray pulsar. The shape of the spectral cutoff significantly ruled out the emission near the neutron star surface (eg. the polar cap model). The observations support the outer gap or the slot gap models.

Table 2.1: List of pulsars whose gamma-ray pulsations were detected by *Fermi* LAT.

JName[a]	R.A. (°)	Dec. (°)	ν (Hz)[b]	$\dot{\nu}$ (Hz s^{-1})[c]	$L_{\rm sd}$ (erg s^{-1})[d]	$\tau_{\rm c}$ (yr)[e]	Type[f]
J0007+7303	1.7548	73.0513	3.17	-3.61×10^{12}	4.51×10^{35}	1.39×10^{4}	g
J0030+0451	7.6143	4.8610	205.53	-4.30×10^{16}	3.49×10^{33}	7.58×10^{9}	m
J0034−0534	8.5910	−5.5768	532.71	-1.45×10^{15}	3.04×10^{34}	5.84×10^{9}	mb
J0205+6449	31.4080	64.8286	15.21	-4.48×10^{11}	2.69×10^{37}	5.38×10^{3}	r
J0218+4232	34.5265	42.5382	430.46	-1.43×10^{14}	2.44×10^{35}	4.76×10^{8}	mb
J0248+6021	42.0797	60.3584	4.61	-2.67×10^{13}	4.85×10^{34}	2.74×10^{5}	r
J0357+32	59.4692	32.0868	2.25	-6.54×10^{14}	5.81×10^{33}	5.46×10^{5}	g
J0437−4715	69.3159	−47.2524	173.69	-1.74×10^{15}	1.19×10^{34}	1.58×10^{9}	mb
J0534+2200	83.6331	22.0145	29.74	-3.72×10^{10}	4.37×10^{38}	1.27×10^{3}	r
J0613−0200	93.4332	−2.0131	326.60	-1.02×10^{15}	1.32×10^{34}	5.06×10^{9}	mb
J0631+1036	97.8648	10.6173	3.47	-1.26×10^{12}	1.73×10^{35}	4.36×10^{4}	r
J0633+0632	98.4348	6.5413	3.36	-9.00×10^{13}	1.20×10^{35}	5.92×10^{4}	g
J0633+1746	98.4756	17.7703	4.22	-1.95×10^{13}	3.25×10^{34}	3.42×10^{5}	g
J0659+1414	104.9506	14.2393	2.60	-3.71×10^{13}	3.81×10^{34}	1.11×10^{5}	r
J0742−2822	115.7044	−28.3788	6.00	-6.04×10^{13}	1.43×10^{35}	1.57×10^{5}	r
J0751+1807	117.7882	18.1274	287.46	-6.44×10^{16}	7.31×10^{33}	7.07×10^{9}	mb
J0835−4510	128.8361	−45.1764	11.19	-1.56×10^{11}	6.88×10^{36}	1.14×10^{4}	r
J1022−5746	155.7597	−57.7693	8.97	-3.09×10^{11}	1.09×10^{37}	4.60×10^{3}	g
J1028−5819	157.1167	−58.3181	10.99	-1.94×10^{12}	8.42×10^{35}	8.97×10^{4}	r
J1044−5737	161.1367	−57.6219	7.19	-2.83×10^{12}	8.03×10^{35}	4.03×10^{4}	g
J1048−5832	162.0508	−58.5349	8.08	-6.29×10^{12}	2.01×10^{36}	2.04×10^{4}	r
J1057−5226	164.4952	−52.4490	5.07	-1.50×10^{13}	3.01×10^{34}	5.35×10^{5}	r
J1124−5916	171.1629	−59.2722	7.38	-4.09×10^{11}	1.19×10^{37}	2.86×10^{3}	r
J1413−6205	213.3739	−62.0947	9.11	-2.30×10^{12}	8.27×10^{35}	6.28×10^{4}	g
J1418−6058	214.6823	−60.9610	9.04	-1.39×10^{11}	4.95×10^{36}	1.03×10^{4}	g
J1420−6048	215.0343	−60.8046	14.66	-1.79×10^{11}	1.03×10^{37}	1.30×10^{4}	r
J1429−5911	217.4943	−59.1929	8.63	-2.27×10^{12}	7.75×10^{35}	6.02×10^{4}	g
J1459−60	224.8747	−60.8877	9.69	-2.38×10^{12}	9.09×10^{35}	6.46×10^{4}	g
J1509−5850	227.3630	−58.8489	11.25	-1.16×10^{12}	5.15×10^{35}	1.54×10^{5}	r
J1614−2230	243.5000	−22.5000	317.38	-9.69×10^{16}	1.21×10^{34}	5.19×10^{9}	mb
J1709−4429	257.4280	−44.4856	9.76	-8.84×10^{12}	3.40×10^{36}	1.75×10^{4}	r
J1718−3825	259.5565	−38.4217	13.39	-2.36×10^{12}	1.25×10^{36}	8.97×10^{4}	r

Table 2.1: Continued.

JName[a]	R.A. (°)	Dec. (°)	ν (Hz)[b]	$\dot{\nu}$ (Hz s^{-1})[c]	$L_{\rm sd}$ (erg s^{-1})[d]	$\tau_{\rm c}$ (yr)[e]	Type[f]
J1732−31	263.1396	−31.5225	5.09	-7.26×10^{13}	1.46×10^{35}	1.11×10^{5}	g
J1741−2054	265.4908	−20.9033	2.42	-9.82×10^{14}	9.37×10^{33}	3.90×10^{5}	g
J1744−1134	266.1225	−11.5818	245.43	-5.34×10^{16}	5.18×10^{33}	7.28×10^{9}	m
J1747−2958	266.8171	−29.9686	10.12	-6.28×10^{12}	2.51×10^{36}	2.55×10^{4}	r
J1809−2332	272.4592	−23.5397	6.81	-1.60×10^{12}	4.30×10^{35}	6.76×10^{4}	g
J1813−1246	273.3490	−12.7673	20.80	-7.60×10^{12}	6.24×10^{36}	4.34×10^{4}	g
J1826−1256	276.5354	−12.9434	9.07	-1.00×10^{11}	3.58×10^{36}	1.44×10^{4}	g
J1833−1034	278.3899	−10.5688	16.16	-5.27×10^{11}	3.36×10^{37}	4.85×10^{3}	r
J1836+5925	279.0566	59.4247	5.77	-5.05×10^{14}	1.15×10^{34}	1.81×10^{6}	g
J1846+0919	281.6176	9.3299	4.43	-1.91×10^{13}	3.34×10^{34}	3.68×10^{5}	g
J1907+06	286.9786	6.0375	9.38	-7.64×10^{12}	2.83×10^{36}	1.95×10^{4}	g
J1952+3252	298.2425	32.8779	25.29	-3.73×10^{12}	3.72×10^{36}	1.08×10^{5}	r
J1954+2836	298.5799	28.6017	10.79	-2.46×10^{12}	1.05×10^{36}	6.94×10^{4}	g
J1957+5036	299.3843	50.6091	2.67	-1.47×10^{14}	1.55×10^{33}	2.88×10^{6}	g
J1958+2846	299.6679	28.7649	3.44	-2.51×10^{12}	3.42×10^{35}	2.17×10^{4}	g
J2021+3651	305.2688	36.8575	9.64	-8.90×10^{12}	3.39×10^{36}	1.71×10^{4}	r
J2021+4026	305.3753	40.4466	3.77	-7.81×10^{13}	1.16×10^{35}	7.65×10^{4}	g
J2032+4127	308.0550	41.4563	6.98	-9.72×10^{13}	2.68×10^{35}	1.14×10^{5}	g
J2043+2740	310.9313	27.6822	10.40	-1.20×10^{13}	4.94×10^{34}	1.37×10^{6}	r
J2055+2539	313.9534	25.6663	3.13	-4.04×10^{14}	5.00×10^{33}	1.23×10^{6}	g
J2124−3358	321.1827	−33.9791	202.79	-8.46×10^{16}	6.78×10^{33}	3.80×10^{9}	m
J2229+6114	337.2707	61.2369	19.36	-2.92×10^{11}	2.23×10^{37}	1.05×10^{4}	r
J2238+59	339.6163	59.0617	6.15	-3.67×10^{12}	8.89×10^{35}	2.66×10^{4}	g

[a] The JNames of new gamma-ray pulsars discovered by the *Fermi* LAT can be changed in the future.

[b] Pulse frequency.

[c] Time derivative of the pulse frequency.

[d] Spin-Down luminosity or rotational energy loss rate.

[e] Characteristic age.

[f] g: pulsars first discovered in gamma-ray timing analysis (however there is an exception: only PSR J0633+1746 was discovered in a X-ray observation by *ROSAT* [6]), r: pulsars discovered in radio timing analysis, m: millisecond pulsars, mb: millisecond pulsars with binary companion stars. All millisecond pulsars were discovered in radio.

Chapter 3

Instrumentation

We utilized the *Fermi Gamma-ray Space Telescope* for gamma-ray observations and three contemporary X-ray observatories, *Suzaku*, *XMM-Newton* and *Chandra X-ray Observatory*. In this chapter, we briefly introduce those missions and the basic properties of on-board science instruments. See references for more details.

3.1 *Fermi Gamma-ray Space Telescope*

The *Fermi Gamma-ray Space Telescope* is an international space mission for observational studies of gamma-ray cosmos. The spacecraft was placed into its orbit by a Delta II Heavy launch vehicle on June 11, 2008. *Fermi* is on a low-earth circular orbit with the altitude of 565 km and the inclination angle of 25.6°. The orbiting period is 95 minutes. *Fermi* features the Large Area Telescope (LAT) [50] as its main instrument. The LAT is an imaging spectroscopy telescope with the largest effective area ever launched into the space in the energy range from 20 MeV to 300 GeV. The LAT is targeting a broad range of sources such as pulsars, active galactic nuclei (AGNs), supernova remnants, Galactic binaries, solar flares and unknown objects formerly found, and also challenging signals from dark matter and new physics. The telescope is continuing all-sky scans every day from August 2008 after on-orbit calibrations [51]. With the high sensitivity of LAT, many new high-energy gamma-ray discoveries have been reported in the earliest days of the mission (see [52, 53, 54] for example). *Fermi* also has scintillator blocks named the Gamma-ray Burst Monitor (GBM) [55] for quick detections of explosive phenomena in the sky in a hard X-ray band (8 keV – 40 MeV) such as gamma-ray bursts (GRBs) or high-energy transients in our Galaxy.

Table 3.1: Properties of *Fermi* LAT and *CGRO* EGRET. Since the performance strongly depends on the energy, only typical values are shown.

Parameter	*Fermi* LAT	*CGRO* EGRET
Energy Range	20 MeV – 300 GeV	20 MeV– 30 GeV
Effective Area	~ 8000 cm^2 (> 1 GeV, on axis)	1500 cm^2
Field of View	2.4 sr (1 GeV)	0.5 sr
Angular Resolution	4.5° (100 MeV),	5.8° (100 MeV)
(95 % containment)	$< 0.15°$ (> 10 GeV)	
Energy Resolution	10 % (1 GeV)	10 %
Source Location Determination	$< 0.5'$	$15'$
Point Source Sensitivity[a]	$< 6 \times 10^{-9}$ cm^{-2} s^{-1}	$\sim 10^{-7}$ cm^{-2} s^{-1}

[a] Assuming sources at a high Galactic latitude with a spectrum of $\propto E^{-2}$ and a one-year observation.

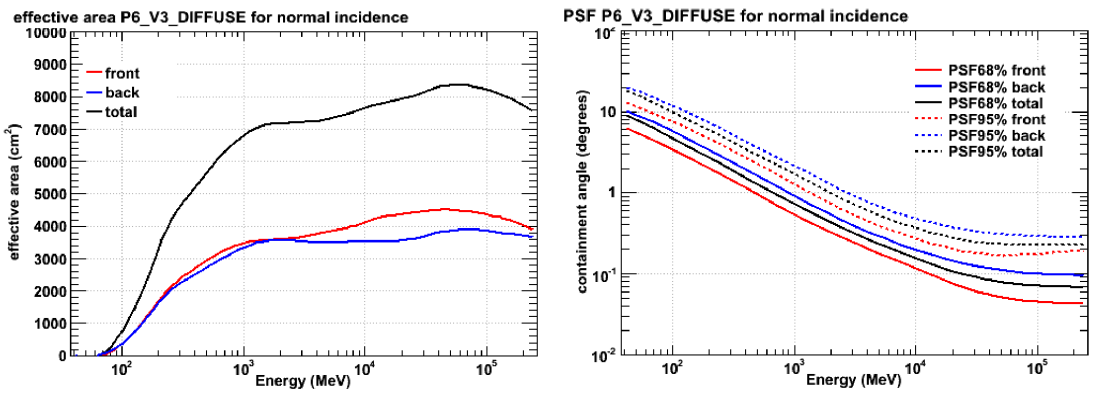

Figure 3.1: Left: Effective area of LAT. Right: Point spread function of LAT. They are calculated with P6_V3_DIFFUSE response matrices for vertically injected photons.

3.1.1 Large Area Telescope

The LAT instrument is a high-energy gamma-ray (20 MeV – 300 GeV) telescope designed to have a high sensitivity with large effective area, wide field of view and good accuracy of source location determination. Table 3.1 summarizes properties of *Fermi* LAT and the EGRET (Energetic Gamma Ray Experiment Telescope) instrument onboard the *Compton Gamma Ray Observatory* (*CGRO*), a high-energy mission operated before *Fermi* from 1991 to 2000 [56]. The sensitivity of *Fermi* LAT is > 10 times higher than that of *CGRO* EGRET. The performance of the LAT strongly depends on the energy. Figure 3.1 shows the effective area and the point spread function as functions of energy.

Figure 3.2 is a schematic view of the LAT. The LAT consists of three components:

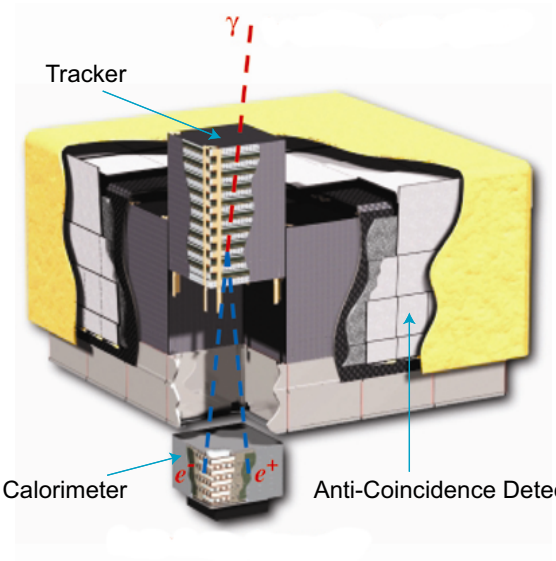

Figure 3.2: A schematic view of the *Fermi* LAT [50].

anti-coincidence detectors [57, 58], tracker [59, 60, 61, 62] and calorimeter [63]. Electron-positron pair creation is the measurement principle of the LAT since it is the primary interaction process between photons and matter in the observing energy range of the LAT. An incoming gamma-ray photon first passes through the anti-coincidence plastic scintillators, then thin tungsten foils in the tracker modules convert a photon into an electron and positron pair. Trajectories of the pair are measured by silicon strip detectors. Finally the electron and positron produce electromagnetic showers in the calorimeter made of cesium iodide (CsI) scintillators.

The anti-coincidence detector enclosing the tracker array is made of plastic scintillator tiles, which are transparent to the high-energy gamma-ray photons because of its small atomic numbers ($Z = 6$ for carbon and $Z = 1$ for hydrogen). Charged particles easily interact with the plastic scintillators. Scintillation lights are read by wavelength-shifter fibers and small photomultiplier tubes. Background charged cosmic-ray particles, whose flux is 10^5 times larger than the photon flux, are reduced using anti-coincidence technique.

The main part of the LAT consists of a four-by-four array of modules called "towers". Each tower comprises a tracker, calorimeter and data acquisition module. A tracker is made of 18 X and Y layers of silicon strip detectors and 18 thin tungsten foils. The silicon strip detectors can measure tracks of converted electrons and positrons with high resolution (< 60 μm) with high detection efficiency (> 99 %) and large signal-to-noise ratio (> 20). The calorimeter in each tower consists of 8 layers of 12 CsI scintillator bars in a hodoscopic arrangement for a total thickness of 10 radiation lengths. In addition, each scintillator is read out by two photodiodes at both ends of each bar to measure where

showers cross in the bar. With this arrangement, the calorimeter units can measure 3-dimensional profiles of electromagnetic showers, which allow for corrections of energy leakage and discrimination between hadronic cosmic-rays.

Events with three hits of tracker layers automatically trigger the readout system. In addition to signals from anti-coincidence detectors, some onboard discriminator algorithms ("gamma-filter") eliminate any particle-like events. While the rate of triggering events is $\sim$ 2.2 kHz, the rate of events filtered and sent to the ground is $\sim$ 400 Hz. Row data sent to the ground are flowed into a pipeline process to be analyzed further and to be formatted. Incident direction of each photon event can be reconstructed with trajectories and energies of converted electron and positron pairs. Each event is tagged how the event is gamma-ray like. For gamma-ray analysis, events are divided into three probability classes called Event Class: Transient, Source and Diffuse[1] . The Diffuse class contains the purest and most reliable gamma-ray events, however the effective area for those events is the least among those classes. The *Fermi* LAT Collaboration strongly encourages people to use the Diffuse class for scientific analysis.

The strategy of the LAT observations is a continuous all-sky scan so as to achieve a high sensitivity and continuous observations of flux variations for sources all around the sky with a large field of view. Therefore the spacecraft is basically in a non-directional mode with the z-axis of the LAT inclined at 50° from the zenith to the north and south poles[2] . The spacecraft switches the pointing direction between the north and the south each orbit so as to scan whole sky with every two orbits ($\sim$ 3 hours). The continuous all-sky scan is important in studies of variable sources such as AGNs and Galactic binaries. However the spacecraft goes into a pointed observation mode, staring only one point of the sky, once a bright bursting object (especially GRBs) appears. The mode change called Autonomous Repoint Request (ARR) is automatically triggered by significant rapid count rate increases of gamma-ray-like events. This automatic maneuver gave us excellent statistics of GeV gamma-ray photons from GRBs for the first time [64, 65, 66, 67].

3.1.2 GLAST Burst Monitor

The GBM consists of twelve sodium iodide (NaI) scintillators, each 12.7 cm in diameter by 1.27 cm thick, and two cylindrical bismuth germanate (BGO) scintillators, each 12.7 cm in diameter and 12.7 cm in height. The NaI detectors cover the lower energy range

[1] The classification will be finer in the next data reprocessing with the latest event reconstruction scheme called "Pass 7.2".

[2] The angle was smaller ($35° - 39°$) from August 2008 to September 2009 then became 50° in order to improve thermal conditions and extend the lifetime of batteries.

from $\sim$ 8 keV to $\sim$ 1 MeV and provide burst triggers and coarse locations. The BGO detectors covers the higher energy range from $\sim$ 150 keV to $\sim$ 40 MeV.

GRBs will be detected by a significant change in count rate in at least two NaI scintillators. Time-tagged event data with 5 μs resolution will be recorded continuously to provide $\sim$ 50 s of pre-trigger information for GRBs. After a trigger, the GBM processor will calculate preliminary position and spectral information for telemetry to the ground and possible automatic pointing of the spacecraft.

3.2 *Suzaku*

Suzaku is the fifth satellite for Japanese X-ray astronomy. It is a joint Japan-US mission developed and operated by the Institute of Space and Astronautical Science of the Japan Aerospace Exploration Agency (ISAS/JAXA) and many other institutions. *Suzaku* was launched into a low-earth circular orbit in July 2005 by a M-V rocket. The orbit is 568 km in the altitude and 31.9° in the inclination. The orbital period is 96 minutes. Although target objects are eclipsed by the earth, observations will never interrupted by flares of solar wind particles in this low-earth orbit.

Suzaku has three kinds of scientific payloads: X-Ray Spectrometer (XRS) [68], X-ray Imaging Spectrometer (XIS) [69] and Hard X-ray Detector (HXD) [70]. XRS is the first micro-calorimeter launched into the space, which has unprecedented spectral resolution ($E/\Delta E \sim 800$), but the liquid helium coolant of XRS evaporated in August 2005 and XRS has been inoperable. However XIS and HXD are working well and retaining excellent X-ray sensitivity with high throughput over a broad-band energy range of 0.2 – 600 keV. Table 3.2 summarizes properties of XIS and HXD.

3.2.1 X-ray Imaging Spectrometer

The XIS instruments consist of four X-ray sensitive silicon charge-coupled device (CCD) cameras operated in a photon-counting mode. Each XIS is located in the focal plane of its own X-Ray Telescope (XRT) [71]. They are co-aligned and operate simultaneously.

A field of view of XIS is $\sim 18' \times 18'$ and an angular resolution of XRT is $\sim 2'$ in the half-power diameter (HPD), which is the diameter within which half of the focused X-rays are enclosed. Figure 3.3 shows the total effective area of the XIS+XRT, which includes features due to the elemental composition of the XIS and XRT. K-shell absorption edges from oxygen (0.54 keV) and aluminum (1.56 keV) in the blocking filters are present, as well as a number of weak M-shell features between 2–3 keV arising from gold used in XRT.

Table 3.2: Properties of XIS and HXD onboard *Suzaku*.

Parameter	XIS	HXD
Energy Range	0.2–12 keV	10–70 keV (PIN)
		40–600 keV (GSO)
Effective Area	340 cm^2 (FI), 390 cm^2 (BI) at 1.5 keV	$\sim$ 160 cm^2 at 20 keV
	150 cm^2 (FI), 100 cm^2 (BI) at 8 keV	$\sim$ 260 cm^2 at 100 keV
Field of View	$17.8' \times 17.8'$	$4.5^\circ \times 4.5^\circ$ ($>$ 100 keV)
		$34' \times 34'$ ($<$ 100 keV)
Angular Resolution	$\sim 2'$ (HPD)	N/A[a]
Energy Resolution	$\sim$ 130 eV at 6 keV	$\sim$ 4.0 keV (PIN, FWHM)
		$7.6/\sqrt{E_{\rm MeV}}$ % (GSO, FWHM)

[a] HXD is a non-imaging instrument.

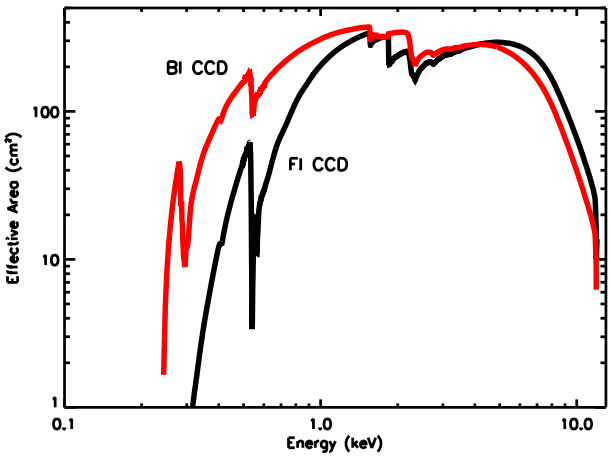

Figure 3.3: XIS effective area of one XRT+XIS system [72].

Each camera has a single CCD chip with an array of 1024 × 1024 picture elements (pixels). Each pixel is 24μm square and the size of the CCD is 25 mm × 25 mm. Three of XIS cameras (XIS0, XIS2 and XIS3) are front-illuminated chips (FI, 0.4–12 keV) but XIS2 is no longer in operation since November 2006 due to a large amount of leaked charge. The other one, XIS1, is a back-illuminated chip (BI, 0.2–12 keV). A CCD has a gate structure on one of the surfaces to transfer the charge packets to the readout gate. The surface of the chip with the gate structure is called a "front side". A FI CCD detects X-ray photons that pass through the gate structures. Because of the photo-electric absorption at the gate structure, the low-energy quantum detection efficiency of a FI CCD is rather limited. Conversely, a BI CCD receives photons from the "back side". There is only a thin layer to enhance the electron collection efficiency on the back side. Thus the detection efficiency in a sub-keV energy band is much higher than that of a FI CCD. On the other hand, since a depletion layer of a BI CCD is thinner than that of a FI CCD, the detection efficiency is lower in the higher energy band.

It is known that the CCD performance gradually degrades due to the radiation damage. This is because charge traps are produced by cosmic-rays and are accumulated in the CCD. One of the unique features of the XIS is the capability to inject small amounts of charge to the pixels so as to fill the charge traps and to make them harmless. This is called the spaced-row charge injection (SCI), and the SCI has been adopted as a standard method since AO-2 [73].

To reduce contamination of X-ray signals by optical and UV light, each XIS has an Optical Blocking Filter (OBF) located in front of it. The XIS had unexpectedly large contamination from some chemical material on the OBF. This reduced the low-energy efficiency of the XIS significantly. The contamination thickness has been monitored by regular observations of calibration targets. This effect is included in the response matrices [74].

3.2.2 Hard X-ray Detector

The HXD is a non-imaging instrument featuring a compound-eye configuration and a low background (Figure 3.4) HXD extends the bandpass of *Suzaku* with its nominal sensitivity over 10–600 keV with an effective area of ~ 260 cm^2 (Fig 3.5). HXD consists of 16 main detectors arranged as a 4 × 4 array and surrounding 20 BGO scintillators. Each unit consists of two types of sensors: four 21.5 mm × 21.5 mm, 2 mm thick silicon PIN diodes (10–70 keV) and four 24 mm × 24 mm, 5 mm thick Gadolinium Silicate (GSO) scintillators placed behind the PIN diodes (40–600 keV). BGO crystals are also placed underneath of the GSO sensors, and thus each well is a five-sided anti-coincidence system.

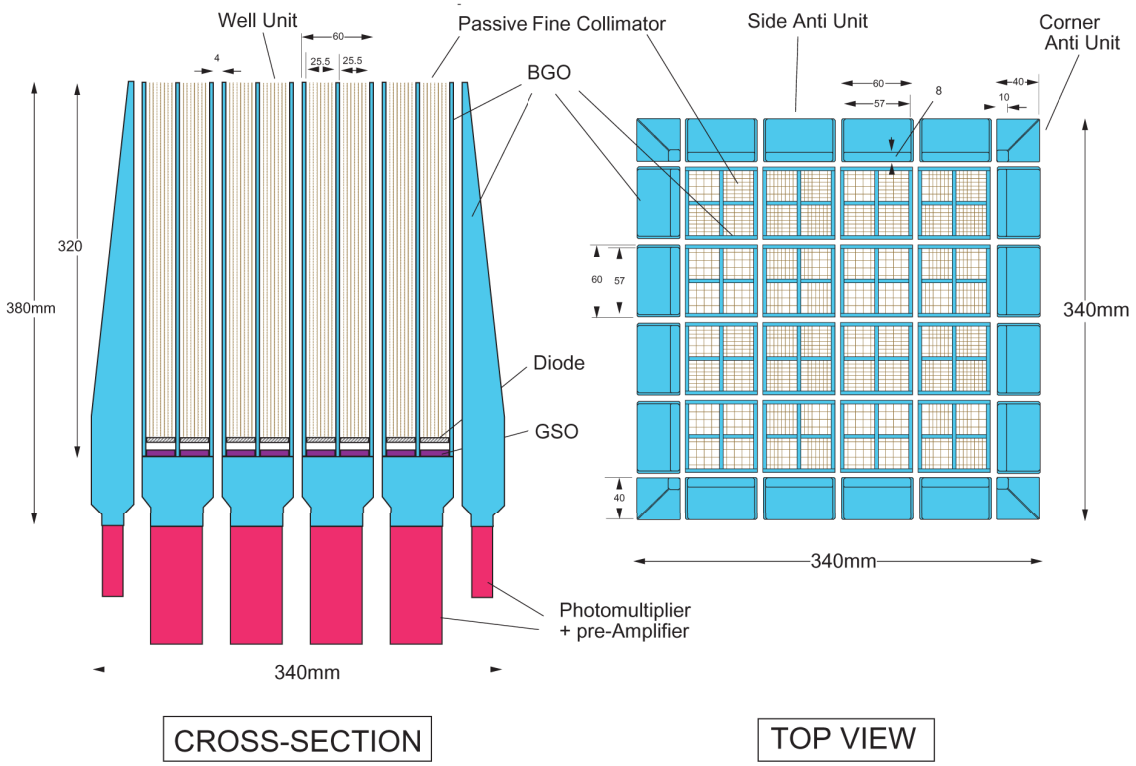

Figure 3.4: A schematic view of the Hard X-ray Detector onboard *Suzaku* [72].

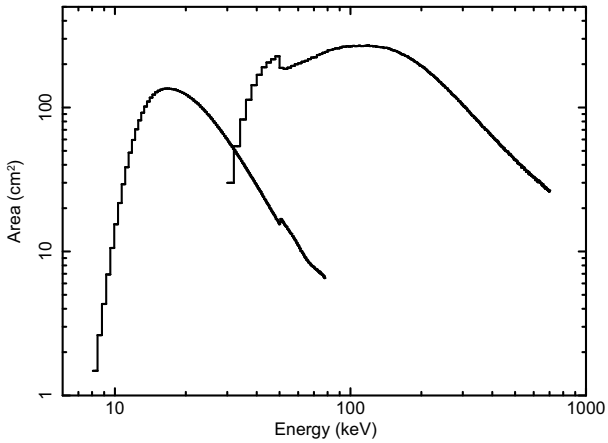

Figure 3.5: Total effective area of HXD detectors, PIN and GSO [72].

Both GSO and BGO scintillators of each unit are read by a single photomultiplier tube with pulse shape discrimination method, which utilizes a difference of the decay time of scintillations. The well-shaped configuration reduces background cosmic-ray particles and cosmic X-ray background emission.

The HXD field of view is actively collimated to $4.5^\circ \times 4.5^\circ$ by the well-shaped BGO scintillators[3] . At energies below ~ 100 keV, additional passive collimator, made of 50μm

[3] With the large area of the lateral BGO scintillators, HXD also performs as an all-sky monitor (the

thick phosphor bronze sheets, reduce the field of view further to $34' \times 34'$. The energy resolution is $\sim$ 4.0 keV (FWHM) for the PIN diodes and $7.6/\sqrt{E}$ % (FWHM, E is in MeV) for the GSO scintillators. A time resolution of both sensors of HXD is 61 μs. Though HXD is intended mainly to explore the faintest hard X-ray sources, it can also tolerate very bright sources up to $\sim$ 10 Crab.

Because HXD's bore-sight axis is shifted $\sim 3.5'$ from that of XISs, *Suzaku* supports two aim-points, XIS and HXD oriented. For the XIS, choosing the XIS aim-point provides a $\sim$ 10 % larger effective area than that expected with the HXD aim-point, and vice versa. Users can select either one of the two depending on their purposes.

3.3 *XMM-Newton*

The European Space Agency's (ESA) X-ray Multi-Mirror Mission (*XMM-Newton*) was launched by an Ariane 5 launcher in December 1999. Its orbit is highly elliptical with an apogee of 107,230 km, a perigee of 26,700 km, an inclination angle of 60.6°, an eccentricity of 0.60 and a period of 47.86 hours (prediction in May 2010; the orbit changes with time). The highly eccentric orbit allows long ($\sim$ 130 ks on average) uninterrupted observations. However, solar wind particles sometimes can affect observations depending on the solar activity.

XMM-Newton carries three types of science instrument: European Photon Imaging Camera (EPIC) [75, 76], Reflection Grating Spectrometer (RGS) [77] and Optical Monitor (OM) [78]. EPIC consists of three X-ray CCD cameras for imaging spectroscopy and photometry. There are two different types of camera, MOS (Metal Oxide Semiconductor) and pn. RGS comprises two essentially identical spectrometers for high-resolution X-ray spectroscopy and spectro-photometry. OM is a 30 cm optical/UV telescope for imaging and grism spectroscopy. The EPIC cameras and RGS spectrometers are placed on the focal planes of X-ray telescopes while OM has its own telescope. All EPIC cameras and OM are operated simultaneously. The instruments also can be operated independently in different data acquisition modes.

Since we used only EPIC cameras for this study, descriptions about RGS and OM are omitted hereafter in this section. Performance of EPIC MOS and pn cameras are summarized in Table 3.3.

EPIC cameras are co-aligned with a relative astrometry between the three cameras calibrated to better than $1 - 2''$ across the full field of view. Each of the three X-ray telescopes has its own point spread function and the HPD is slightly different each other

Wide-band All-sky Monitor, WAM), which can detect GRBs and other flaring sources.

Table 3.3: Properties of EPIC cameras onboard *XMM-Newton*.

Parameter	EPIC MOS1	EPIC MOS2	EPIC pn
Energy Range	0.15–12 keV	0.15–12 keV	0.15–15 keV
Effective Area (at 1.5 keV)	~ 550 cm^2	~ 550 cm^2	~ 1400 cm^2
Field of View	$30'$	$30'$	$30'$
Angular Resolution (HPD)	$13.8''$	$13.0''$	$15.2''$
Energy Resolution	~ 70 eV	~ 70 eV	~ 80 eV

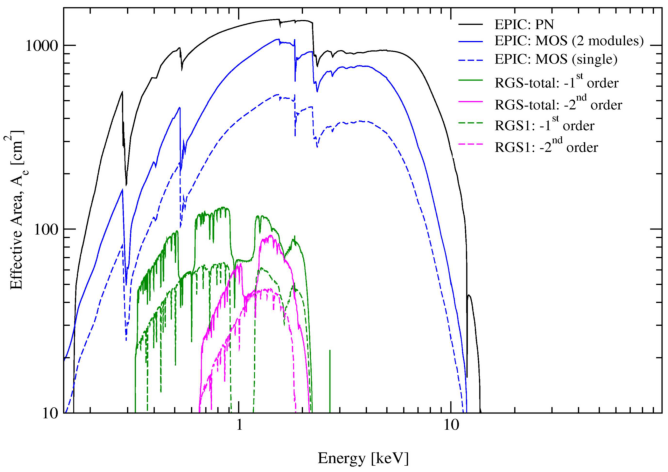

Figure 3.6: Total effective area of X-ray telescopes onboard *XMM-Newton* [79].

(Table 3.3). While the three X-ray telescopes are identical, the effective area of the MOS cameras is lower than that of the pn. This is mainly because X-ray photons are partially obscured by a grating assembly of the RGS inserted in X-ray paths between the telescope and the pn camera. Figure 3.6 shows the on-axis effective area as a function of energy. The EPIC and telescope system is most efficient in a 1.5–2.0 keV band.

The EPIC cameras offer the possibility to perform sensitive imaging observations over a field of view of $30'$ and the energy range from 0.15 to 15 keV with moderate spectral ($E/\Delta E \sim 20 - 50$) and angular resolution ($\sim 15''$ HPD). All EPIC cameras operate in photon counting mode with a fixed, mode dependent frame readout frequency, producing event lists. This allows for simultaneous imaging and non-dispersive spectroscopy due to the intrinsic energy resolution of the pixels. The two types of EPIC camera are different with the geometry (Figure 3.7), readout time, electrode structure and so on.

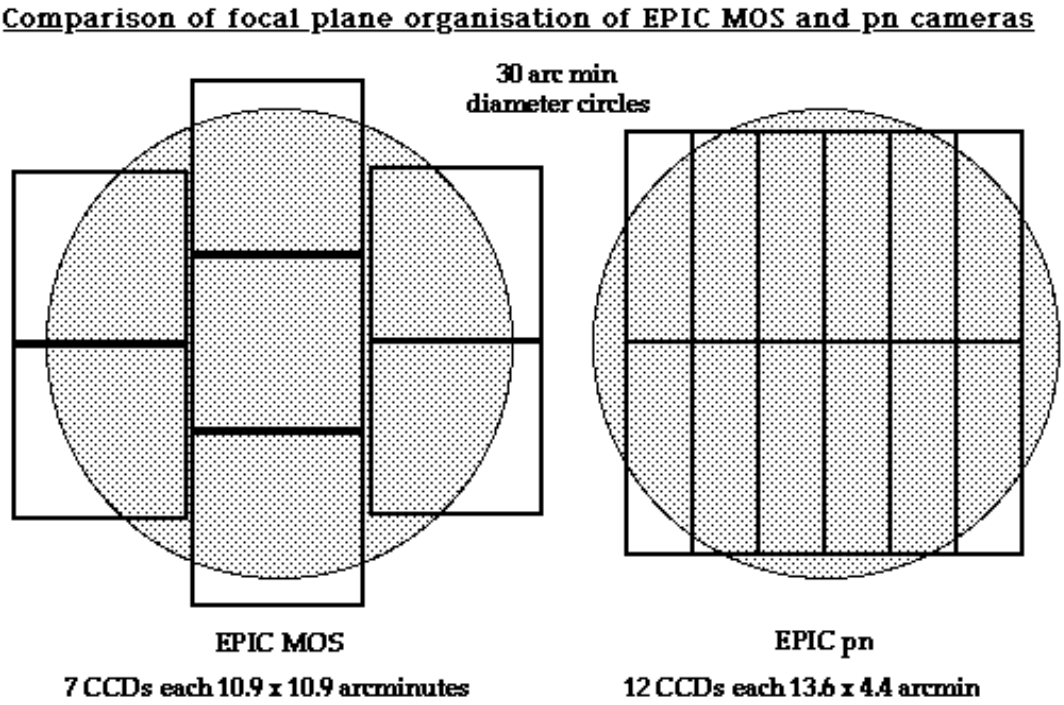

Figure 3.7: A rough sketch of the field of view of the two types of EPIC camera; MOS (left) and pn (right) [79]. The shaded circle depicts a 30′ diameter area.

The MOS chip arrays consist of seven individual identical, front-illuminated chips. The individual CCDs are not co-planar, but offset with respect to each other, following closely the sight curvature of the focal surface of the telescopes. As indicated above, the MOS cameras are mounted on those X-ray telescopes that also carry RGS assembly. Therefore they receive only 44 % of the reflected light. The MOS1 CCD6 has not been in operation since March 2005 because it had sustained significant damage by a possible debris impact and no events cannot be recorded.

The pn camera is a single silicon wafer with twelve back-illuminated CCD chips integrated. The readout of the pn chips (73.4 ms in Full frame mode) is much faster than that of the MOS cameras (2.6 s in Full frame mode) because each pixel column has its own readout node.

The MOS and pn cameras have various observation modes with smaller chip area to read out. Those modes give shorter readout time and thus they are suitable for timing observations or bright source observations. Since the cameras operate individually, users can select modes for each camera. The standard mode is called Full frame mode.

The EPIC background can be divided into stable components (cosmic X-ray background and a particle-induced component) and an external flaring component characterized by strong and rapid variability. The flaring component is currently attributed to soft

protons with the energy of less than a few hundred MeV which are funneled towards the detectors by the X-ray mirrors. Time intervals affected by the proton flares are encouraged to remove for the science analysis.

Photon pile-up, the arrival of more than one X-ray photon in one camera pixel or in adjacent pixels before it read out, can affect both the point spread function and the spectral response of EPIC. For the MOS Full frame mode, ~ 0.7 counts s^{-1} should not be exceeded. The point spread function is influenced by pile-up because in the core of the point source image many photons arrive at almost the same time (i.e. within one readout time), creating multi-pixel photon patterns which are rejected by the onboard software. This effect leads to a point source image with an artificial hole at its center. Pile-up effects also effects on the spectral shape because piled-up soft photons create artificial hard photons.

3.4 *Chandra X-ray Observatory*

The *Chandra X-ray Observatory* was launched by NASA's Space Shuttle Columbia in July 1999. The orbit is highly elliptical and varies with time. As of December 2008 the apogee height was $\sim$ 132,200 km and the perigee height was $\sim$ 16,700 km. The orbit allows for reasonably high observing efficiency as the satellite spends most of the time ($\sim$ 75 %) well above the radiation belts and long continuous observations ($\sim$ 160 ks) are made possible by the orbital period of 63.5 hours.

Chandra was designed to provide order-of-magnitude advances over previous X-ray astronomy missions with regards to spatial and spectral resolution. The High Resolution Mirror Assembly (HRMA) [80] produces images with a HPD of the point spread function of $< 0.5''$. The Advanced CCD Imaging Spectrometer (ACIS) [81] and the High Resolution Camera (HRC) [82] are placed on the focal plane of HRMA. The ACIS and HRC cannot be operated simultaneously. They are on board a single plate which moves their positions depending on the selected instrument. Two grating systems, the Low Energy Transmission Grating (LETG) [83] and the High Energy Transmission Grating (HETG) [84], offer resolving powers well in excess of 500 in the energy range from ≤ 0.1 to 10 keV. Since the HRC, LETG and HETG are not used in this study, their description is omitted hereafter.

The HRMA consists of a nested set of four Wolter-1 grazing-incidence X-ray mirror pairs, with the largest having a diameter of 1.2 m. The focal length is 10 m. The on-axis HPD is $\sim 0.3''$ at 1.5 keV. The point spread function has a faint halo extending to large angles, resulting from X-rays scattering from micro-roughness on the mirror surfaces. This scattering is energy dependent.

ACIS contains ten planar, 1024 × 1024 pixel CCDs; four arranged in a 2 × 2 array (ACIS-I) used for imaging, and six arrange in a 1 × 6 array (ACIS-S) used either for imaging or as a HETG grating readout. Currently any combination of up to six CCDs may be operated simultaneously. While all of ACIS-I chips are FI CCDs, ACIS-S consists of four FI and 2 BI CCDs, one of which is at the best focus position. The layout of the ACIS chips is shown in Figure 3.8. The CCDs are flat but the chips are positioned to fit the focal surface for ACIS-I and the Rowland circle of HETG for ACIS-S. The effective areas as a system of HRMA+ACIS are shown in Figure 3.9. The on-axis effective area is ~ 600 cm^2 at 1.5 keV for FI.

There are two ACIS operation modes. One is Timed Exposure (TE) and the other is Continuous Clocking (CC). The TE refers to the mode of operation wherein a CCD collects data (integrates) for a preselected amount of time, the Frame Time. Once this time interval has passed, the charge from the 1024 × 1024 active region is quickly (~ 41 ms) transferred to the frame store region and subsequently read out through 1024 serial registers. Frame times can be selected within a range of values between 0.2 to 10.0 seconds. The nominal and optimal time is 3.2 s. Since pileup effects also matter for the ACIS, shorter frame time is preferable for bright sources. The CC mode is provided to allow 3 ms timing at the expense of one dimension of spatial resolution. In this mode, one obtains 1 pixel × 1024 pixel images.

The large majority of observations are performed using Normal Point Mode, with dither selected. In this case *Chandra* line-of-sight will be commanded through a Lissajous pattern. Dithering distributes photons over many detector elements and serves several purposes: reduces uncertainty due to pixel to pixel variation in quantum efficiency; and allows sub-sampling of the image. Dither can be disabled for ACIS observations.

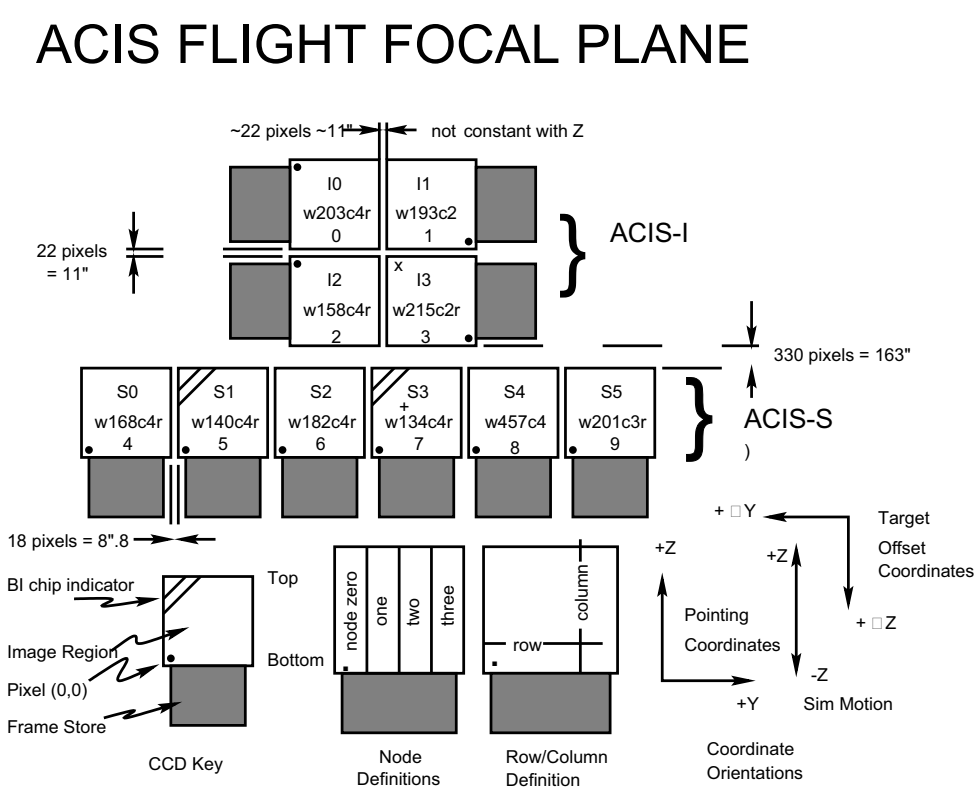

Figure 3.8: A schematic drawing of the ACIS focal plane. Note the nominal aimpoints: on S3 (the + mark) and on I3 (the x mark) [85].

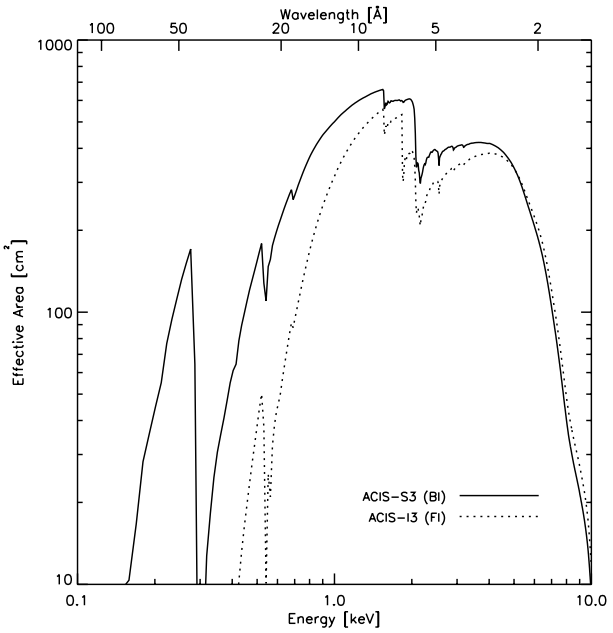

Figure 3.9: The on-axis effective areas of the HRMA/ACIS-I(FI), the HRMA/ACIS-S(BI) and HRMA/HRC [85].

Chapter 4

Observations and Data Analysis

4.1 Target selection

Our start point of the target selection is a list of pulsars whose gamma-ray pulsations were detected by the *Fermi* LAT (Table 2.1). First we removed all millisecond pulsars because we want to compare properties of younger normal pulsars. In addition, emissions of millisecond pulsars are too weak to obtain enough statistics for spectral analysis. We suggest more observations are necessary to discuss properties of gamma-ray millisecond pulsars.

Next, in order to compare pulsars' spectral properties in gamma-ray and X-ray bands, we checked if there are archival X-ray data for each pulsar by contemporary observatories: *Suzaku*, *XMM-Newton* and *Chandra*. We also took quick looks at existing X-ray data and excluded objects with much flux as to suffer pile-ups, objects suffering large background cosmic-ray proton flares, and objects not observed in standard full frame modes. Naturally, there were few X-ray coverages for pulsars newly discovered by *Fermi* LAT therefore we proposed and carried out *Suzaku* observations for some of the new pulsars (see §4.2.2).

The selection left 23 pulsars shown in Table 4.1 (15 pulsars discovered in gamma-ray and 8 pulsars already known in the radio band) out of 55 LAT pulsars. We performed gamma-ray spectral analyses with the LAT data only for those selected pulsars.

4.2 Data

4.2.1 *Fermi* LAT public data

All the observation data by *Fermi* LAT are released to the public. There are no proprietary data owned by the *Fermi* LAT Collaboration or guest observers. Among some kinds

Table 4.1: Pulsars analyzed in this study.

JName	Type[a]	Used X-ray Data
J0007+7303	g	*XMM-Newton* and *Chandra*[b]
J0205+6449	r	*XMM-Newton*
J0357+32	g	*Suzaku*
J0633+0632	g	*Suzaku*
J0633+1746	g	*XMM-Newton*
J1022−5746	g	*Chandra*
J1028−5819	r	*Suzaku*
J1048−5832	r	*XMM-Newton* and *Chandra*[b]
J1413−6205	g	*Suzaku*
J1418−6058	g	*XMM-Newton*
J1459−60	g	*Suzaku*
J1509−5850	r	*XMM-Newton*
J1826−1256	g	*Chandra*
J1833−1034	r	*XMM-Newton*
J1836+5925	g	*Chandra*
J1907+06	g	*Suzaku*
J1952+3252	r	*XMM-Newton*
J1954+2836	g	*Suzaku*
J1958+2846	g	*Suzaku*
J2021+3651	r	*XMM-Newton*
J2032+4127	g	*Chandra*
J2229+6114	r	*Chandra*
J2238+59	g	*Suzaku*

[a] See Table 2.1.

[b] For these sources, data from two observatories were used for better statistics.

of data formats, using FITS [86] format data is the easiest way. Data analysis requires calibrated event data files called "FT1" and spacecraft data files called "FT2". The FT1 files contain each photon's energy, reconstructed incoming direction, arrival time, Event Class and so on. The FT2 files contain the spacecraft's position, attitude and so on for every 30 seconds.

Event data can be extracted at the SLAC Astro Server [87]. Users can request their own conditions (i.e. center coordinates and radius of a region, time intervals and energy ranges) to get minimum necessary data. We extracted Diffuse Class events reprocessed with a reconstruction procedure called Pass 6 for each selected pulsar with a circular region centered at the pulsar location with a radius of 15°. The time interval is from 15:43 of August 4, 2008 (start of the all-sky observations) to 0:00 of September 3, 2009. The LAT basically carried out continuous all-sky observations but a few ARRs and calibration runs were performed during this period. We did not include data of calibration runs at all.

4.2.2 *Suzaku* observations

Since some of the new pulsars lack deep X-ray follow-up observations, we proposed observations with *Suzaku* at the fourth Announcement of Opportunity (AO4). Our proposal includes eleven new pulsars, a known radio pulsar (PSR J1028−5819), and two objects without any associations[1] . The 360-kilosecond proposal was fully accepted with an evaluation of Priority A and twelve sources have been observed as of December 2009[2] .

Our main objectives were detections of X-ray counterparts of the new pulsars and their spectroscopy with XIS. Therefore all observations were performed with XIS-nominal pointing and normal mode of XIS without any special options (window, burst or timing options). The aim positions were set to the center coordinates of localization error circles reported by the LAT Collaboration. The best coordinates of some pulsars were slightly improved after the *Suzaku* observations due to further gamma-ray analysis .

4.2.3 Archival data of *XMM-Newton* and *Chandra*

Archival data of *XMM-Newton* and *Chandra* can be accessed at *XMM-Newton* Science Operations Centre [88] and *Chandra* X-ray Center [89], respectively. We utilized observations listed in Tables 4.3 and 4.4.

[1] This study does not cover those two unknown objects.

[2] Two remaining objects are PSR J1741−2054 and J1813−1246. *Suzaku* has a little chance of observations for sources at lower ecliptic latitude due to the limitation of the sun angle relative to the solar paddles. The two pulsars will be observed by the end of March 2010.

Table 4.2: Used observation data by *Suzaku*.

JName	ID	R.A. (°)[a]	Dec. (°)[a]	Start Time	Exp (ks)[b]	PI[c]
J0357+32	504041010	59.4720	32.0900	2009-08-02 19:41:12	21.3	Kawai
J0633+0632	504047010	98.4346	6.5402	2009-04-10 22:02:08	24.0	Kawai
J1028−5819	504045010	157.1332	−58.3130	2009-07-08 08:12:56	22.8	Kawai
J1413−6205	504054010	213.3355	−62.0808	2009-07-24 21:42:28	44.2	Kawai
J1459−60	504055010	224.8822	−60.8823	2009-08-06 16:59:15	42.3	Kawai
J1732−31	504049010	263.1417	−31.5448	2009-09-08 03:36:55	37.2	Kawai
J1907+06	504043010	286.9632	6.0295	2009-04-15 03:40:44	24.5	Kawai
J1954+2836	504046010	298.5570	28.6365	2009-04-07 18:02:07	20.5	Kawai
J1958+2846	504044010	299.6429	28.7759	2009-05-23 15:19:43	38.7	Kawai
J2238+59	504048010	339.5988	59.0734	2009-06-19 04:27:31	26.3	Kawai

[a] Coordinates of nominal aim points.

[b] Total exposure time.

[c] Principal Investigator.

Evey *XMM-Newton* observations used here were performed with at least one of the EPIC camera with the Full Frame mode. We did not use any Window mode data because interested regions were not fully covered by the exposed CCD area. For *Chandra* data, we used ACIS-I or ACIS-S observations with the Timed Exposure mode. No HRC data were used.

4.3 Analysis procedure

In order to handle data systematically, standard analysis procedure was decided. Here we omit details about tasks and their parameters. See handbooks of the software packages for comprehensive explanations.

4.3.1 *Fermi* LAT data

The *Fermi* LAT Collaboration distributes the ScienceTools, a standard software package for handling and analyzing *Fermi* LAT data [90]. We used version v9r15p4 in this study. For the instrumental response function, P6_V3_DIFFUSE was used. The procedure of the analysis is as follows.

Table 4.3: Used observation data by *XMM-Newton*.

JName	ID	R.A. (°)	Dec. (°)	Start Time	Exp. (ks)	PI
J0007+7303	0011430201	1.7583	73.0497	2002-02-21 18:56:32	41.5	Slane
J0205+6449	0153752101	31.4083	64.8278	2002-09-13 10:37:32	21.4	Jansen
J0633+1746	0111170101	98.4758	17.7703	2002-04-04 16:40:19	103.3	Kaastra
	0201350101	98.4758	17.7703	2004-03-13 14:55:08	26.2	Halpern
	0311591001	98.4760	17.7706	2006-03-17 05:03:52	34.9	Schartel
	0400260201	98.4760	17.7706	2006-10-02 07:04:22	20.3	Halpern
	0400260301	98.4760	17.7706	2007-03-11 11:28:50	24.4	Halpern
	0501270201	98.4762	17.7706	2007-09-18 08:33:36	24.9	Halpern
	0501270301	98.4762	17.7706	2008-03-08 15:28:16	20.8	Halpern
J0659+1414	0112200101	104.9500	14.2394	2001-10-23 09:29:06	40.9	Mason
J1048−5832	0054540101	162.0525	−58.5344	2002-08-10 06:53:36	31.2	Gaensler
J1418−6058	0151100201	214.6658	−60.9675	2003-03-10 11:55:43	27.2	Roberts
J1509−5850	0500630101	227.3630	−58.8489	2008-01-28 06:46:15	79.9	Kargaltsev
	0500630301	227.3630	−58.8489	2008-03-01 21:16:43	49.8	Kargaltsev
J1833−1034	0122700101	278.3875	−10.5694	2000-04-07 12:36:39	35.3	Jansen
J1952+3252	0204070101	298.2429	32.8779	2004-05-11 12:43:29	10.4	Zane
J2021+3651	0404540101	305.2728	36.8513	2006-05-19 10:39:36	34.6	Roberts
	0404540201	305.2728	36.8513	2006-05-21 10:38:50	34.3	Roberts

Table 4.4: Used observation data by *Chandra*.

JName	ID	R.A. (°)	Dec. (°)	Start Time	Exp. (ks)	PI
J0007+7303	3835	1.7825	73.0527	2003-04-13 10:08:50	50.1	Halpern
J1022−5746	3501	156.0022	−57.7549	2003-08-23 18:20:19	36.6	Garmire
	6410	155.9843	−57.7612	2006-09-05 15:50:57	50.0	Rauw
	6411	155.9869	−57.7598	2006-09-28 05:45:16	50.0	Rauw
J1048−5832	3842	162.0386	−58.5277	2003-10-08 22:37:30	36.6	Kaspi
J1826−1256	3851	276.4606	−12.9987	2003-02-17 20:03:44	15.1	Romani
	7641	276.5253	−12.9517	2007-07-26 16:04:16	74.8	Roberts
J1836+5925	2764	279.0680	59.4332	2002-03-06 02:20:57	28.1	Halpern
J2032+4127	4501	308.0240	41.5108	2004-07-19 02:03:29	49.3	Butt
J2229+6114	2787	337.3040	61.2307	2002-03-15 12:23:57	95.1	Halpern

1. Add selection criteria on the extracted photon event data.
2. Make good time intervals (GTIs).
3. Create a livetime hypercube and an exposure map.
4. Write a model file and perform fitting.
5. Remove objects that resulted in low significance levels and refit.

First, following selections were used to extracted event data with the gtselect task. We selected events with

- energies between 200 MeV and 100 GeV,
- distances less than 10° from the target pulsar and
- incident angles less than 105° from the zenith.

In the first criterion, the lower limit is required to reduce calibration uncertainties and the upper limit is chosen to match that of the template model for isotropic background. The extracted sky region is called the region of interest (RoI). The extraction radius in the second criterion may be controversial. The larger the RoI is, the more accurate results one may obtain. However larger RoI needs longer CPU times for model fitting calculations. We have tested the effects of the radius on the fit results and concluded that 10° is the minimum requirement, which agrees with the recommendation from the

Fermi LAT Collaboration. We adopted 10° radius to save computation resources and time. The third criterion is necessary to avoid confusion of the earth's atmospheric or albedo gamma-rays.

Next, good time intervals (GTIs) were made with a gtmktime task. This task adds a GTI extension to each FT1 file. Events not recorded in GTIs will not handled in further analysis tasks. The filter expression of PSR J0007+7303, for example, was

```
IN_SAA!=T && DATA_QUAL==1 && LAT_CONFIG==1 &&
(ANGSEP(RA_ZENITH,DEC_ZENITH,1.75483,73.05126)+10<105 || ABS(ROCK_ANGLE)<43)
```

`IN_SAA!=T` is for the time intervals when the spacecraft is out the South Atlantic Anomaly (SAA). `DATA_QUAL==1` and `LAT_CONFIG==1` mean that no significant problems were found and the operation configuration of the LAT is suitable for scientific analysis, respectively, on a per-run basis. The last two conditions are about the attitude of the spacecraft. The former one means the entire RoI is above the confusion limit of the albedo gamma-rays (zenith angle $< 105°$). The coordinates of the target and the radius of the RoI should be fitted with each analysis. The latter one means the absolute value of the rocking angle is smaller than 43° [3] .

In the next step, a gtltcube task calculates a "livetime hypercube", which is integrated livetime as a function of the sky position and the incident angle in the spacecraft coordinates. Then a gtexpmap task calculates an exposure map for each energy range based on the livetime hypercube. These tasks are necessary to calculate each source's flux and number of predicted photons from the fitted spectral model. We set parameters dcostheta = 0.025 and binsz = 0.5 in gtltcube and srcrad = 20, nlong = 120, nlat = 120 and nenergies = 20 in gtexpmap.

Then we wrote a model file containing spectral functions and positions in the sky for each objects within 12° from the center coordinate. This means that objects near the edge of the RoI are included, too. It is because the large point spread function of the LAT (Figure 3.1) can cause leakage of photons of nearby objects into the RoI, especially in the lower energy ranges. In the model, we included sources in the 11-month source catalog, Galactic diffuse emission model (gll_iem_v02.fit) and isotropic background model (isotropic_iem_v02.txt). The normalization parameters of the two diffuse emission models were free. The spectra of the point sources except the pulsars were modeled with PowerLaw, whose initial parameters were Prefactor = 1×10^{-12}, Index = -2.3 and Scale = 1000, where Prefactor and Index were set free. The pulsar spectra were modeled with

[3] Due to the change of the rocking angle, the limit should be 52° when the analysis data include events taken after 3 September 2009

PLSuperExpCutoff, whose initial parameters were Prefactor $= 1 \times 10^{-10}$, Index1 $= -1.6$, Scale $= 1000$, Cutoff $= 2500$ and Index2 $= 1$, where Prefactor, Index1 and Cutoff were set free. For the model fitting, a gtlike task was run with the DRMNFB optimizer and a fit tolerance of 10^{-5}.

After the first fit, objects resulted in low significance (test statistics < 9) were taken away from the model file and gtlike was run again with the NEWMINUIT optimizer and a fit tolerance of 10^{-10}. If objects with low significance remain, the same procedure was iterated.

4.3.2 X-ray data

Suzaku data

We used the HEAsoft version 6.6.3 [91] and *Suzaku* CALDB released on 13 August 2009 [92]. The source and background events were extracted from the cleaned event files of XIS with energies in 0.5 – 10 keV. The extracted regions differ according to the sources (see §5.2). Tasks xisrmfgen and xissimarfgen were used to calculate redistribution matrix functions (RMFs) and ancillary response files (ARFs). Tasks mathpha, marfrmf and addrmf were used to add spectra and response files of the two FI XISs (XIS0 and XIS3).

XMM-Newton data

We used *XMM-Newton* Science Analysis Software package version 9.0.0 [94] for analysis of the *XMM-Newton* data. Tasks cifbuild, odfingest, epchain and emchain were run for event reduction. For the GTI selection, first we extracted events with the condition `(PI in [10000:12000]) && #XMMEA_EP && PATTERN==0` for the PN camera and with `(PI>10000) && #XMMEA_EM && PATTERN==0` for the MOS cameras. In the higher energy band (> 10 keV), the proton background dominates. The light curves for the extracted events were drawn with a 100 s binning. We removed time intervals where the count rate is higher than 0.5 Hz for PN and 0.2 Hz for MOS. For the spectral analysis, 0.5 – 10 keV events with `(PATTERN<=4) && (FLAG==0)` and `(PATTERN<=12) && (FLAG==0)` were extracted for PN and MOS, respectively. Extracted source and background regions are presented in §5.2. Tasks rmfgen, arfgen and backscale were run to calculate RMFs, ARFs and area of the extracted regions.

Chandra data

We used *Chandra* Interactive Analysis of Observations package version 4.1 [95] and CALDB version 4.1.4 [96] for analysis of the *Chandra* data. We did not use the ready-made

dataset. We performed event reduction and filtering by ourselves with tasks acis_process_events and dmcopy. For the grade filter, events were screened out with status = 0 and grade $= 0, 2, 3, 4$ or 6. Then a specextract task was run to make spectra, RMFs and ARFs for source and background regions.

The source spectra were binned so as to several tens of photons per energy bin after subtracting background spectra. For spectral fitting, xspec version 11.3.2 [93] was used. In most cases, there are several datasets like XIS0+3 and XIS1 for *Suzaku*, and MOS1, MOS2 and pn for *XMM-Newton*. These spectra are fitted simultaneously.

Chapter 5

Results

5.1 Discovery of X-ray counterparts for LAT pulsars

Before presenting the results of spectral fitting, we compare X-ray images with the localization errors of the pulsars obtained from the gamma-ray photon arrival time analysis by the *Fermi* LAT Collaboration. Images taken by XIS0 and XIS3 were overlaid to find X-ray counterparts. We searched for counterparts in two bands, 0.5–2 keV and 2–10 keV. Figures 5.1 – 5.10 are XIS images with ellipses of gamma-ray localization errors and positions of probable X-ray counterparts. Note that the errors of gamma-ray analysis are preliminary and systematic errors have not been estimated yet. Thus we use errors five times larger than the reported 1σ errors for more reliable estimates.

We conclude that *Suzaku* observations found probable X-ray counterparts of the new LAT pulsars for the first time. In addition to the new gamma-ray pulsars, we report the first clear detection of the X-ray counterpart for PSR J1028−5819, which was recently discovered in radio observation [97] before the LAT detection and there was only a short Swift observation for the source. Coordinates of discovered X-ray counterparts are summarized in Table 5.1. The 'Band' column in Table 5.1 shows which band is used to determine the coordinate. Due to few number of photons from the counterparts and the moderate point spread function of *Suzaku* XIS, the localization error is quite large, about $10''$. We suggest that followup observations with *Chandra* are necessary to know more accurate coordinates.

By the eye inspections, there seem to be extended emissions around PSR J0633+0632, PSR J1028−5819 and PSR J1732−31, which are candidates for pulsar wind nebulae.

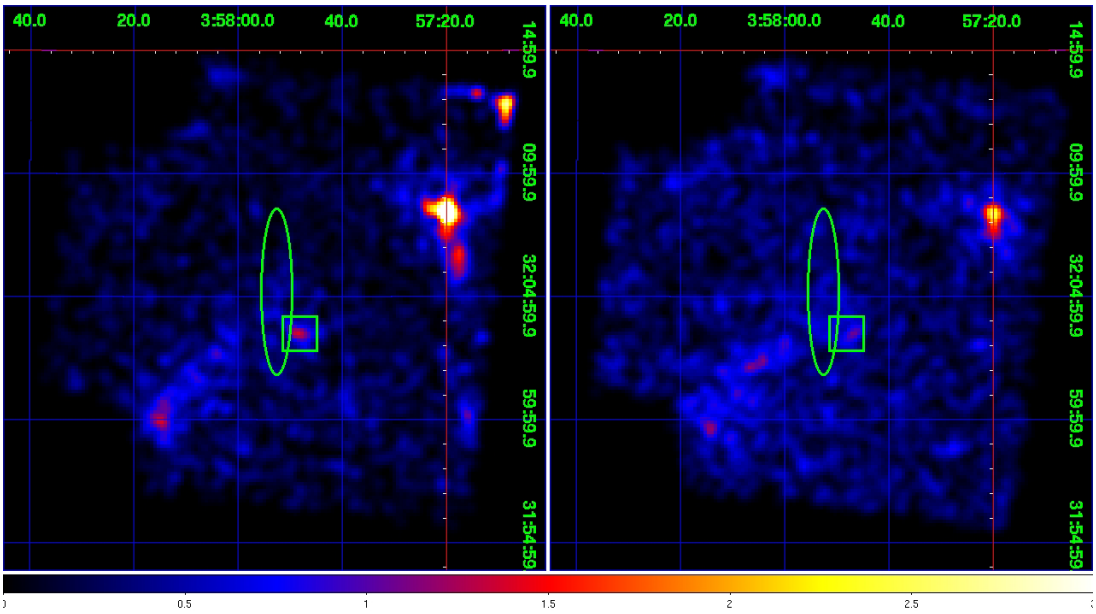

Figure 5.1: *Suzaku* XIS0+3 images of PSR J0357+32 in the energy band of 0.5–2 keV (left) and 2–10 keV (right). The ellipse shows a position error of the pulsar obtained in a gamma-ray timing analysis but the radius is 5 time larger than the reported value (only 1σ statistical error) for more reliable estimate. The box shows a position of the X-ray counterpart of the pulsar. Find its coordinates in Table 5.1.

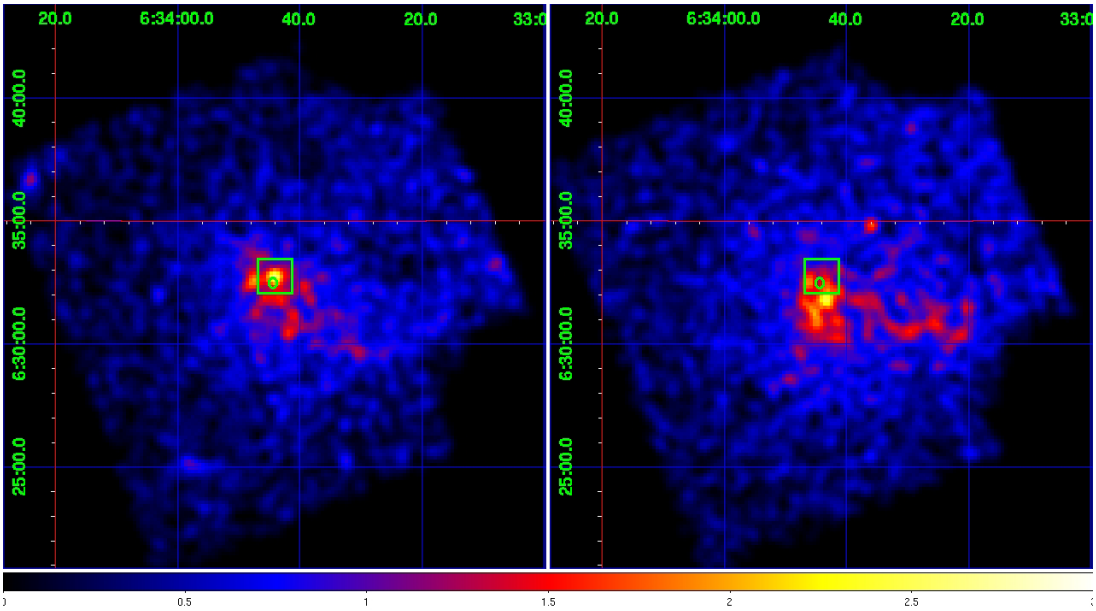

Figure 5.2: Same as Figure 5.1, but for PSR J0633+0632.

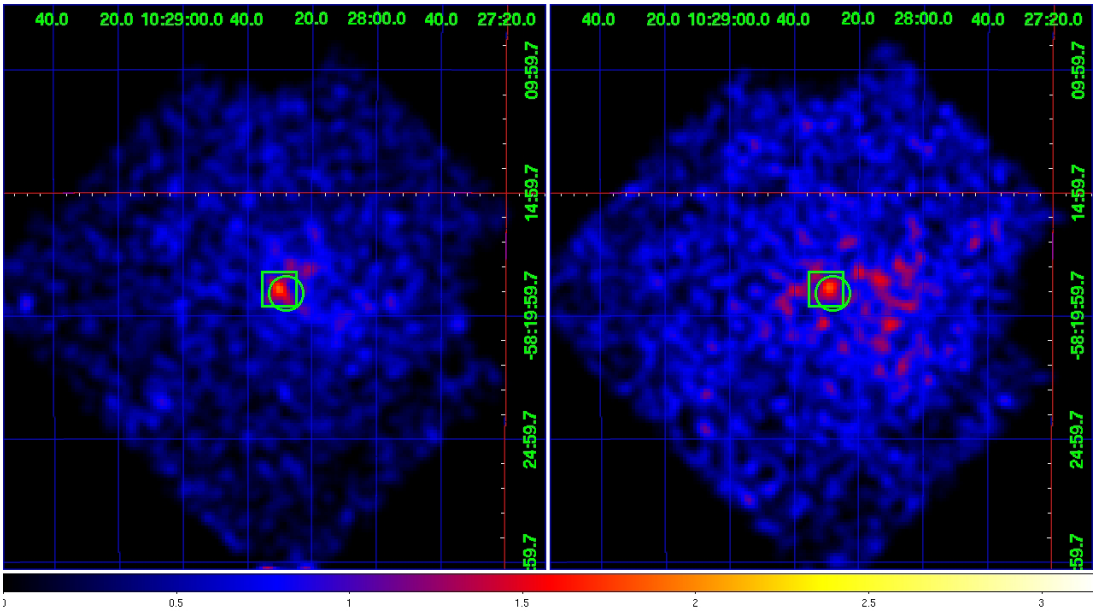

Figure 5.3: Same as Figure 5.1, but for PSR J1028–5819. This is a radio pulsar detected in 2008 [97]. The center of the circle corresponds to the radio position.

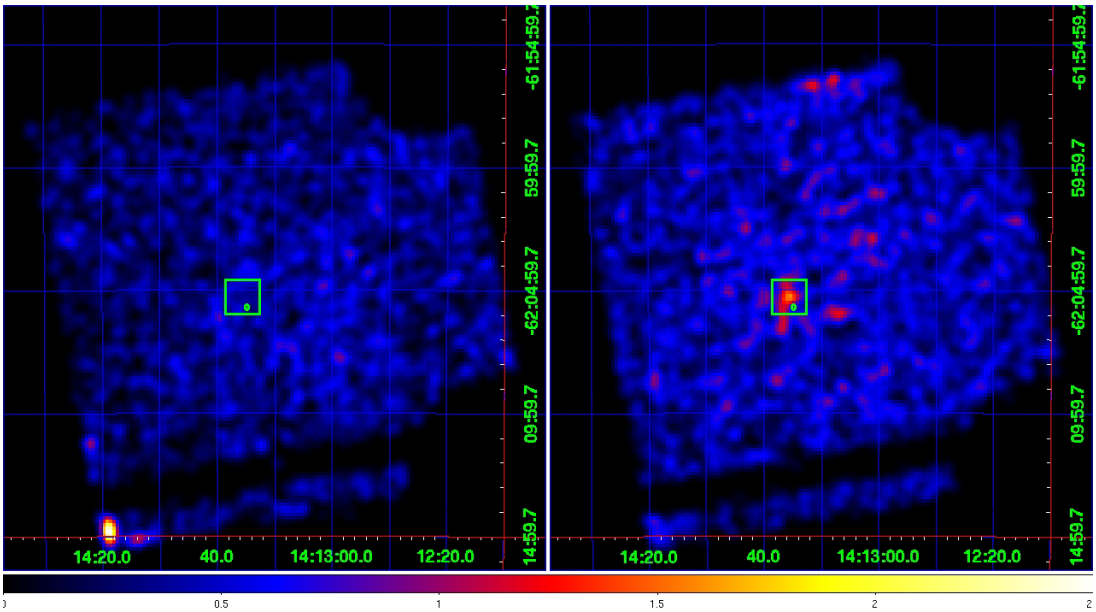

Figure 5.4: Same as Figure 5.1, but for PSR J1413–6205.

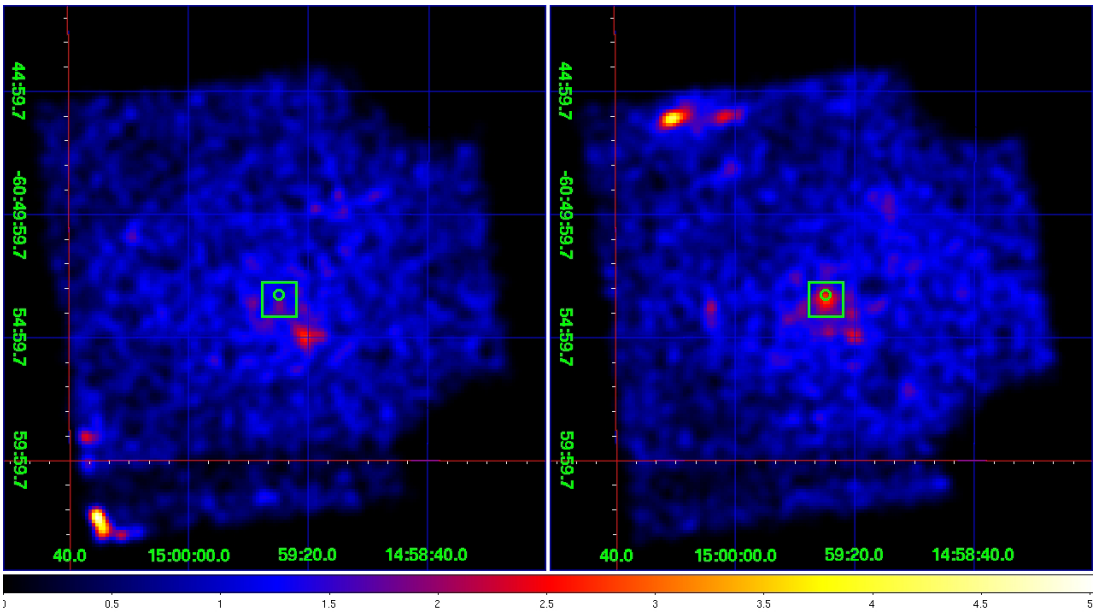

Figure 5.5: Same as Figure 5.1, but for PSR J1459–60.

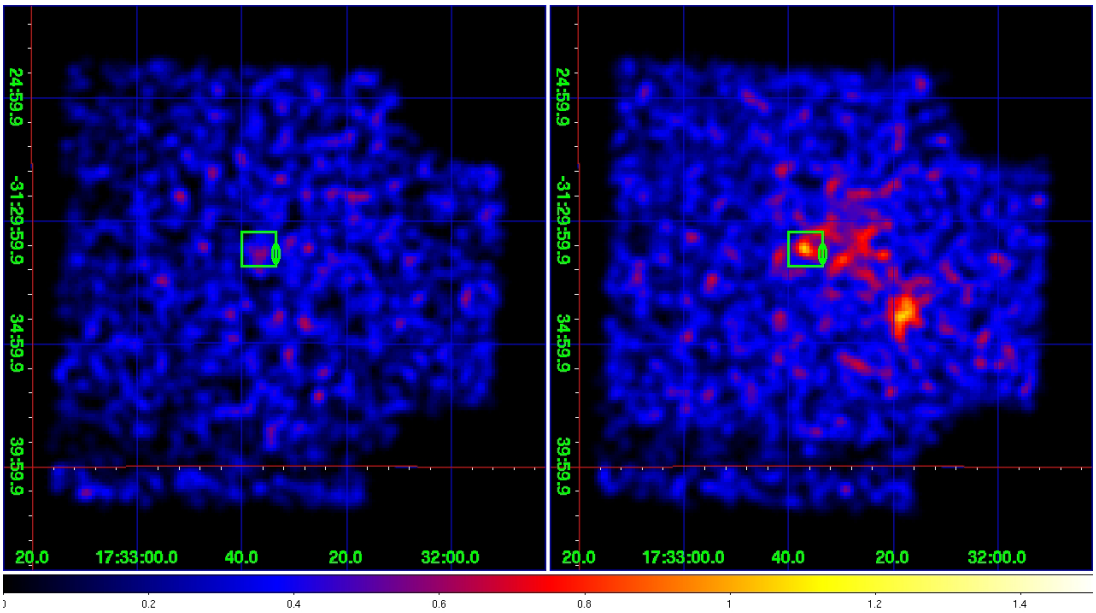

Figure 5.6: Same as Figure 5.1, but for PSR J1732–31.

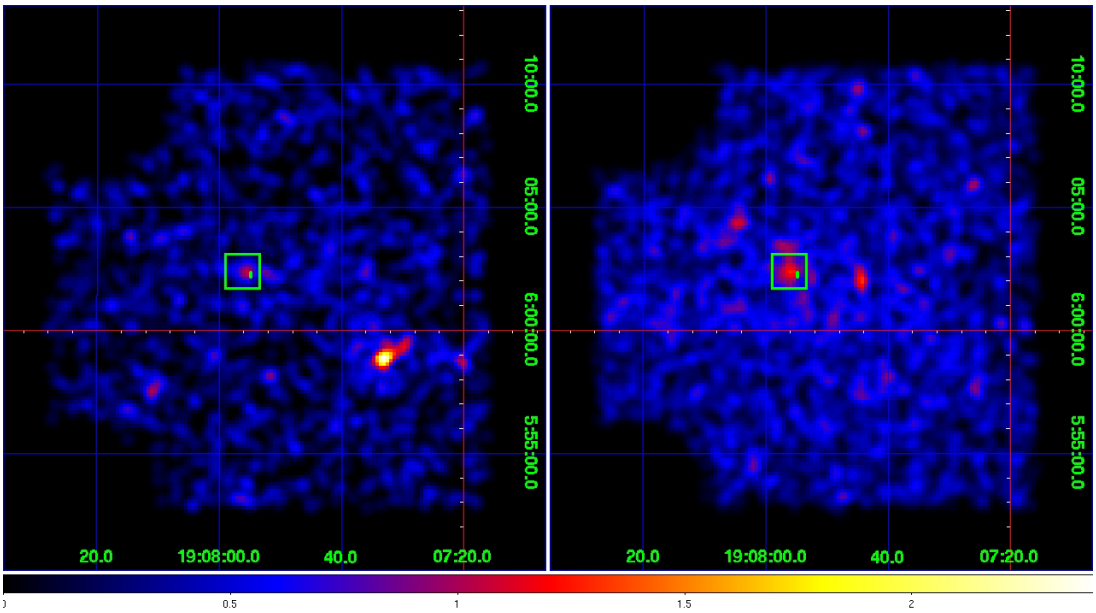

Figure 5.7: Same as Figure 5.1, but for PSR J1907+06.

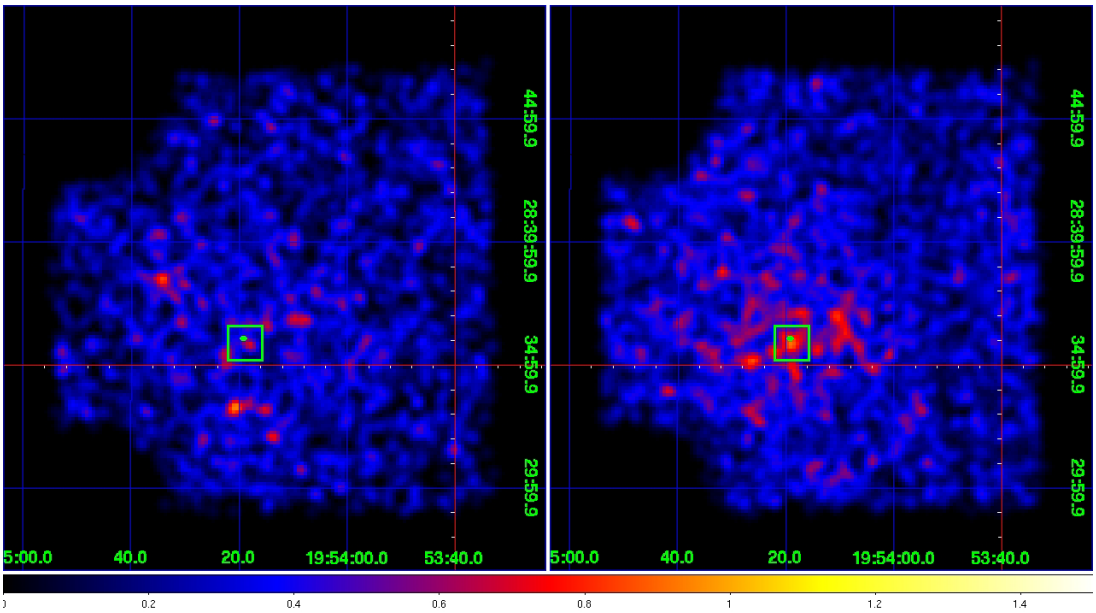

Figure 5.8: Same as Figure 5.1, but for PSR J1954+2836.

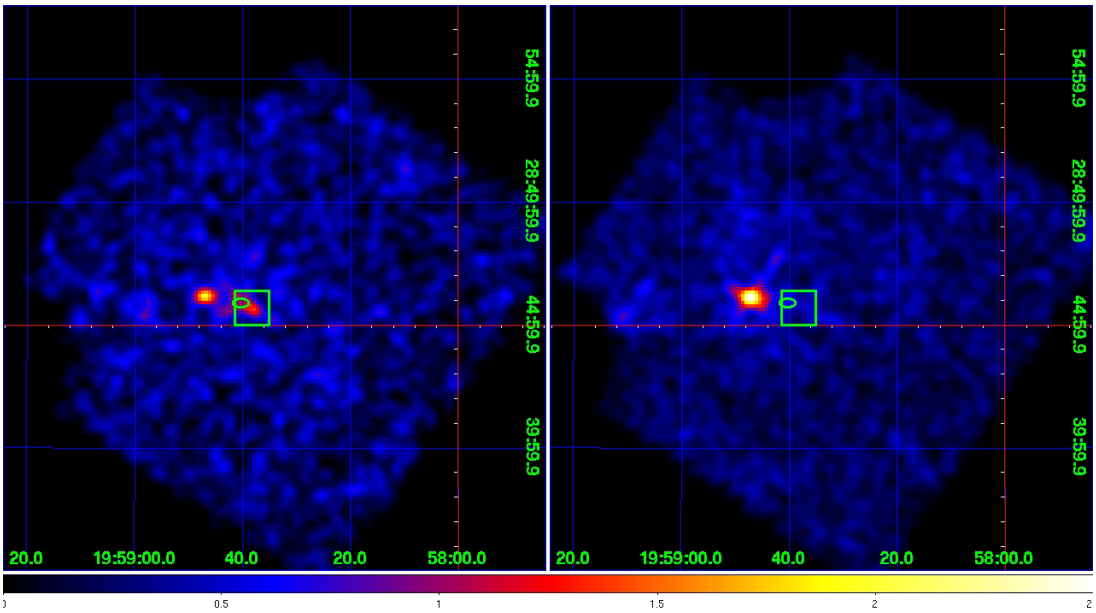

Figure 5.9: Same as Figure 5.1, but for PSR J1958+2846.

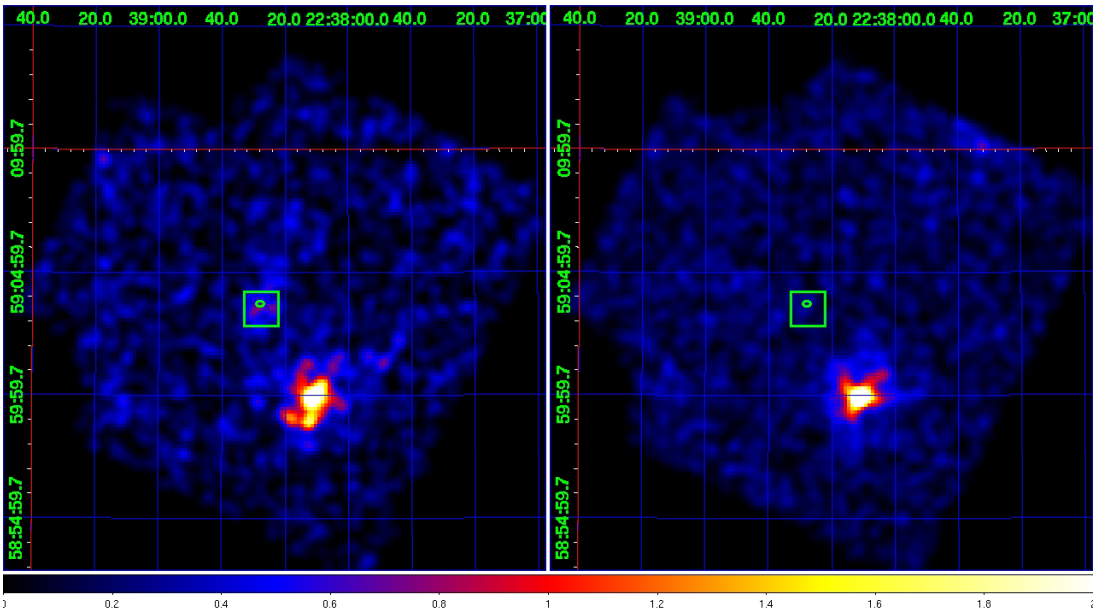

Figure 5.10: Same as Figure 5.1, but for PSR J2238+59.

Table 5.1: Coordinates of probable X-ray counterparts of new LAT pulsars discovered by *Suzaku* XIS. The positional error is $\sim 10''$. The "Band" column shows which energy band is used to determine the coordinates.

JName	R.A. $(^\circ)^a$	Dec. $(^\circ)^a$	Band
J0357+32	59.45082	32.05786	$0.5-2$ keV
J0633+0632	98.43343	6.54599	$0.5-2$ keV
J1028−5819	157.12548	−58.31532	$0.5-2$ keV
J1413−6205	213.38003	−62.08774	$2-10$ keV
J1459−60	224.87387	−60.89099	$2-10$ keV
J1732−31	263.15325	−31.51932	$2-10$ keV
J1907+06	286.98416	6.03992	$2-10$ keV
J1954+2836	298.57876	28.59828	$2-10$ keV
J1958+2846	299.65941	28.76142	$0.5-2$ keV
J2238+59	339.61457	59.05835	$0.5-2$ keV

5.2 Results from spectral fitting

Gamma-ray spectra were modeled with a power-law with an exponential cutoff function

$$\frac{dN}{dE} = K E_{\rm GeV}^{-\Gamma} \exp\left(-\frac{E}{E_{\rm cut}}\right),$$

where the energy $E_{\rm GeV}$ is scaled with 1 GeV. A scaling factor K is a differential flux at 1 GeV in the unit of photon cm^{-2} s^{-1} MeV^{-1}. Parameters Γ and $E_{\rm cut}$ are called photon index and cutoff energy, respectively.

Obtained gamma-ray spectral parameters are summarized in Table 5.2. All sources have hard spectra with a photon index of less than 2 and a cutoff energy of a few GeV. Typical photon flux and energy flux are $\sim 10^{-7}$ photons cm^{-2} s^{-1} and $\sim 10^{-10}$ ergs cm^{-2} s^{-1}, respectively.

X-ray emission from neutron stars is often modeled with blackbody radiation and a phenomenological power-law function. Although there are fine structures in PWNs, X-ray emission from PWNs can be generally modeled with a single power-law function[1] . Therefore X-ray spectra were tested with two models; absorbed power-law function (`wabs*pegpwrlw` in xspec)

$$\frac{dN}{dE} = \exp\left[-N_{\rm H}\cdot\sigma\left(E\right)\right] \times \frac{K_{\rm pl}\left(-\Gamma+2\right)E^{-\Gamma}}{E_2^{-\Gamma+2}-E_1^{-\Gamma+2}}$$

[1] Some PWNs are known to have fine structures and spectral variations in them.

Table 5.2: Fit parameters from gamma-ray spectral analysis. Errors are only statistical ones with 1σ confidence level.

JName	K	Γ	$E_{\rm cut}$	$F_{\rm ph}$	$F_{\rm E}$	TS
J0007+7303	8.03 ± 0.22	1.50 ± 0.03	4.54 ± 0.32	3.86 ± 0.11	4.05 ± 0.08	17908
J0205+6449	1.03 ± 0.20	2.06 ± 0.18	3.55 ± 1.62	1.01 ± 0.17	0.52 ± 0.05	345
J0357+32	3.61 ± 1.27	1.36 ± 0.28	1.04 ± 0.31	1.03 ± 0.15	0.63 ± 0.04	1295
J0633+0632	2.91 ± 0.20	1.65 ± 0.09	3.27 ± 0.49	1.59 ± 0.15	1.21 ± 0.06	1672
J0633+1746	120.18 ± 0.89	1.31 ± 0.01	2.44 ± 0.03	41.95 ± 0.24	41.33 ± 0.19	367408
J1022−5746	5.16 ± 0.57	1.73 ± 0.12	2.92 ± 0.64	3.07 ± 0.34	2.06 ± 0.12	1308
J1028−5819	5.55 ± 0.39	1.70 ± 0.09	3.54 ± 0.56	3.28 ± 0.31	2.42 ± 0.11	1976
J1048−5832	5.33 ± 0.46	1.53 ± 0.11	2.60 ± 0.41	2.43 ± 0.25	1.92 ± 0.10	1987
J1413−6205	4.58 ± 0.93	1.34 ± 0.43	2.89 ± 1.62	1.72 ± 0.65	1.78 ± 0.26	1106
J1418−6058	8.31 ± 0.89	1.56 ± 0.19	2.84 ± 0.68	3.96 ± 0.85	3.16 ± 0.33	1541
J1459−60	3.13 ± 0.41	1.88 ± 0.14	2.82 ± 0.74	2.27 ± 0.29	1.31 ± 0.09	811
J1509−5850	3.26 ± 0.34	1.68 ± 0.21	3.73 ± 1.19	1.88 ± 0.47	1.45 ± 0.17	703
J1826−1256	12.13 ± 0.79	1.56 ± 0.07	2.38 ± 0.25	5.59 ± 0.37	4.15 ± 0.14	3022
J1833−1034	1.64 ± 0.28	1.39 ± 0.23	3.09 ± 0.89	0.66 ± 0.17	0.66 ± 0.08	185
J1836+5925	18.51 ± 0.54	1.30 ± 0.03	2.19 ± 0.09	6.24 ± 0.11	5.84 ± 0.07	45359
J1907+06	6.76 ± 0.44	1.76 ± 0.07	3.75 ± 0.57	4.35 ± 0.32	3.05 ± 0.12	2420
J1952+3252	3.71 ± 0.23	1.59 ± 0.07	2.94 ± 0.35	1.84 ± 0.13	1.44 ± 0.06	2074
J1954+2836	2.54 ± 0.30	1.47 ± 0.22	3.00 ± 0.87	1.10 ± 0.25	1.00 ± 0.10	777
J1958+2846	2.99 ± 1.24	1.16 ± 0.63	1.85 ± 1.24	0.83 ± 0.37	0.82 ± 0.15	688
J2021+3651	14.01 ± 0.61	1.70 ± 0.05	2.81 ± 0.23	7.99 ± 0.34	5.44 ± 0.12	8954

Table 5.2: Continued.

JName	K	Γ	$E_{\rm cut}$	$F_{\rm ph}$	$F_{\rm E}$	TS
J2032+4127	2.84 ± 0.21	1.93 ± 0.24	10.64 ± 6.89	2.46 ± 0.89	1.87 ± 0.32	1151
J2229+6114	4.92 ± 0.25	1.90 ± 0.05	4.48 ± 0.61	3.86 ± 0.20	2.47 ± 0.07	3907
J2238+59	2.15 ± 0.31	1.62 ± 0.15	2.39 ± 0.56	1.08 ± 0.15	0.75 ± 0.05	594

Units: K (10^{-11} ph cm^{-2} s^{-1} MeV^{-1}), $E_{\rm cut}$ (GeV), $F_{\rm ph}$ (10^{-7} ph cm^{-2} s^{-1}) and $F_{\rm E}$ (10^{-10} erg cm^{-2} s^{-1}).

Photon fluxes and energy fluxes are calculated with the energy band of $0.1 - 100$ GeV.

and absorbed power-law plus blackbody function (`wabs*(pegpwrlw+bbody)` in xspec)

$$\frac{dN}{dE} = \exp\left[-N_{\rm H} \cdot \sigma\left(E\right)\right] \times \left[\frac{K_{\rm pl}\left(-\Gamma+2\right)E^{-\Gamma}}{E_2^{-\Gamma+2} - E_1^{-\Gamma+2}} + \frac{8.0525 K_{\rm bb} E^2}{\left(kT\right)^4 \left(e^{E/kT}-1\right)}\right].$$

$N_{\rm H}$ and $\sigma\left(E\right)$ are column density of interstellar neutral hydrogen atoms and photoelectric cross-section for X-ray photons with energy E, respectively. The power-law function with a photon index Γ is scaled by a factor $K_{\rm pl}$ with the fixed energy range between E_1 and E_2 ($E_1 < E_2$). The blackbody emission with temperature kT is scaled by a factor $K_{\rm bb} = L_{39}/D_{10}^2$, where L_{39} is a luminosity in the unit of 10^{39} erg s^{-1} and D_{10} is a distance to the object in the unit of 10 kpc.

X-ray spectral parameters are summarized in Table 5.3. Most pulsars can be fitted with the absorbed power-law model and there are no apparent structures such as emission lines and absorption lines in the spectra. The blackbody+power-law model did not converge or was not justified focused on χ^2 values for most of the pulsars, probably because of too weak blackbody emission or poor statistics. A blackbody emission component were required in PSR J0205+6449, PSR J0633+0632, PSR J0633+1746, PSR J1509−5850 and PSR J1833−1034. The blackbody temperature is several tens $\sim$ several hundreds of eV. The photon index is less than 2 for most cases but PSR J1836+5925 and PSR J2238+59 have larger values with large errors ($2.70^{+0.63}_{-0.44}$ and > 2.02, respectively). The column density of neutral hydrogen varies with sources, which reflects that the pulsars are located in various environments in our Galaxy.

Count maps and spectra in gamma-ray and X-ray are shown in Figure 5.11 – 5.33. In the X-ray count maps, source and background regions are shown with solid and broken lines, respectively, and regions with red diagonal lines indicate excluded regions. One may suppose much larger regions than the point spread function are extracted for some sources. It is because we included underlying diffuse emission of pulsar wind nebulae into the spectrum data. However in most cases emission from point sources (i.e. pulsars) are dominant.

To make gamma-ray spectral plots, the photon data were divided into 20 energy bins between 0.2 and 100 GeV and fitting was performed for each divided dataset. Therefore flux points are only representative ones and do not directly link the spectral model function indicated with a black line.

Table 5.3: Fit parameters from X-ray spectral analysis. Errors with 90% confidence level are shown. The power-law and blackbody model (PL+BB) failed in convergence for some pulsars. Rows are left blank in those cases.

			Power-law		Blackbody				
JName	Model	$N_{\rm H}$	$K_{\rm pl}$	Γ	$K_{\rm bb}$	kT	$F_{\rm ph}$	$F_{\rm E}$	χ^2_ν (dof)
J0007+7303	PL	$0.10^{+0.09}_{-0.08}$	$0.251^{+0.030}_{-0.028}$	$1.51^{+0.25}_{-0.23}$			$5.70^{+0.48}_{-0.55}\times10^{-5}$	$2.34^{+0.33}_{-0.35}\times10^{-13}$	1.192 (52))
	PL+BB								...
J0205+6449	PL	0.44 ± 0.03	$8.66^{+0.23}_{-0.22}$	2.00 ± 0.05			$1.43^{+0.03}_{-0.02}\times10^{-3}$	$5.99^{+0.14}_{-0.15}\times10^{-12}$	1.009 (505)
	PL+BB	0.39 ± 0.06	$7.66^{+0.99}_{-0.96}$	$1.85^{+0.16}_{-0.18}$	$7.08^{+6.51}_{-6.54}\times10^{-6}$	$0.390^{+0.121}_{-0.089}$	$1.44^{+0.14}_{-0.06}\times10^{-3}$	$6.06^{+0.43}_{-0.23}\times10^{-12}$	1.007 (503)
J0357+32	PL	$0.25^{+0.31}_{-0.22}$	$0.190^{+0.051}_{-0.034}$	$1.87^{+0.53}_{-0.43}$			$3.92^{+0.80}_{-0.76}\times10^{-5}$	$1.51^{+0.29}_{-0.34}\times10^{-13}$	1.170 (19)
	PL+BB								...
J0633+0632	PL	$0.15^{+0.06}_{-0.05}$	1.80 ± 0.08	$1.59^{+0.10}_{-0.09}$			$3.95^{+0.21}_{-0.18}\times10^{-4}$	$(1.62\pm0.08)\times10^{-12}$	1.223 (66)
	PL+BB	$0.45^{+0.36}_{-0.29}$	$1.95^{+0.28}_{-0.78}$	$1.73^{+0.22}_{-0.16}$	$<2.4\times10^{-4}$	$0.120^{+0.055}_{-0.016}$	$3.85^{+0.60}_{-0.49}\times10^{-4}$	$1.59^{+0.12}_{-0.10}\times10^{-12}$	1.217 (64)
J0633+1746	PL	$<8\times10^{-4}$	0.397 ± 0.008	2.03 ± 0.03			$1.60^{+0.01}_{-0.11}\times10^{-4}$	$3.77^{+0.24}_{-0.01}\times10^{-13}$	1.563 (689)
	PL+BB	$0.039^{+0.021}_{-0.013}$	$0.418^{+0.006}_{-0.004}$	$1.93^{+0.04}_{-0.03}$	$3.10^{+0.52}_{-0.64}\times10^{-5}$	$0.055^{+0.003}_{-0.001}$	$1.78^{+0.42}_{-0.32}\times10^{-4}$	$4.31^{+0.37}_{-0.31}\times10^{-13}$	0.993 (687)
J1022−5746	PL	$1.16^{+0.44}_{-0.36}$	$0.192^{+0.025}_{-0.019}$	$1.39^{+0.36}_{-0.32}$			$2.14^{+0.17}_{-0.23}\times10^{-5}$	$1.42^{+0.18}_{-0.21}\times10^{-13}$	1.228 (28)
	PL+BB								...
J1028−5819	PL	$0.23^{+0.15}_{-0.12}$	$0.836^{+0.080}_{-0.070}$	$1.74^{+0.22}_{-0.20}$			$1.71^{+0.19}_{-0.17}\times10^{-4}$	$6.95^{+0.66}_{-0.70}\times10^{-13}$	1.080 (50)
	PL+BB								...
J1048−5832	PL	$0.58^{+0.69}_{-0.39}$	$0.165^{+0.080}_{-0.038}$	$1.65^{+0.85}_{-0.64}$			$2.35^{+0.45}_{-0.68}\times10^{-5}$	$1.24^{+0.38}_{-0.48}\times10^{-13}$	0.757 (15)
	PL+BB								...
J1413−6205	PL	<0.378	$0.241^{+0.029}_{-0.028}$	$1.39^{+0.28}_{-0.26}$			$4.72^{+0.60}_{-0.57}\times10^{-5}$	$2.20^{+0.27}_{-0.30}\times10^{-13}$	1.013 (45)
	PL+BB								...
J1418−6058	PL	$2.14^{+0.33}_{-0.29}$	2.94 ± 0.14	$1.51^{+0.17}_{-0.16}$			$3.69^{+0.14}_{-0.17}\times10^{-4}$	$2.64^{+0.14}_{-0.16}\times10^{-12}$	0.782 (84)
	PL+BB	$3.09^{+1.02}_{-0.85}$	$4.97^{+1.42}_{-0.78}$	$1.77^{+0.31}_{-0.26}$	$0.27^{+2.55}_{-0.25}\times10^{-4}$	$0.139^{+0.05}_{-0.45}$	$3.63^{+0.23}_{-0.21}\times10^{-4}$	$2.55^{+0.12}_{-0.23}\times10^{-12}$	0.749 (82)

Table 5.3: Continued.

			Power-law		Blackbody				
JName	Model	$N_{\rm H}$	$K_{\rm pl}$	Γ	$K_{\rm bb}$	kT	$F_{\rm ph}$	$F_{\rm E}$	χ^2_ν (dof)
J1459−60	PL	< 0.29	$0.142^{+0.024}_{-0.023}$	$1.54^{+0.39}_{-0.30}$			$3.41^{+0.43}_{-0.66} \times 10^{-5}$	$1.33^{+0.19}_{-0.29} \times 10^{-13}$	1.139 (18)
	PL+BB								...
J1509−5850	PL	$1.36^{+0.29}_{-0.25}$	$0.568^{+0.073}_{-0.053}$	$1.79^{+0.22}_{-0.20}$			$5.70^{+0.30}_{-0.39} \times 10^{-5}$	$3.44^{+0.27}_{-0.32} \times 10^{-13}$	1.630 (106)
	PL+BB	$1.45^{+0.36}_{-0.23}$	$0.583^{+0.100}_{-0.052}$	$1.83^{+0.26}_{-0.17}$	< 2.74	$0.052^{+0.038}_{-0.019}$	$5.79^{+2.22}_{-0.10} \times 10^{-5}$	$3.43^{+0.41}_{-0.28} \times 10^{-13}$	1.626 (104)
J1826−1256	PL	$3.24^{+2.00}_{-1.36}$	$0.693^{+0.770}_{-0.180}$	$1.76^{+0.85}_{-0.70}$			$4.80^{+0.47}_{-1.77} \times 10^{-5}$	$3.51^{+0.47}_{-1.40} \times 10^{-13}$	0.933 (16)
	PL+BB								...
J1833−1034	PL	2.30 ± 0.03	$71.9^{+0.9}_{-0.8}$	1.81 ± 0.02			$5.70^{+0.03}_{-0.02} \times 10^{-3}$	$3.83^{+0.03}_{-0.02} \times 10^{-11}$	1.196 (2225)
	PL+BB	2.39 ± 0.05	73.9 ± 1.2	1.84 ± 0.02	$1.40^{+5.55}_{-1.06} \times 10^{-2}$	$0.080^{+0.017}_{-0.013}$	$5.70^{+0.09}_{-0.02} \times 10^{-3}$	$3.82^{+0.03}_{-0.01} \times 10^{-11}$	1.178 (2223)
J1836+5925	PL	< 0.08	$0.0207^{+0.0057}_{-0.0046}$	$2.70^{+0.63}_{-0.44}$			$1.21^{+0.01}_{-0.90} \times 10^{-5}$	$2.07^{+0.12}_{-1.49} \times 10^{-14}$	1.101 (6)
	PL+BB	< 0.58	$0.026^{+0.076}_{-0.009}$	$2.46^{+1.64}_{-0.85}$	$0.32^{+5.61}_{-0.30} \times 10^{-5}$	$0.067^{+0.043}_{-0.057}$	$1.33^{+1.92}_{-0.42} \times 10^{-5}$	$2.45^{+3.26}_{-0.97} \times 10^{-14}$	0.724 (4)
J1907+06	PL	< 2.35	$0.148^{+0.152}_{-0.042}$	$1.36^{+1.09}_{-0.80}$			$1.96^{+0.45}_{-0.65} \times 10^{-5}$	$1.19^{+0.32}_{-0.48} \times 10^{-13}$	1.824 (9)
	PL+BB								...
J1952+3252	PL	0.30 ± 0.03	12.7 ± 0.04	1.86 ± 0.07			$(2.45 \pm 0.06) \times 10^{-3}$	$(9.91 \pm 0.36) \times 10^{-12}$	0.825 (253)
	PL+BB								...
J1954+2836	PL	$1.42^{+2.00}_{-1.17}$	$0.231^{+0.765}_{-0.097}$	$2.08^{+1.31}_{-1.01}$			$< 2.4 \times 10^{-5}$	$1.17^{+0.21}_{-0.66} \times 10^{-13}$	0.386 (5)
	PL+BB								...
J1958+2846	PL	< 0.33	$0.0877^{+0.0191}_{-0.0174}$	$1.42^{+0.57}_{-0.26}$			$2.31^{+0.04}_{-1.11} \times 10^{-5}$	$8.77^{+1.06}_{-3.39} \times 10^{-14}$	0.594 (9)
	PL+BB								...
J2021+3651	PL	0.45 ± 0.05	1.29 ± 0.04	1.50 ± 0.08			$1.96^{+0.05}_{-0.06} \times 10^{-4}$	$1.05^{+0.04}_{-0.05} \times 10^{-12}$	0.929 (249)
	PL+BB								...

Table 5.3: Continued.

			Power-law		Blackbody				
JName	Model	$N_{\rm H}$	$K_{\rm pl}$	Γ	$K_{\rm bb}$	kT	$F_{\rm ph}$	$F_{\rm E}$	χ^2_ν (dof)
J2032+4127	PL	< 1.01	$0.0384^{+0.0217}_{-0.0085}$	$1.93^{+1.29}_{-0.85}$			$5.06^{+1.19}_{-1.98} \times 10^{-6}$	$2.09^{+0.66}_{-0.99} \times 10^{-14}$	1.979 (2)
	PL+BB								...
J2229+6114	PL	$0.52^{+0.06}_{-0.05}$	1.60 ± 0.05	1.44 ± 0.07			$(2.31 \pm 0.06) \times 10^{-4}$	$(1.30 \pm 0.05) \times 10^{-12}$	1.181 (135)
	PL+BB								...
J2238+59	PL	< 3.31	< 26.5	> 2.02			$1.20^{+0.25}_{-1.13} \times 10^{-5}$	$3.13^{+0.71}_{-2.97} \times 10^{-14}$	0.655 (7)
	PL+BB								...

Units: $N_{\rm H}$ (10^{22} cm^{-2}), $K_{\rm pl}$ (10^{-12} erg cm^{-2} s^{-1}, for the energy range $0.5-10$ keV), $K_{\rm bb}$ (10^{37} erg s^{-1} kpc^{-2}), kT (keV), $F_{\rm ph}$ (photon cm^{-2} s^{-1}) and $F_{\rm E}$ (erg cm^{-2} s^{-1}).

Photon fluxes and energy fluxes are absorbed values calculated with the energy band of $0.5-10$ keV. The scale factor of power-law component $K_{\rm pl}$ represents non-absorbed energy flux between $0.5-10$ keV.

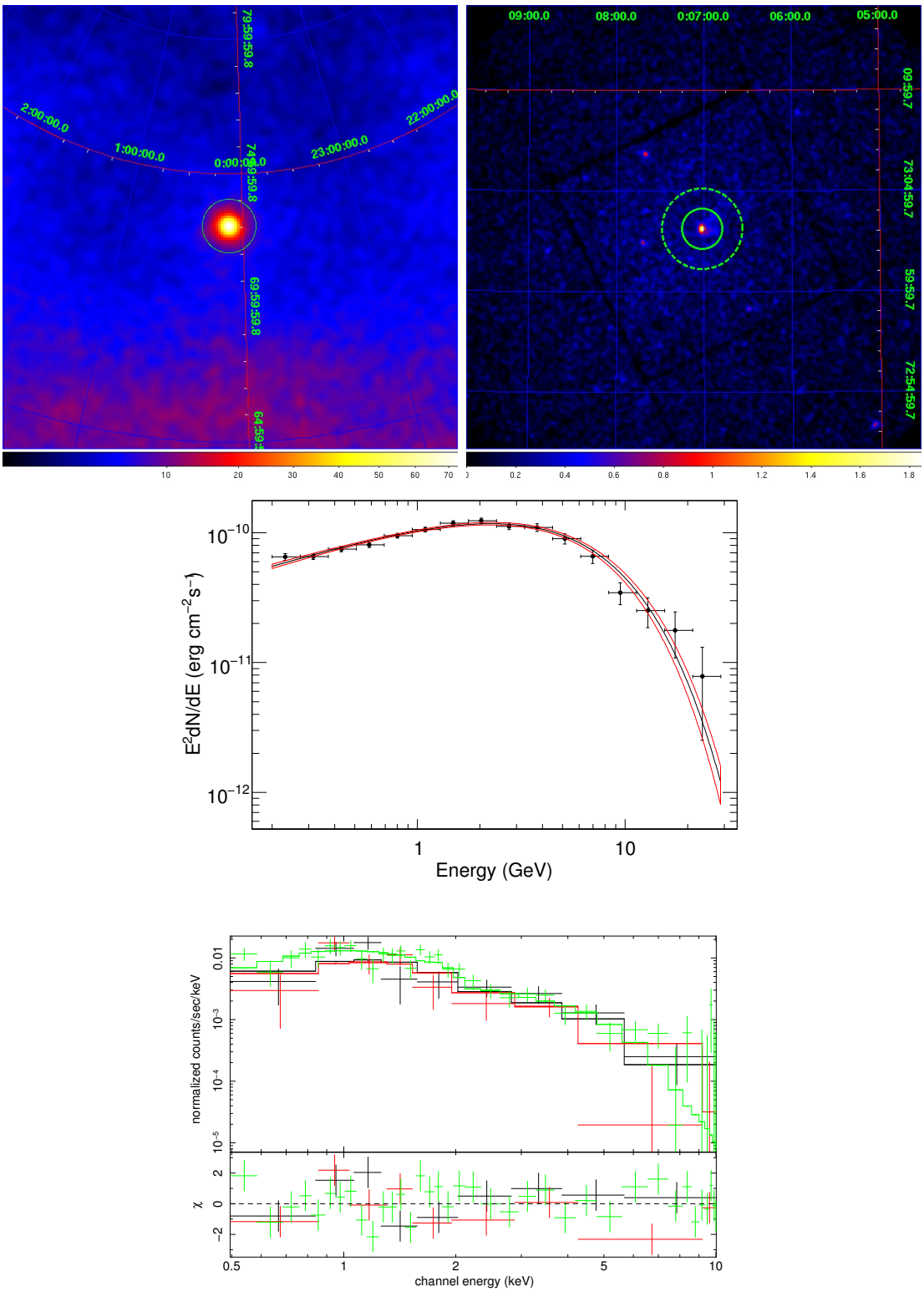

Figure 5.11: Count maps and spectra of PSR J0007+7303. (Top left) 0.2 – 100 GeV Gamma-ray count map. The center of the circle indicates the pulsar position. (Top left) 0.5 – 10 keV X-ray count map. Extracted source and background regions are shown by a solid line and a broken line, respectively. (Middle) Gamma-ray deconvolved spectrum. Red lines show the error range of the best fit model function. (Bottom) X-ray spectra convolved with instrumental response.

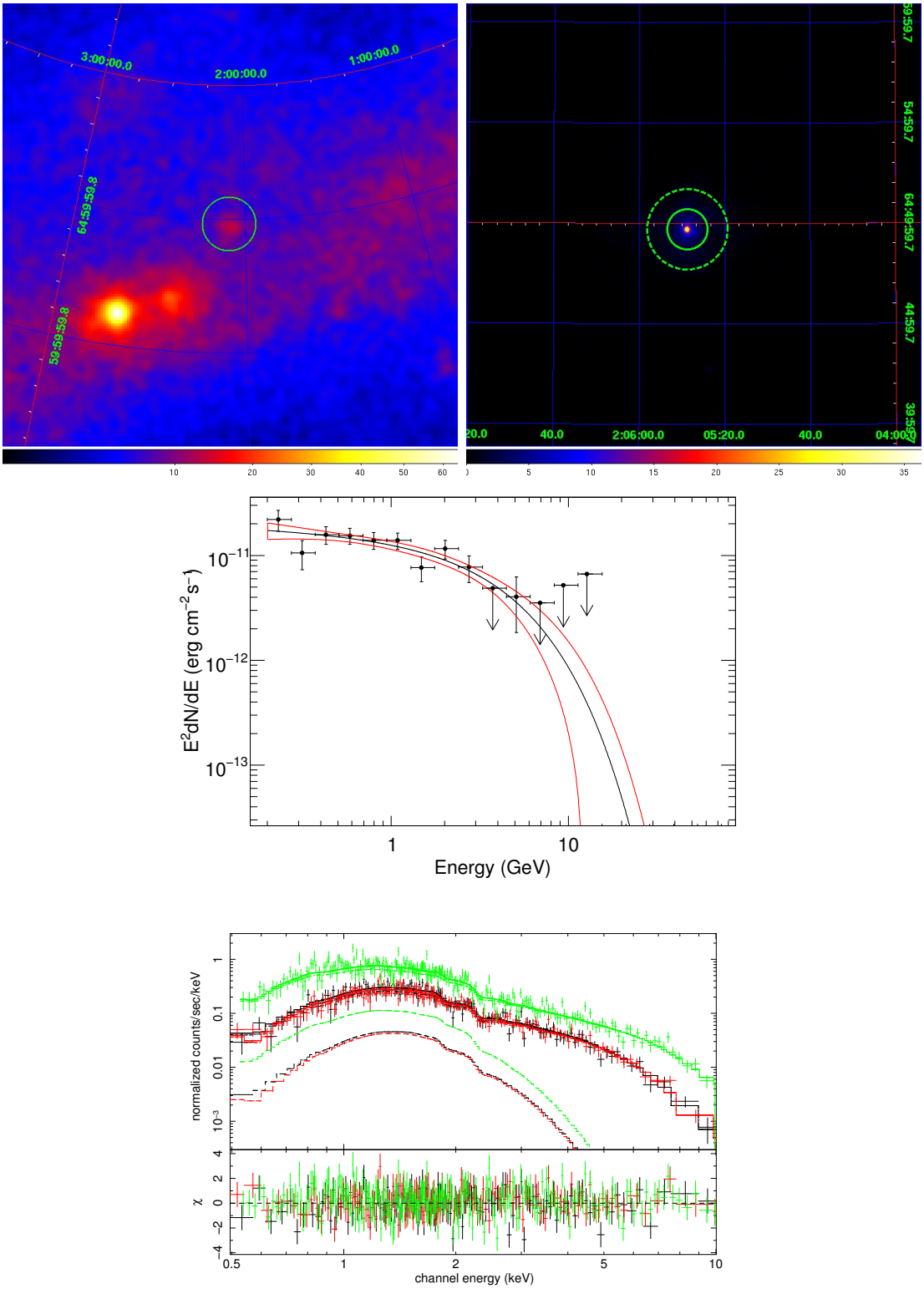

Figure 5.12: Same as Figure 5.11 but for PSR J0205+6449.

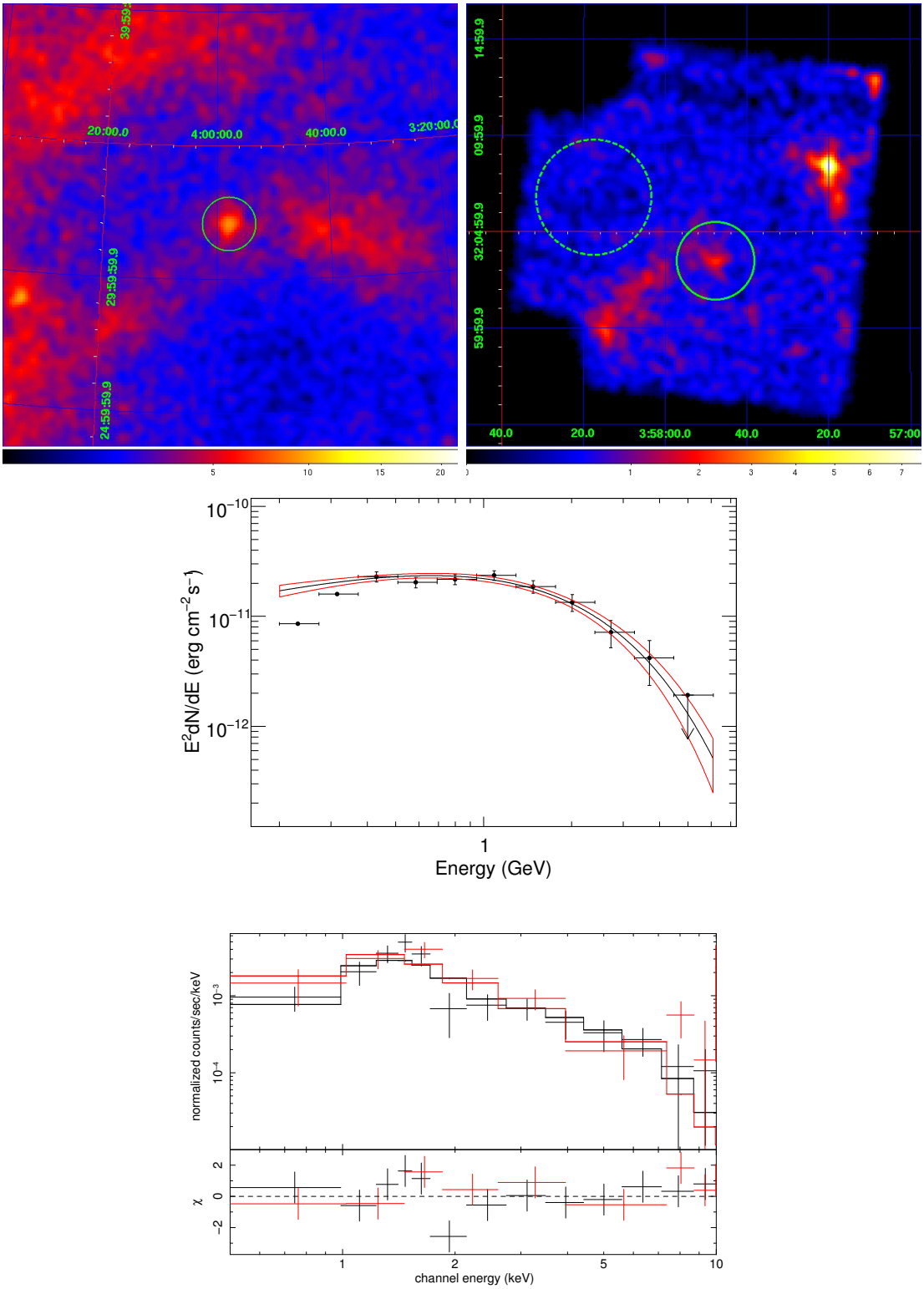

Figure 5.13: Same as Figure 5.11 but for PSR J0357+32.

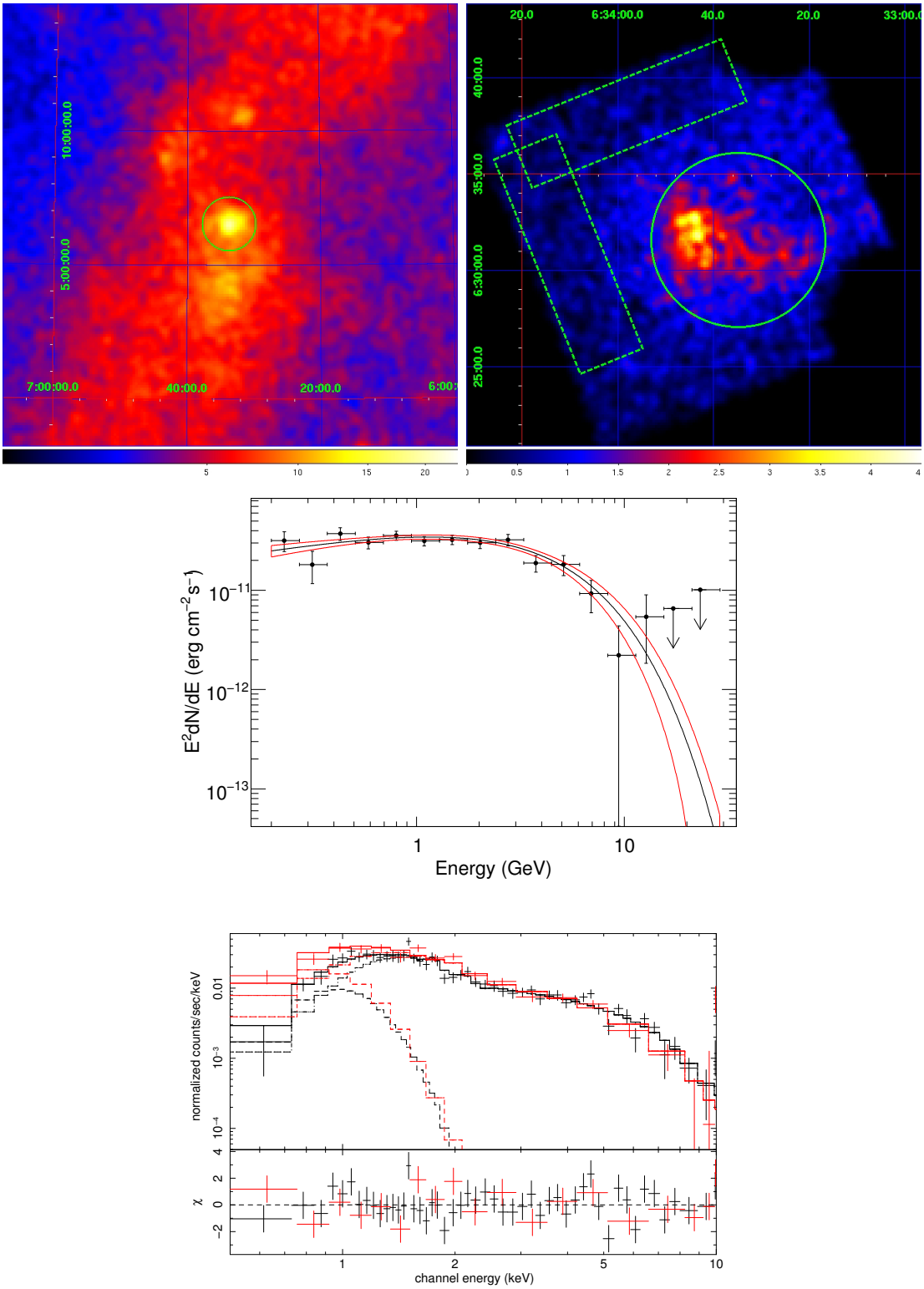

Figure 5.14: Same as Figure 5.11 but for PSR J0633+0632.

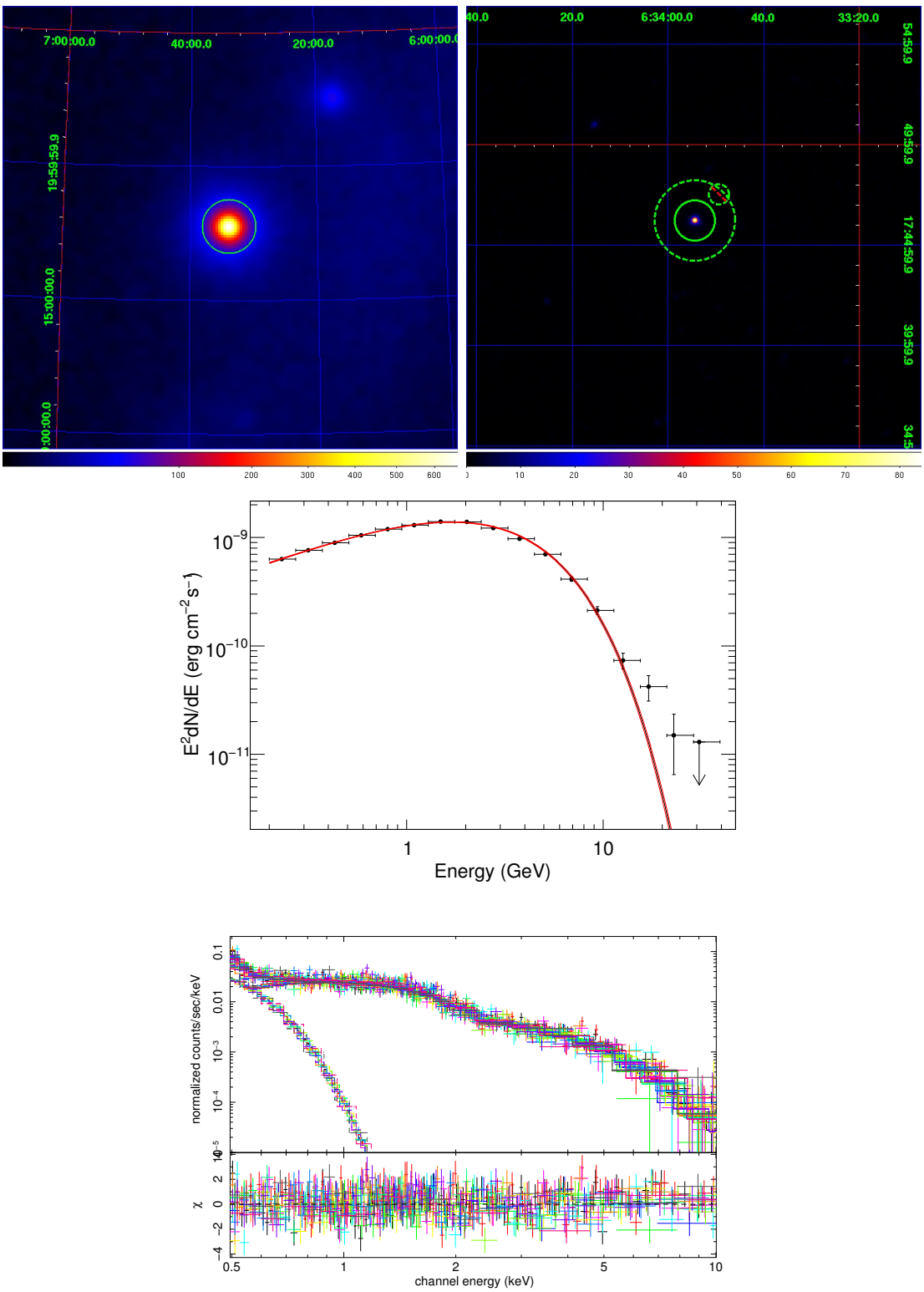

Figure 5.15: Same as Figure 5.11 but for PSR J0633+1746.

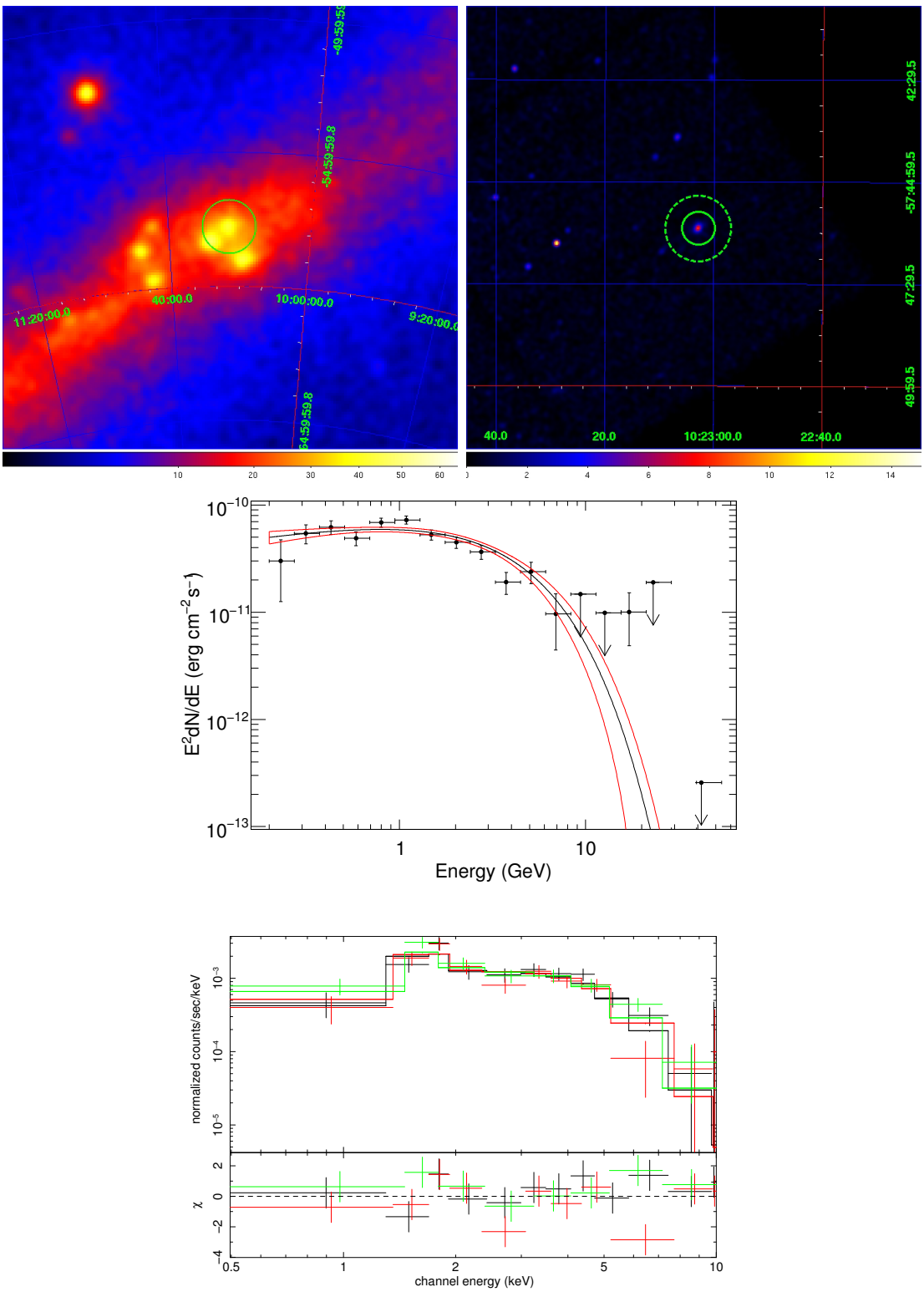

Figure 5.16: Same as Figure 5.11 but for PSR J1022–5746.

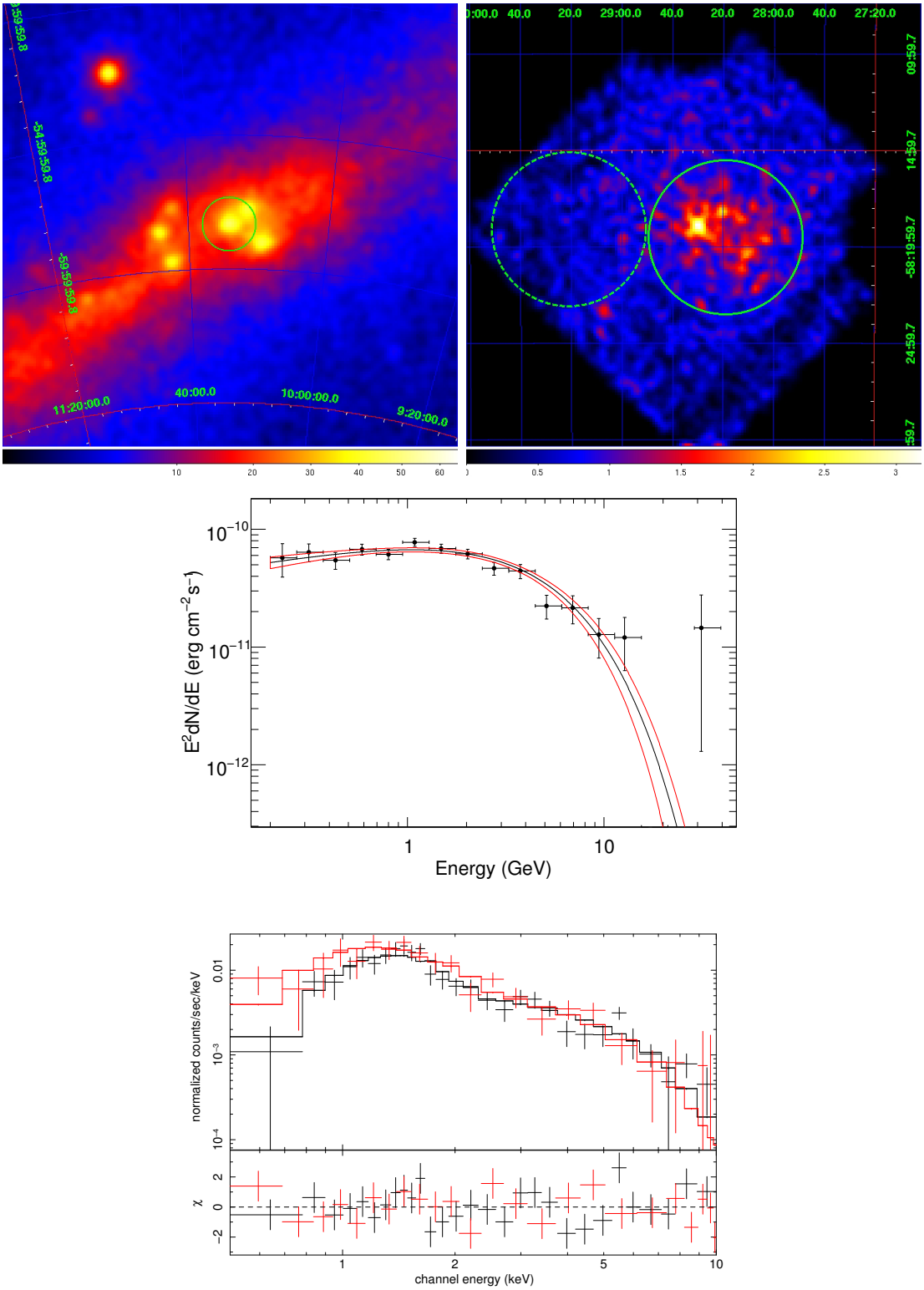

Figure 5.17: Same as Figure 5.11 but for PSR J1028–5819.

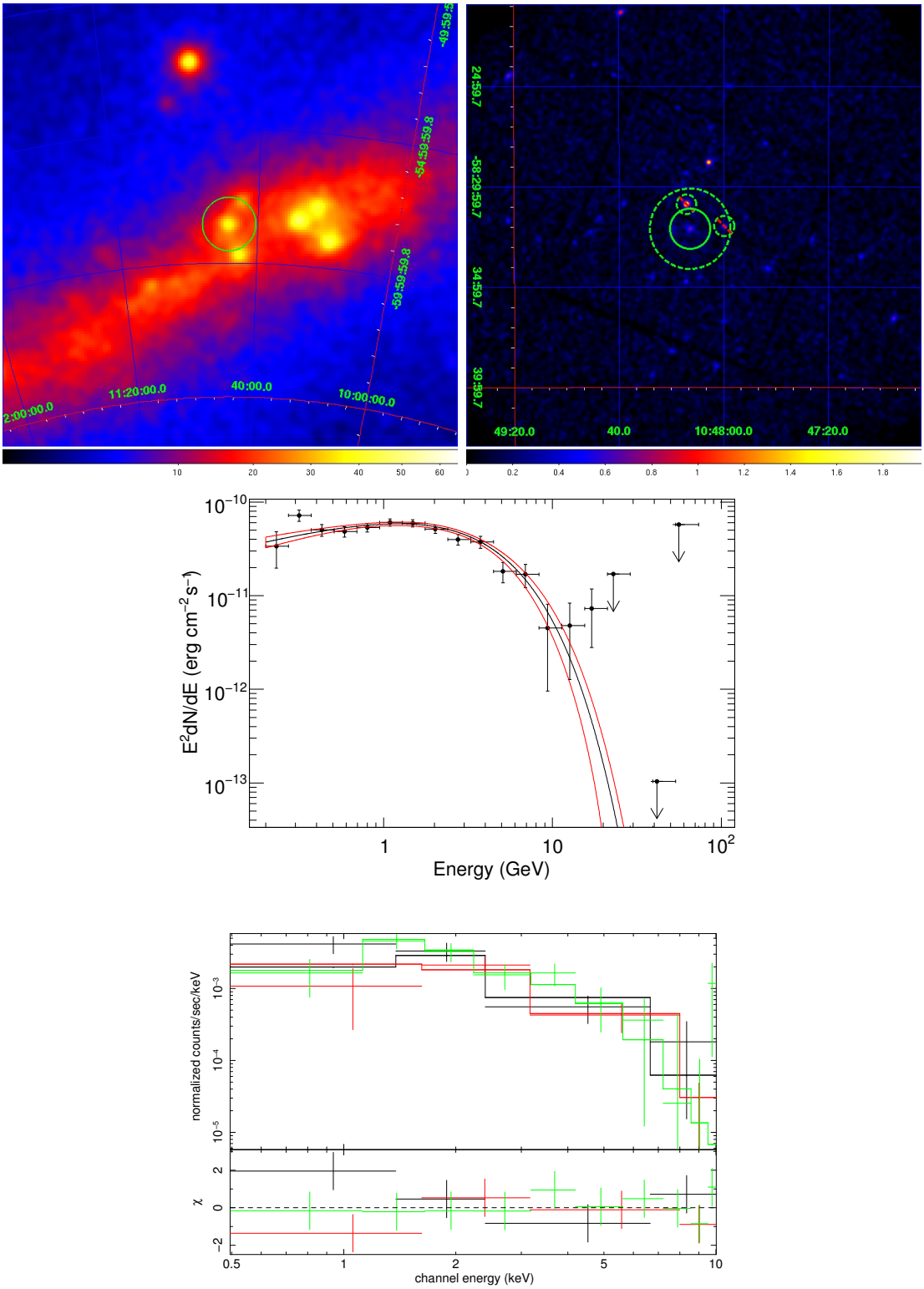

Figure 5.18: Same as Figure 5.11 but for PSR J1048–5832.

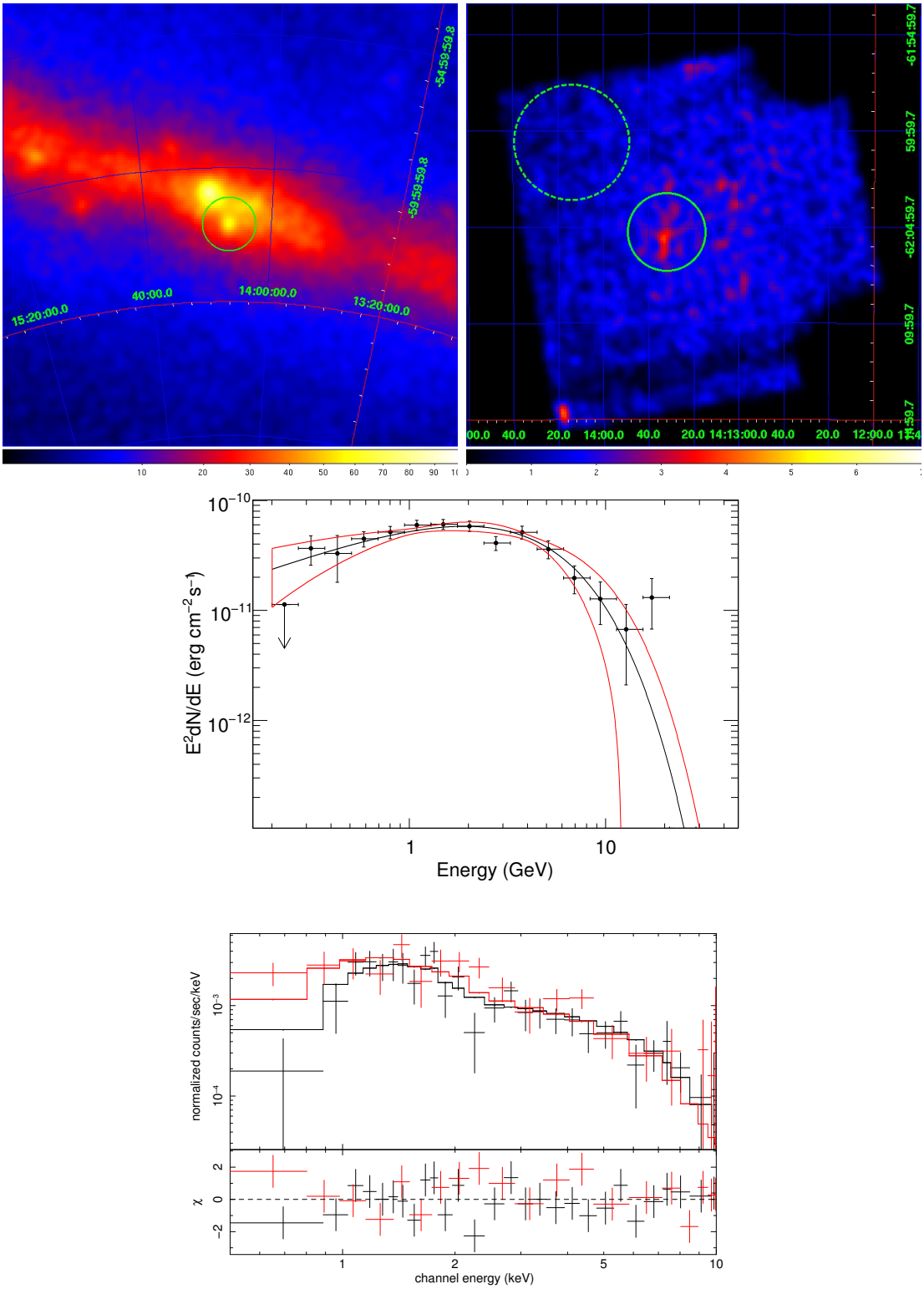

Figure 5.19: Same as Figure 5.11 but for PSR J1413–6205.

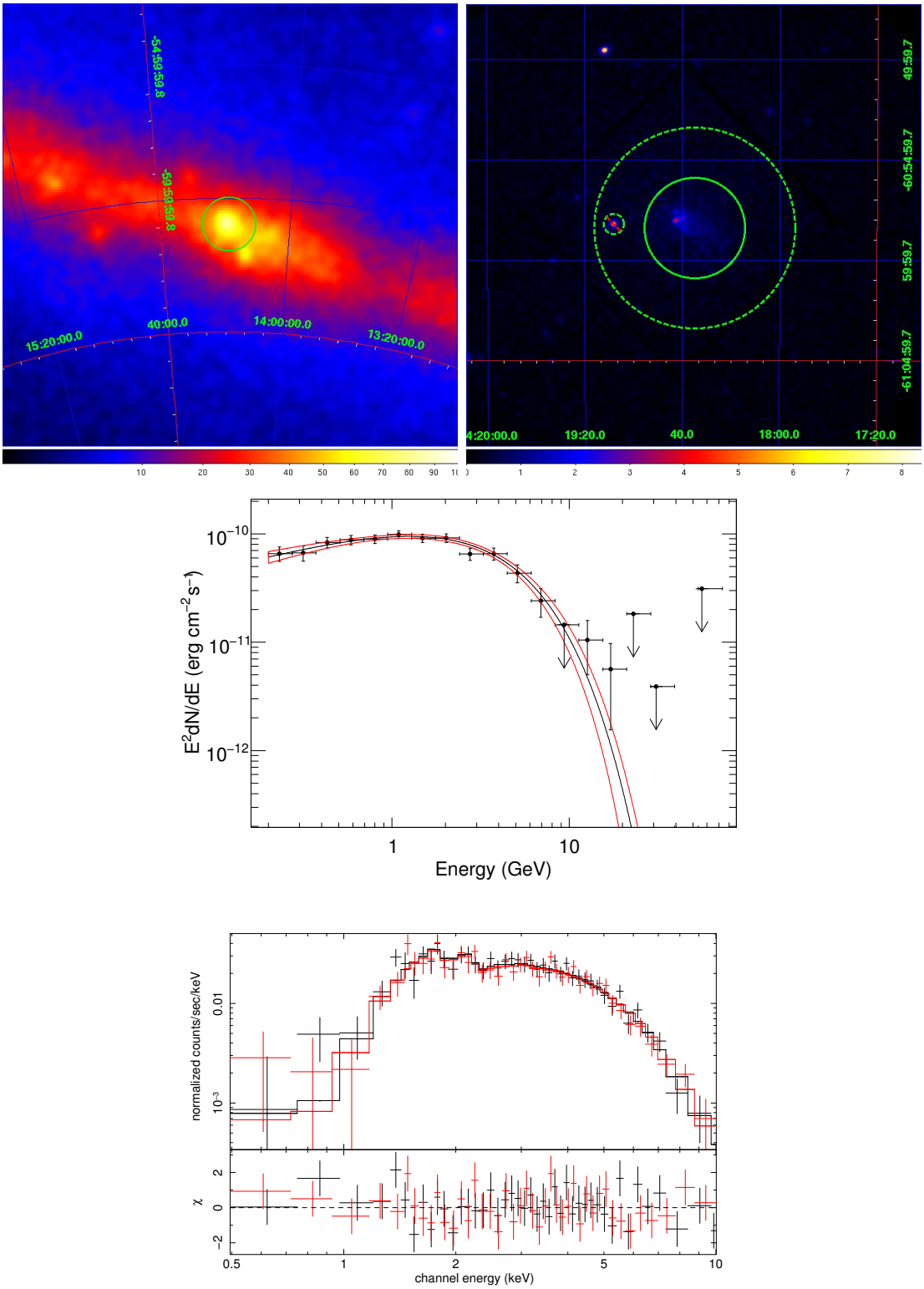

Figure 5.20: Same as Figure 5.11 but for PSR J1418–6058.

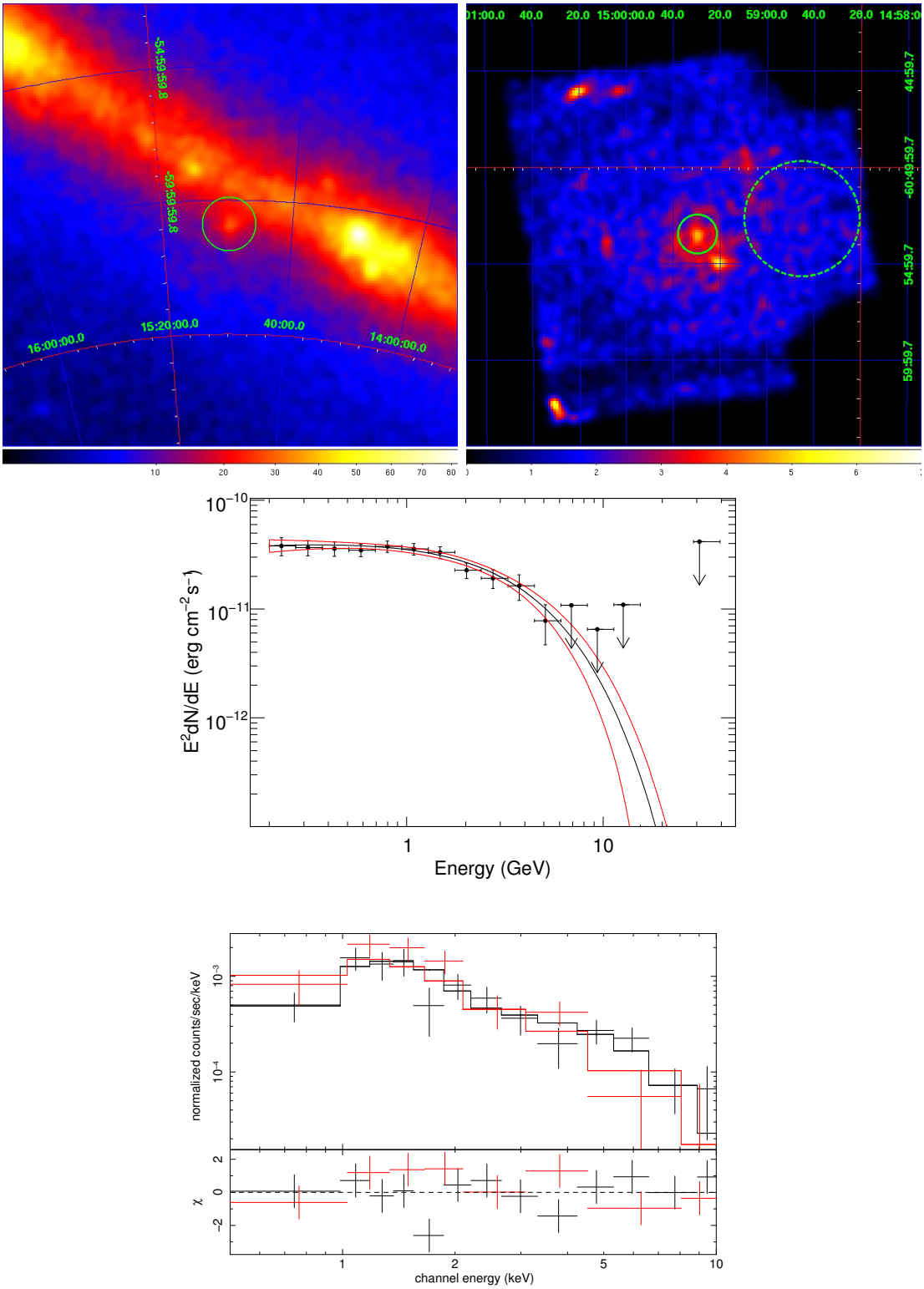

Figure 5.21: Same as Figure 5.11 but for PSR J1459–60.

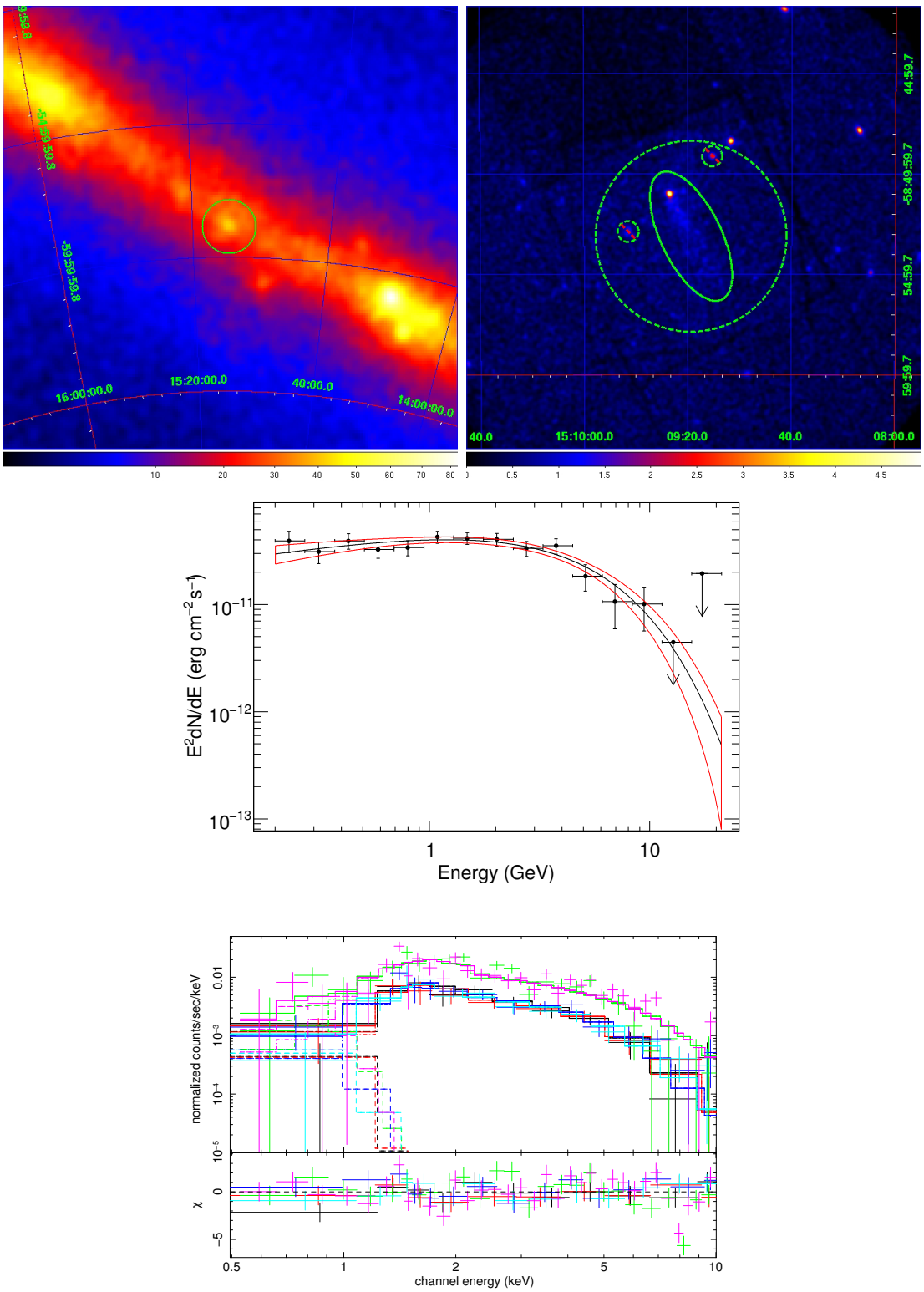

Figure 5.22: Same as Figure 5.11 but for PSR J1509–5850.

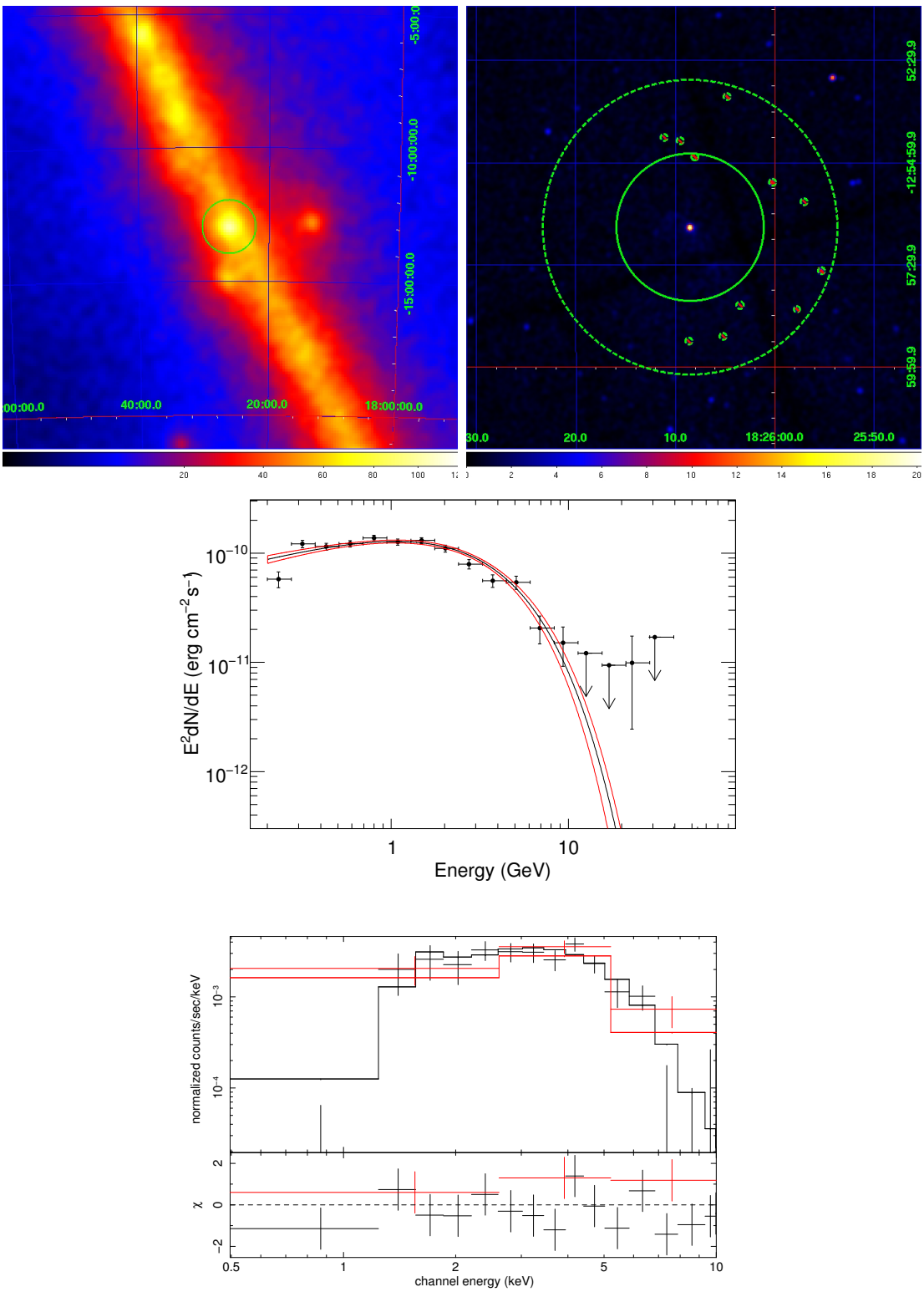

Figure 5.23: Same as Figure 5.11 but for PSR J1826–1256.

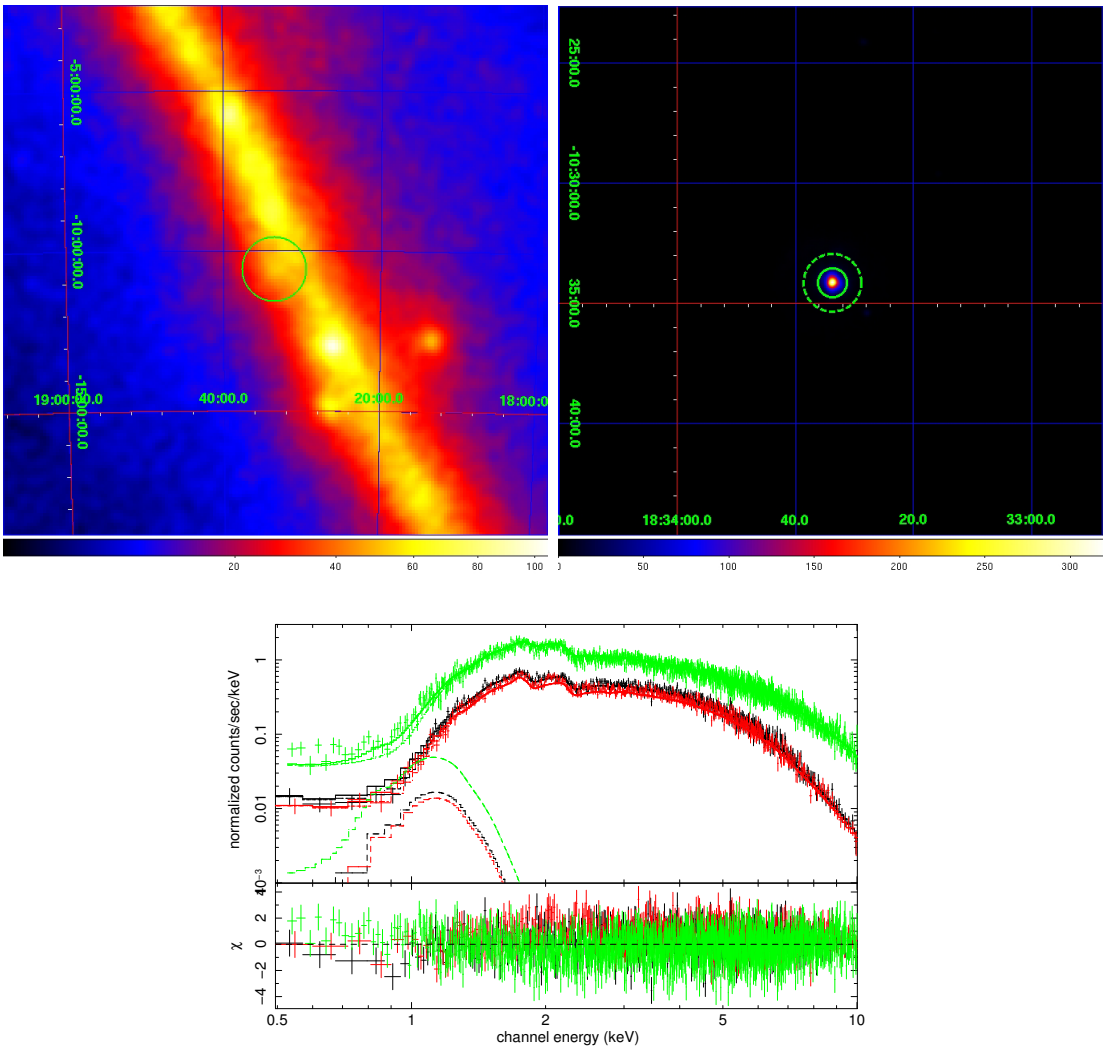

Figure 5.24: Same as Figure 5.11 but for PSR J1833–1034.

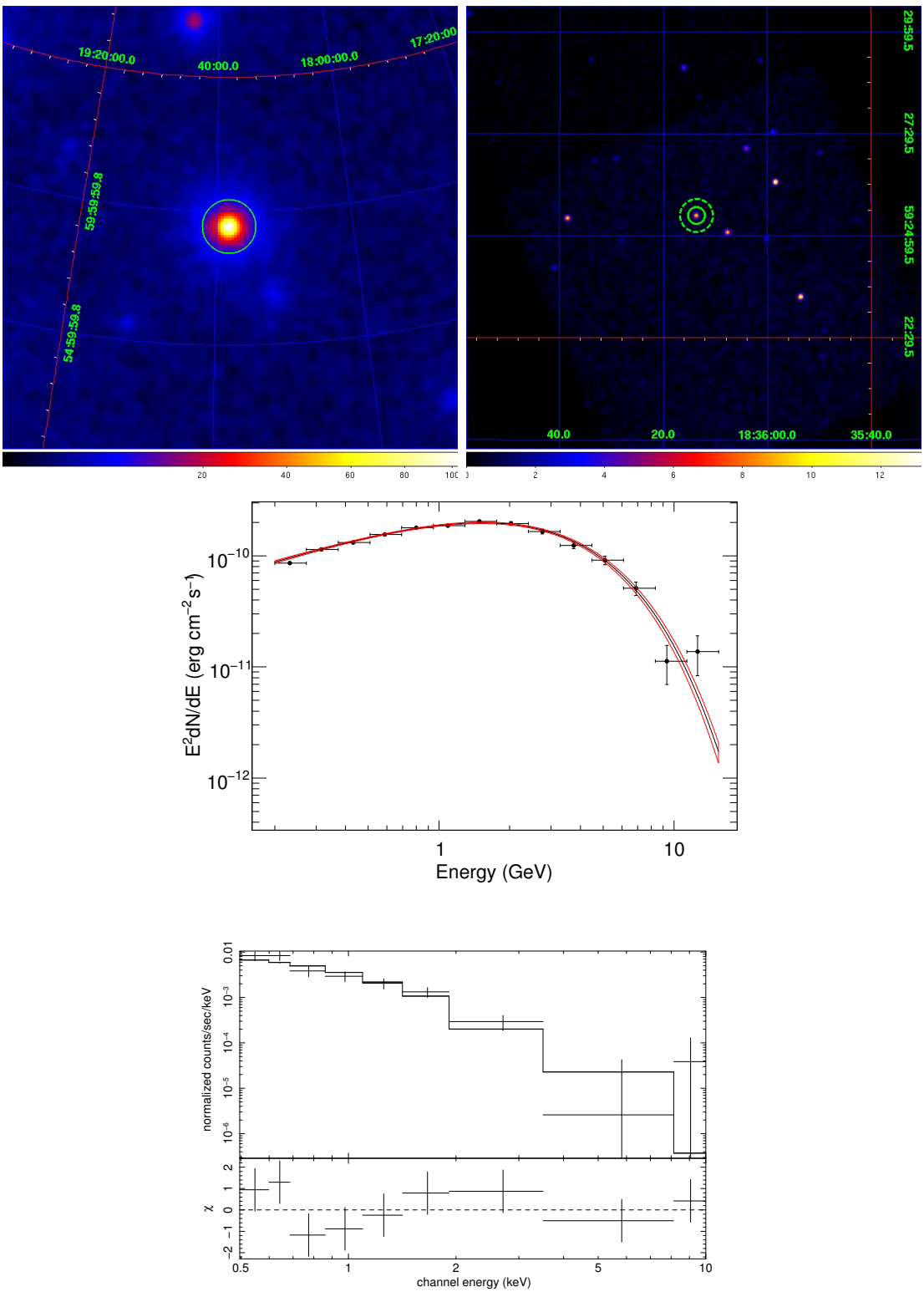

Figure 5.25: Same as Figure 5.11 but for PSR J1836+5925.

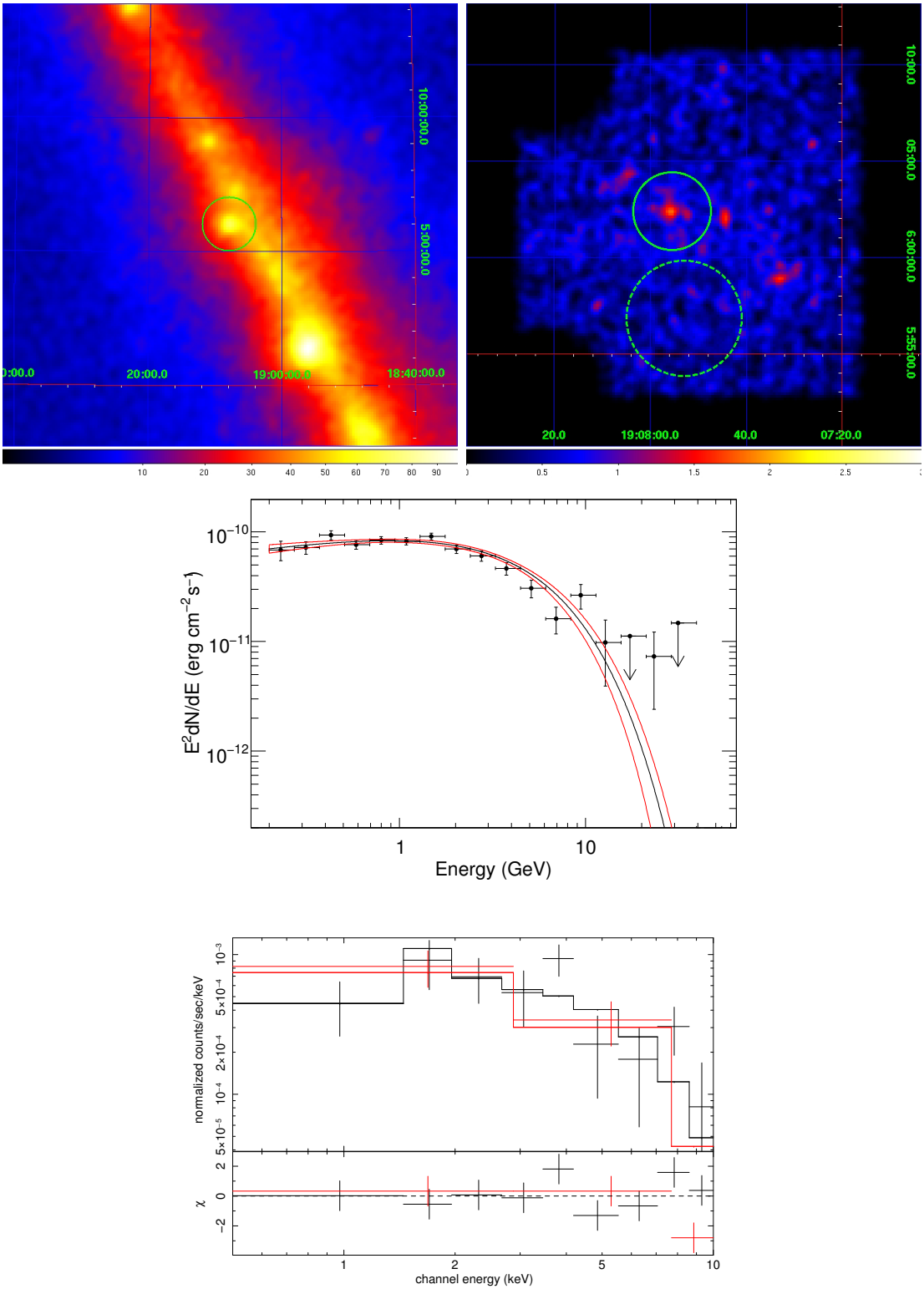

Figure 5.26: Same as Figure 5.11 but for PSR J1907+06.

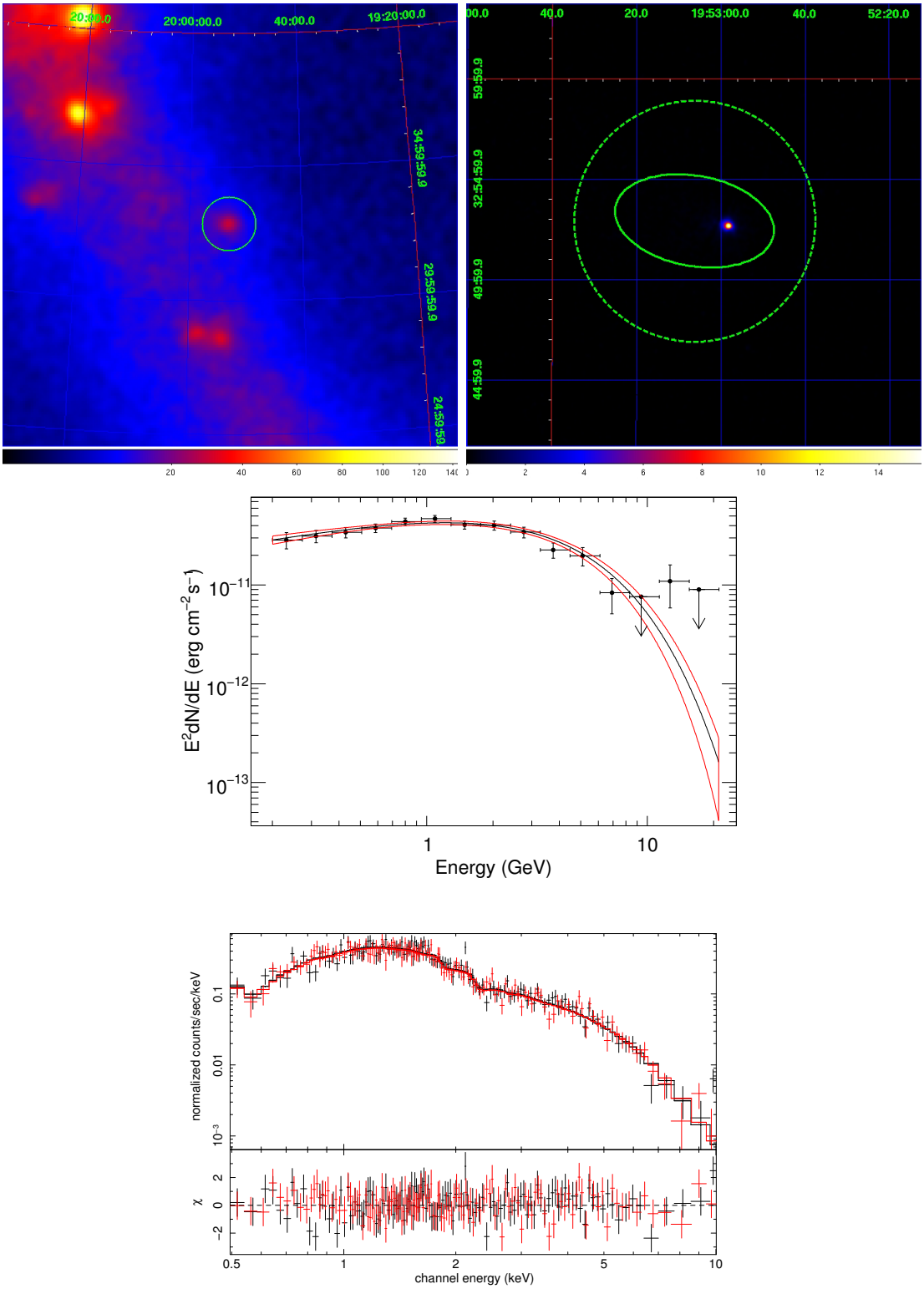

Figure 5.27: Same as Figure 5.11 but for PSR J1952+3252.

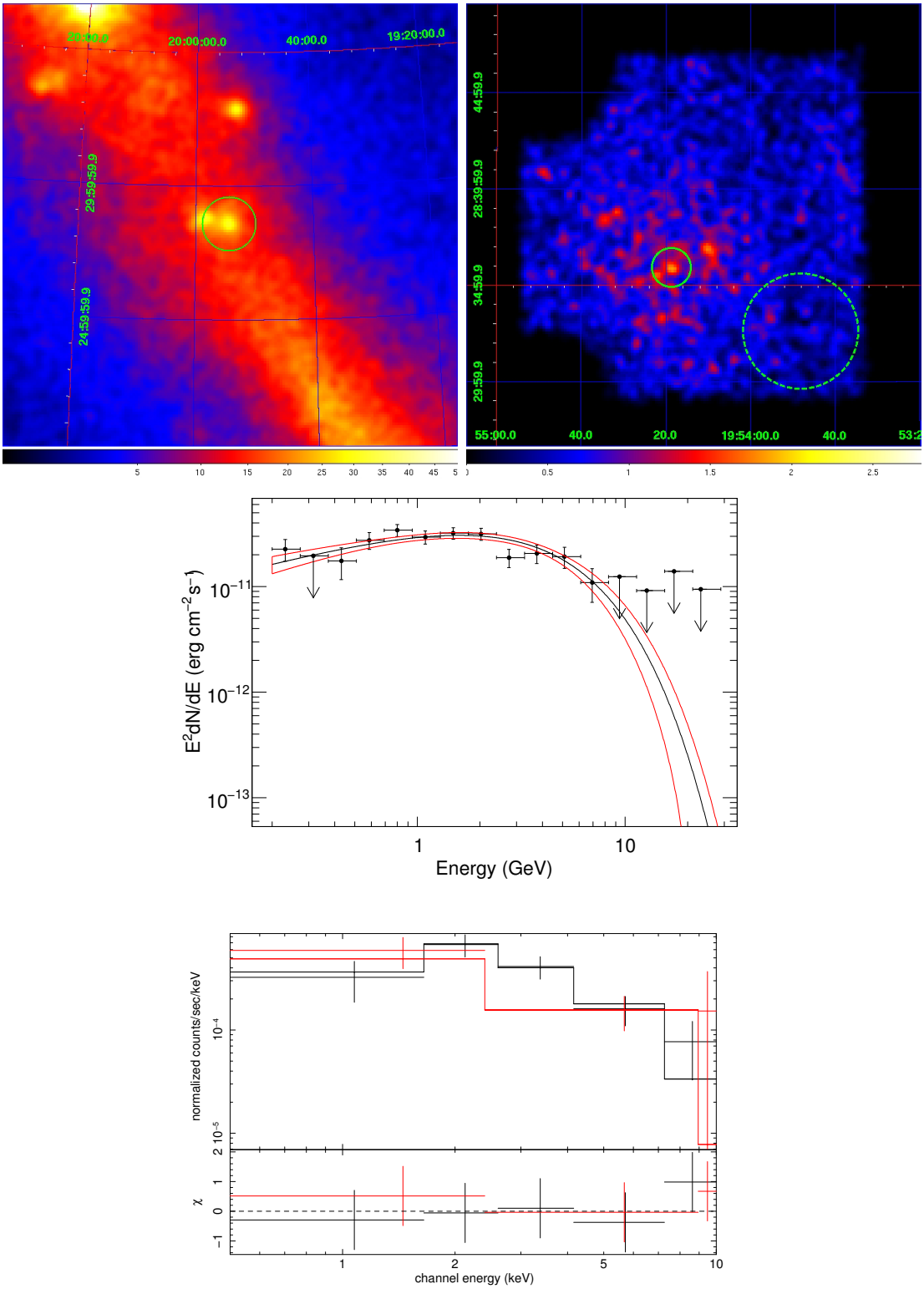

Figure 5.28: Same as Figure 5.11 but for PSR J1954+2836.

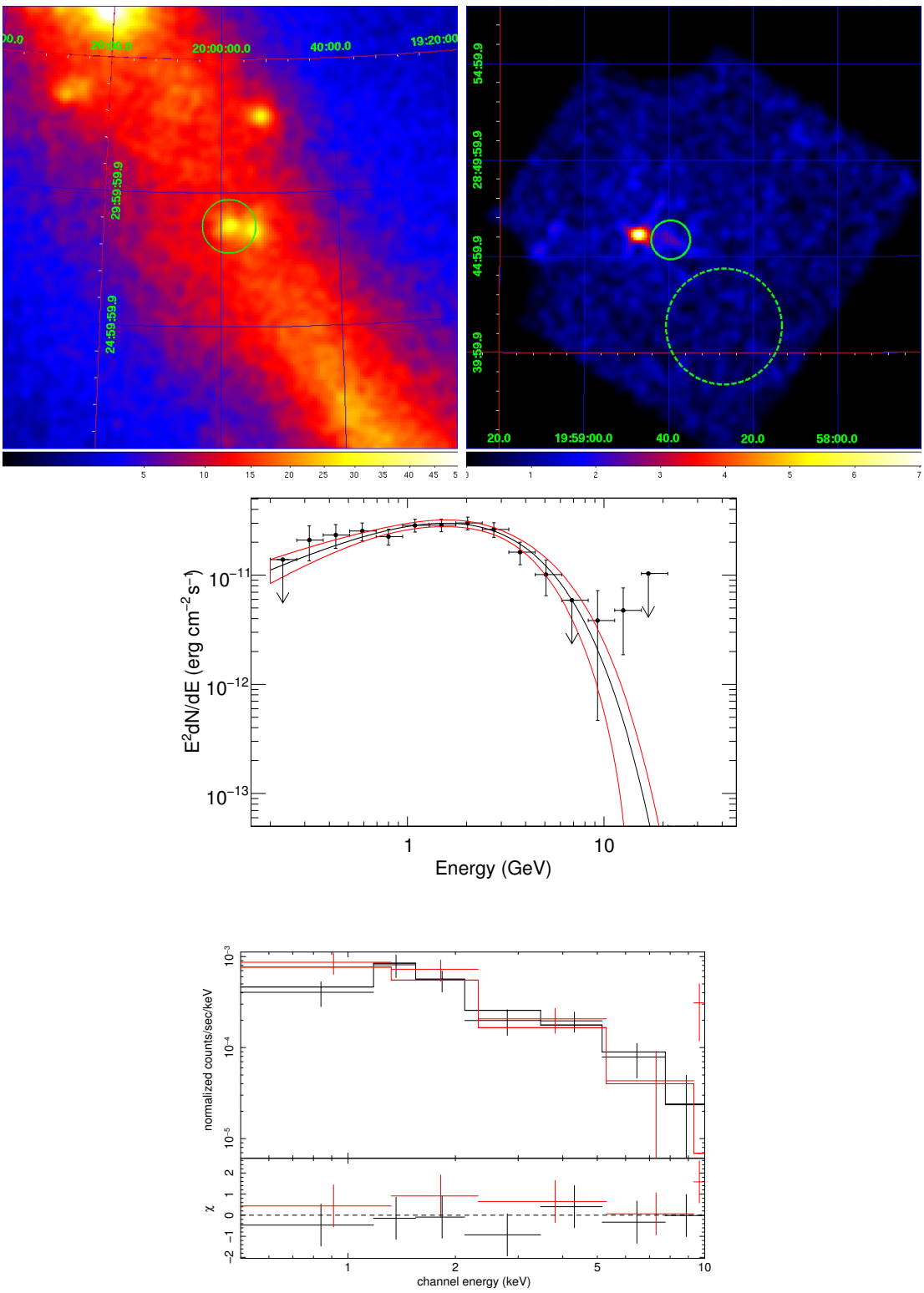

Figure 5.29: Same as Figure 5.11 but for PSR J1958+2846.

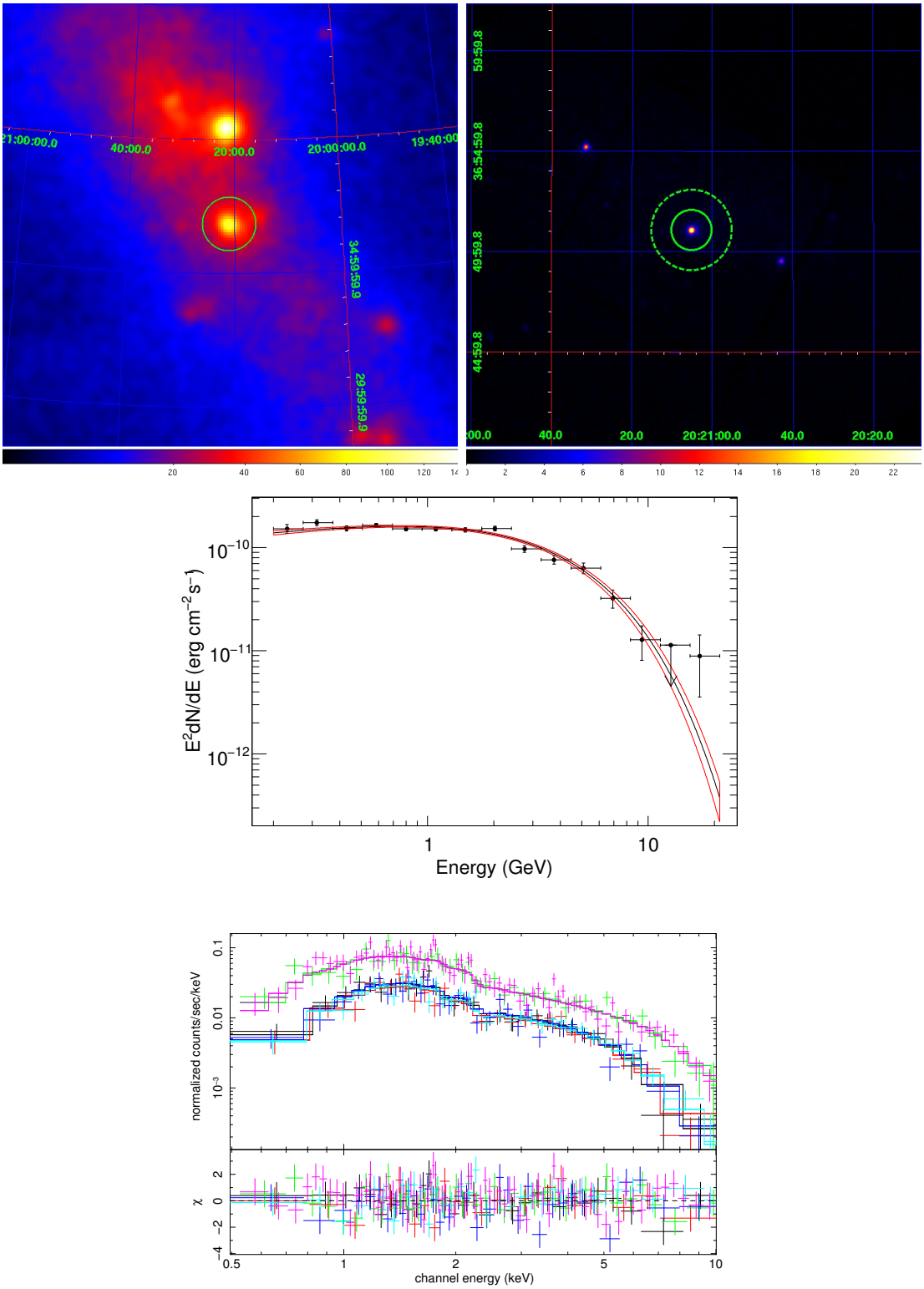

Figure 5.30: Same as Figure 5.11 but for PSR J2021+3651.

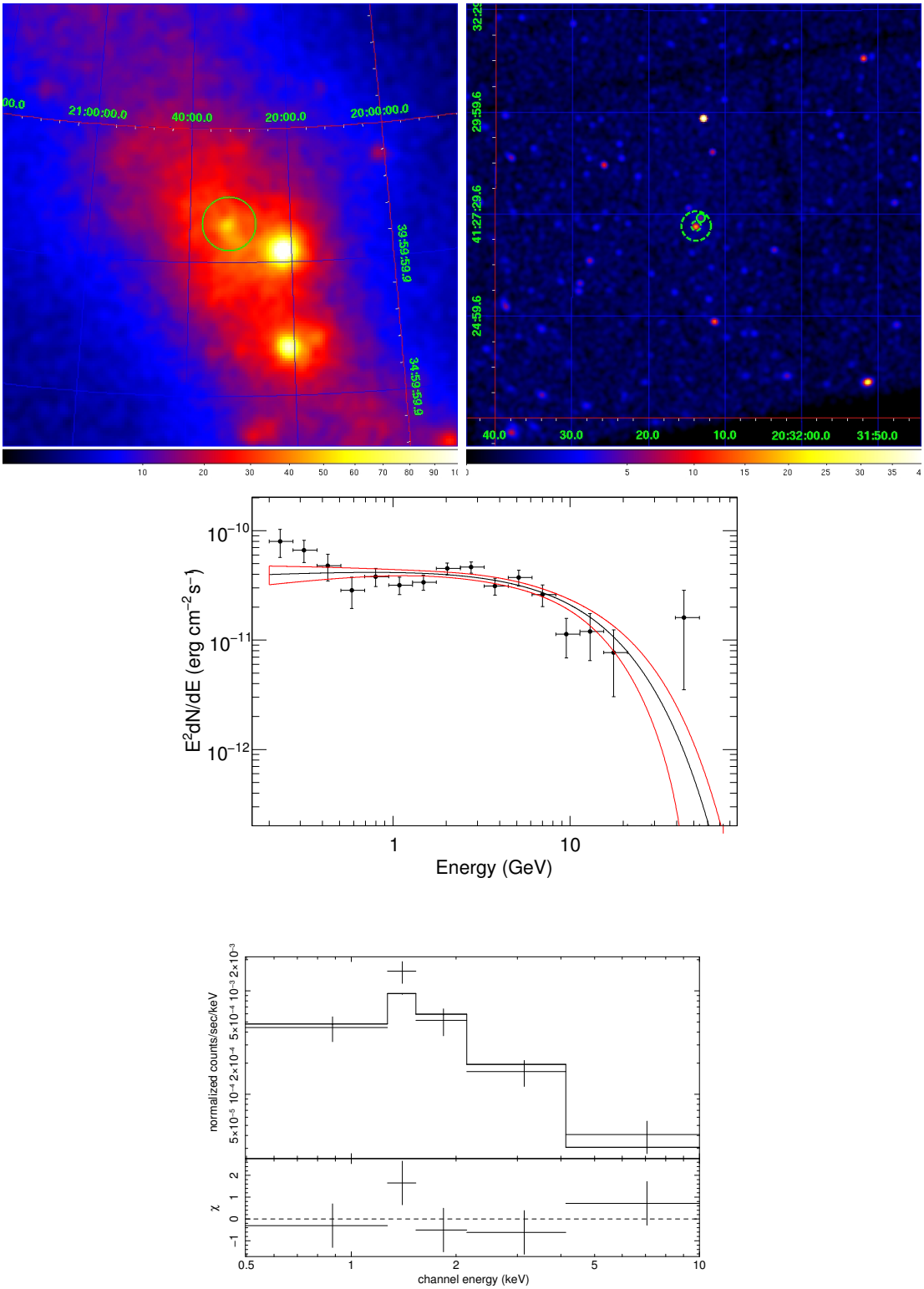

Figure 5.31: Same as Figure 5.11 but for PSR J2032+4127.

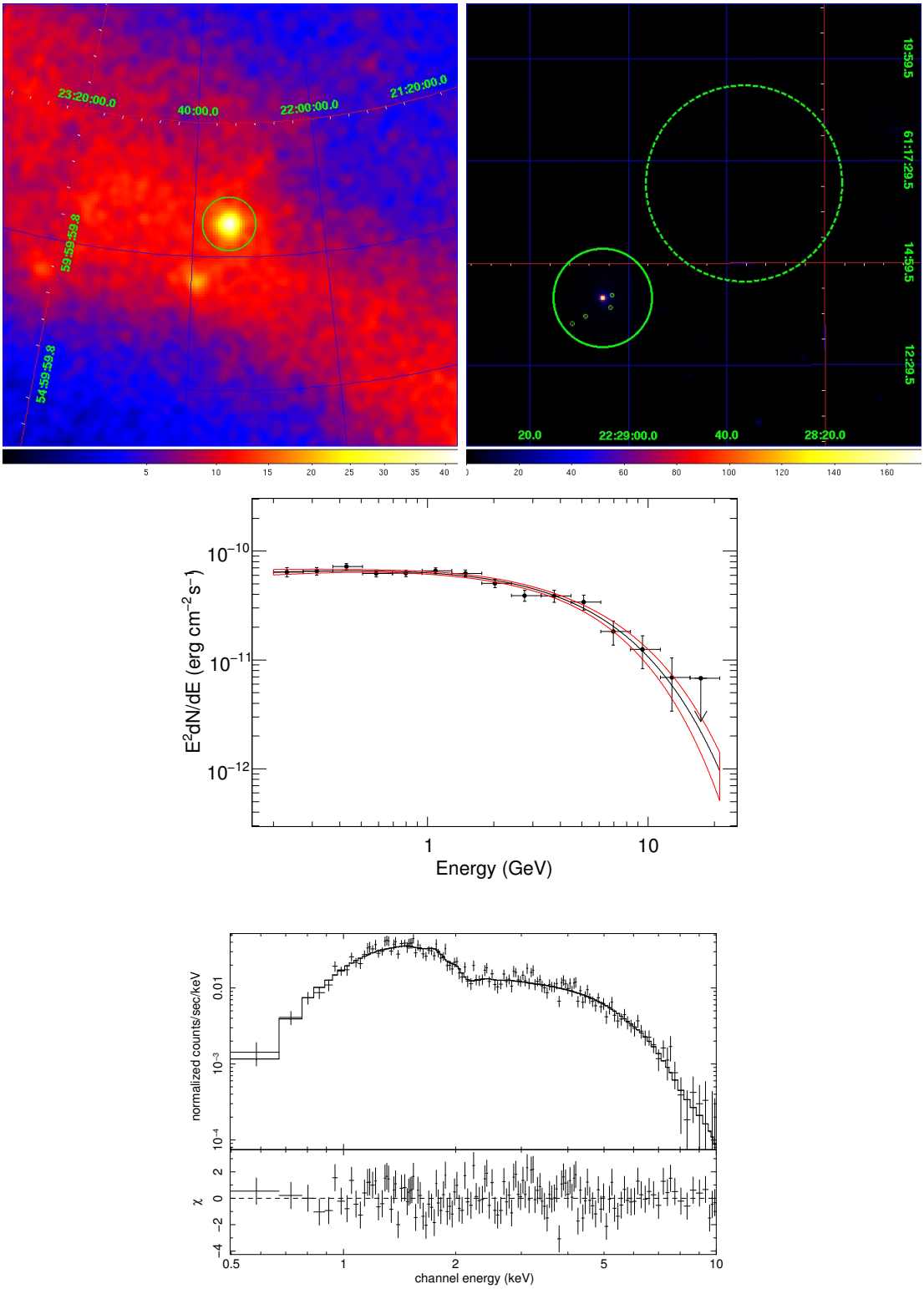

Figure 5.32: Same as Figure 5.11 but for PSR J2229+6114.

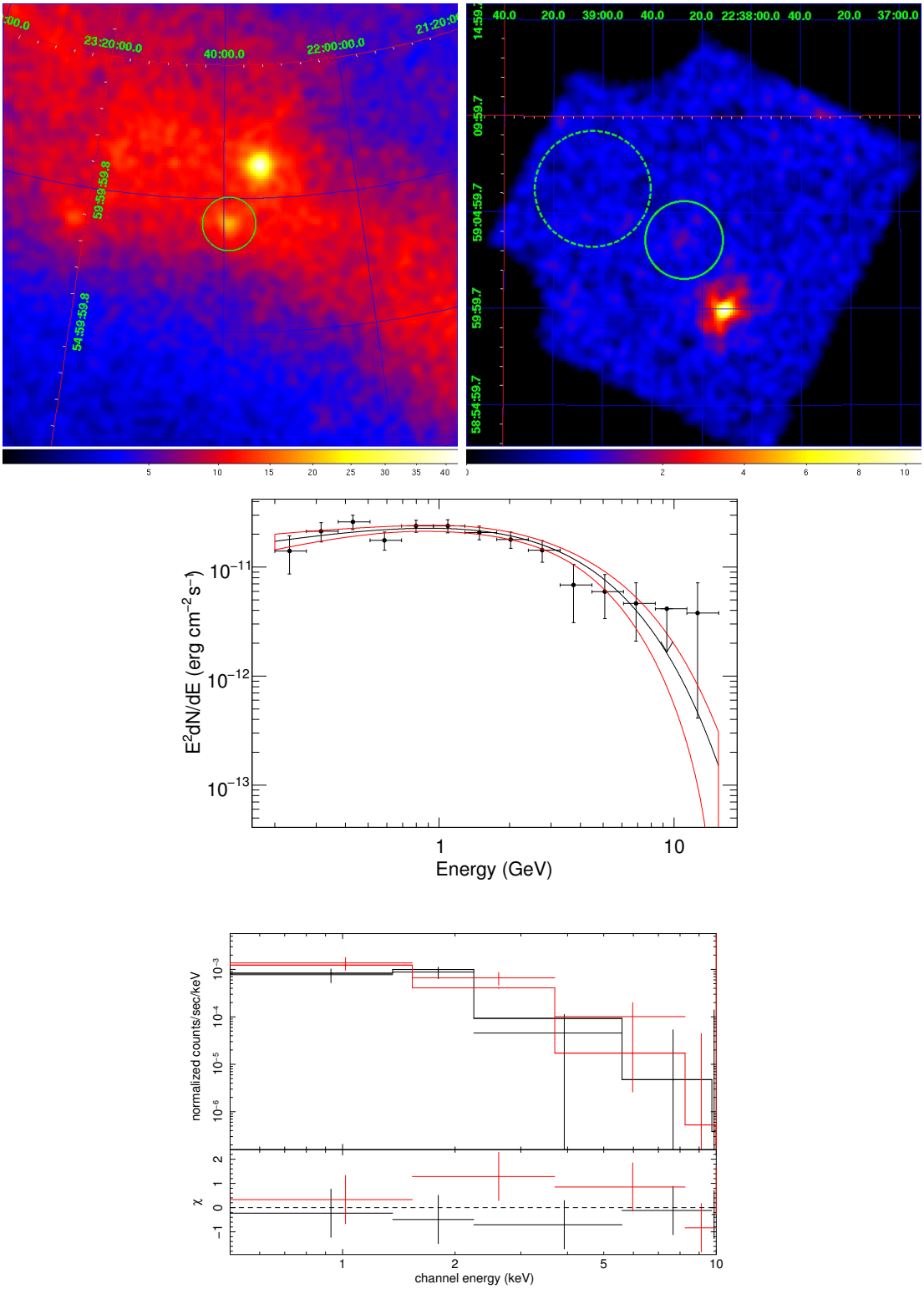

Figure 5.33: Same as Figure 5.11 but for PSR J2238+59.

Chapter 6

Discussion

In this chapter, we discuss differences between the radio- and gamma-selected pulsars. In principle the gamma-ray pulsars must be classified by the radio flux but we do not know the radio flux of all the new gamma-ray pulsars yet. Therefore we adopt the wavelength which detected each pulsar first as the classification criterion for this study.

Since the outer gap emission scheme is now preferable theoretically and observationally, the discussions are based on the outer gap model.

6.1 Distributions of basic physical parameters

Before discussing the obtained spectral data, we compare all the LAT pulsars' basic physical parameters calculated with periods and period derivatives: spin-down luminosity, characteristic age, surface magnetic field, magnetic field at the light cylinder, Goldreich-Julian density and open field line potential difference (see review §2.3 for details).

Figure 6.1 shows histograms of the calculated parameters. Distributions of radio-selected and gamma-selected pulsars look similar while values of millisecond pulsars obviously differ. More quantitatively, we calculated mean μ and standard deviation σ of common logarithm of each value with

$$\mu = \frac{1}{N}\sum_{i=1}^{N} \log_{10} x_i \tag{6.1}$$

and

$$\sigma^2 = \frac{1}{N-1}\sum_{i=1}^{N} \left(\log_{10} x_i - \mu\right)^2 , \tag{6.2}$$

where N is the number of samples. The results are summarized in Table 6.1. The uncertainties of means are estimated with $\sigma/\sqrt{N}$. The values for millisecond pulsars are listed just for information and they will never be discussed in this study.

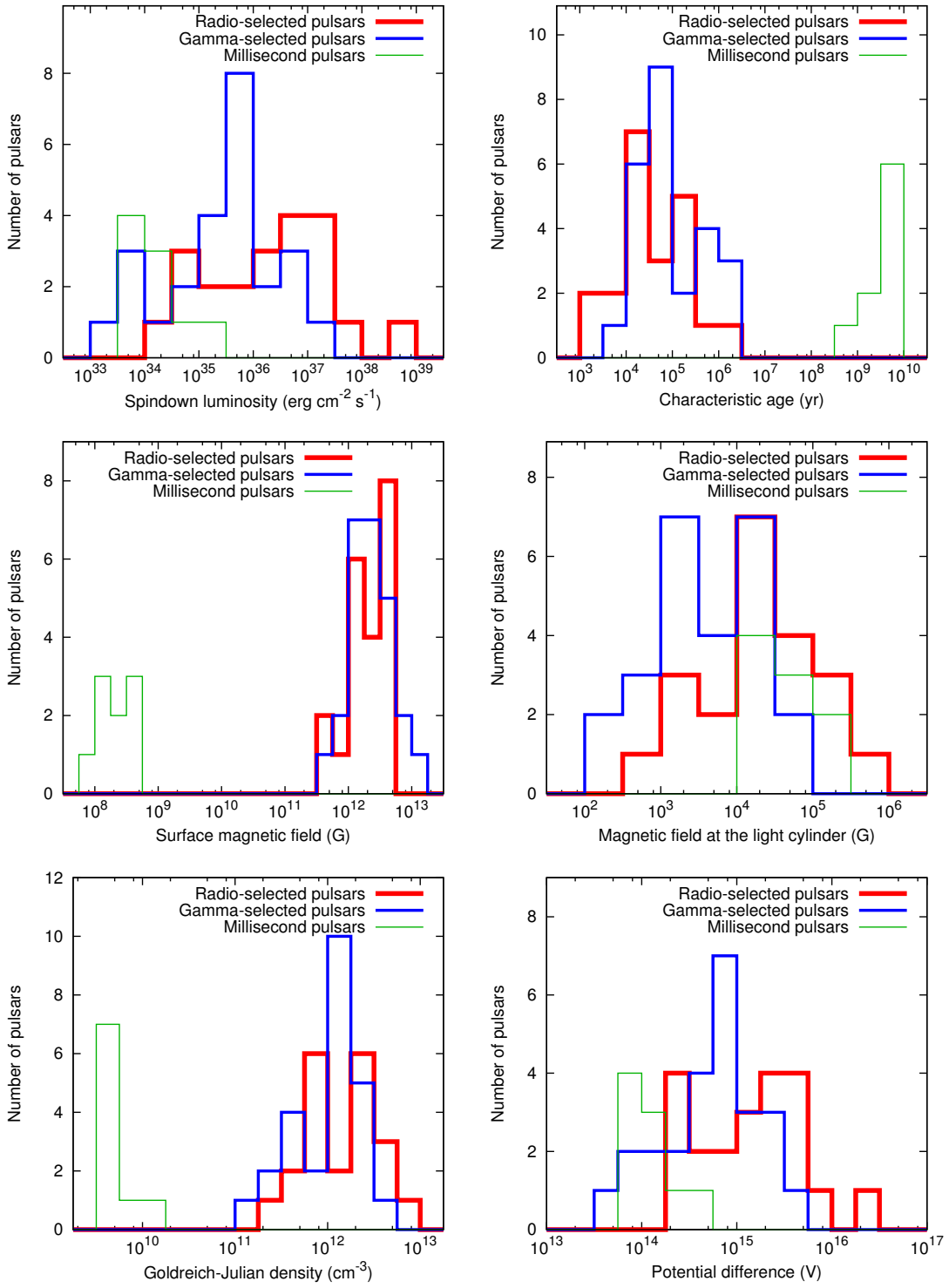

Figure 6.1: Histograms of basic physical parameters for all the pulsars detected by the *Fermi* LAT; spin-down luminosity (top left), characteristic age (top right), surface magnetic field (middle left), magnetic field at the light cylinder (middle right), Goldreich-Julian density (bottom left) and open field line potential difference (bottom right).

Table 6.1: Means and standard deviations of the common logarithm of pulsar parameters.

	Radio-selected		Gamma-selected		Millisecond	
Parameter	μ	σ	μ	σ	μ	σ
$L_{\rm sd}$	36.23 ± 0.25	1.12	35.38 ± 0.21	1.06	34.12 ± 0.18	0.55
$\tau_{\rm c}$	4.556 ± 0.169	0.775	4.933 ± 0.143	0.716	9.581 ± 0.133	0.40
$B_{\rm s}$	12.33 ± 0.08	0.36	12.38 ± 0.06	0.31	8.36 ± 0.08	0.24
$B_{\rm lc}$	4.277 ± 0.172	0.790	3.616 ± 0.148	0.740	4.685 ± 0.133	0.40
$n_{\rm GJ}$	12.17 ± 0.08	0.39	11.98 ± 0.07	0.36	9.66 ± 0.07	0.20
$\Delta\Phi$	15.14 ± 0.12	0.56	14.71 ± 0.11	0.53	14.09 ± 0.09	0.27

Units: $L_{\rm sd}$ (erg s^{-1}), $\tau_{\rm c}$ (yr), $B_{\rm s}$ (G), $B_{\rm lc}$ (G), $n_{\rm GJ}$ (cm^{-3}), $\Delta\Phi$ (V).

As a result, there are small but significant differences between the means of the radio- and gamma-selected pulsars. Gamma-selected pulsars are less energetic and older on average. On the other hand, those means are well within the standard deviations, which is one of suggestions that radio- and gamma-selected pulsars may belong to the same population.

Let us discuss why gamma-selected LAT pulsars are less energetic than radio-selected ones. Gamma-ray pulsations from the radio-selected pulsars have been found utilizing the accurate coordinates and the ephemerides which have been already known in radio observations. The result that gamma-selected pulsars are less energetic looks counter-intuitive considering the fact that there are $\sim$ 1000 known radio pulsars with smaller spin-down luminosities ($< 10^{33}$ erg s^{-1}) and larger characteristic ages ($> 3 \times 10^6$ yr), which are far beyond the distributions shown in Figure 6.1. Both groups of the radio- and gamma-selected pulsars are not complete sets. It is more difficult to detect pulsars near the Galactic center on the celestial sphere in the both wavelengths. There should be other biases and they cannot be considered precisely.

At first we consider that a ratio of the gamma-ray luminosity to the radio luminosity would change with the spin-down luminosity. If the ratio increases with decreasing spin-down luminosity, pulsars with low spin-down luminosity could be discovered with *Fermi* LAT more easily than with radio telescopes. This could explain the reason why the gamma-selected pulsars are older but there is no evidence which supports the assumption above. Figure 6.2 is a plot of a ratio of gamma-ray flux to a radio differential flux at 1400 MHz for eight radio-selected pulsars analyzed in this study (see Table 4.1). Radio flux are drawn from Camilo et al. (2002) [98] for PSR J0205+6449, Keith et al. (2008) for PSR J1028−5819 [97], Hobbs et al. (2004) for PSR J1048−5832 [99], Kramer et al. (2003) for

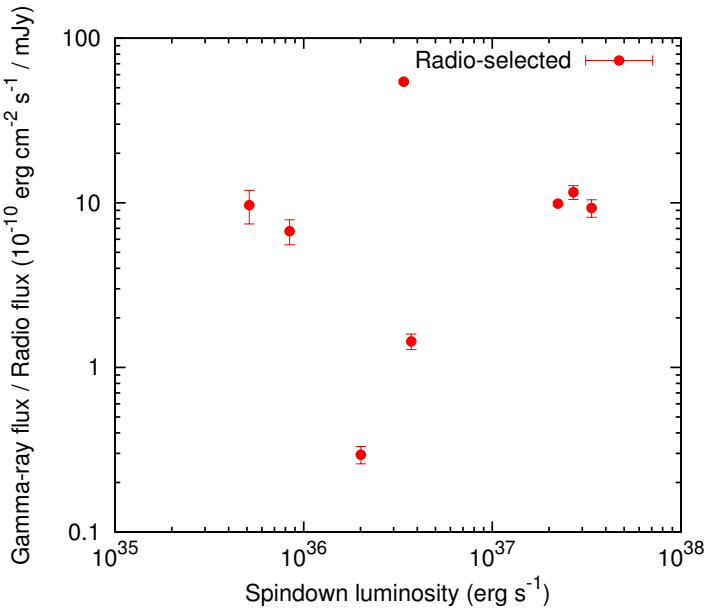

Figure 6.2: Variation of a ratio of the gamma-ray flux ($0.1 - 100$ GeV) to the radio differential flux at 1400 MHz with a spin-down luminosity. There is a large deviation and no correlation seen in this plot, which suggest that the observed gamma-ray and/or radio flux depend on the geometry of pulsar magnetosphere and/or the viewing angle.

PSR J1509−5850 [100], Camilo et al. (2006) for PSR J1833−1034 [101], Lorimer et al. (1995) for PSR J1952+3252 [102], Roberts et al. (2002) for PSR J2021+3651 [103] and Halpern et al. (2001) for PSR J2229+6114 [104]. Note that there is no uncertainty due to distances to the pulsars because we think about flux ratios. There is a large deviation and no correlation seen in Figure 6.2. This suggests that the observed gamma-ray and/or radio flux depend on the geometry of pulsar magnetosphere and/or the viewing angle. Thus this plot does not support the assumption of the flux ratio changing with the spin-down luminosity.

Next we assume that the solid angles of radio and/or gamma-ray beams change with the spin-down luminosity. Smaller (larger) solid angle corresponds to lower (higher) probability of pulsation detection. If the ratio of radio beam width to gamma-ray beam width decreases with the pulsar spin-down, radio beams have more chances to be missed. That may explain the observed distribution differences between radio- and gamma-selected pulsars. There is an observational study of the evolution of radio beams. Rankin (1993) [105] reported that the width of a radio beam W decreases with a rotation period by

$$W = 5.8^{\circ} P^{-1/2}. \tag{6.3}$$

The trend of $\propto P^{-1/2}$ reflects the relationship between the width of the polar cap region

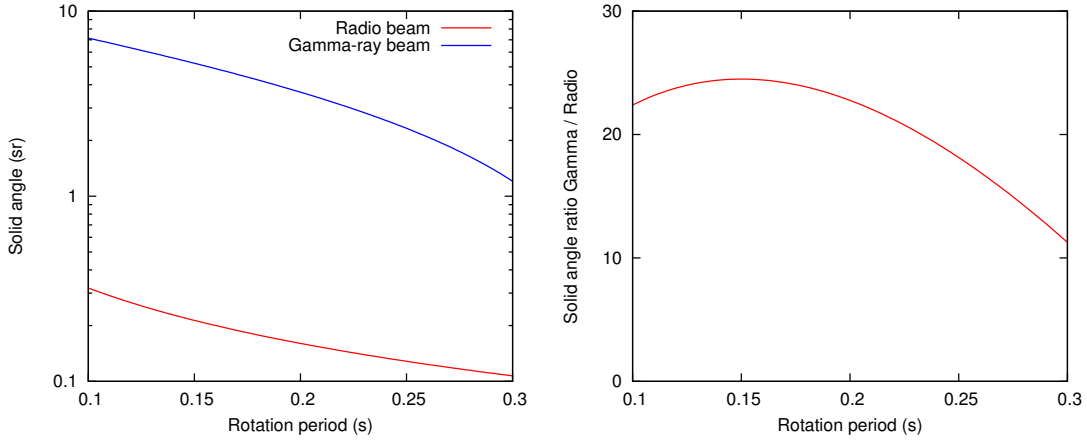

Figure 6.3: (Left) Solid angles of radio and gamma-ray beams derived with Equations (6.3) and (6.4). We assumed $\alpha = 90°$, $b = 0.5$ and $B = 10^{12}$ G. (Right) Ratio of the solid angle of the gamma-ray beam to that of the radio beam as a function of rotation period.

and the rotation period (equation 2.24).

Regarding gamma-ray beams, no observational result has been reported yet. One of predictions by Zhang et al. (2000) [106] states the gamma-ray beaming fraction f_γ is expressed by

$$f_\gamma \sim \left(\frac{\alpha}{90°}\right)^a \frac{1 - bf_s}{1 + bf_s}, \tag{6.4}$$

where α is the magnetic inclination angle of the pulsar, $a \sim 0.5$, $b \sim 0.5$ and f_s is the ratio of the average vertical separation of the outer gap boundaries in the plane of $(\vec{\Omega}, \vec{\mu})$ to the radius of the light cylinder,

$$f_s \sim 5.5 \times P^{26/21} \left(\frac{B}{10^{12}\mathrm{G}}\right)^{-4/7} \leq 1. \tag{6.5}$$

This relation shows f_γ decreases with the pulsar spin-down, increasing P. Figure 6.3 shows the evolution of the solid angles of radio and gamma-ray beams, and their ratio assuming $\alpha = 90°$, $b = 0.5$ and $B = 10^{12}$ G in equations (6.4) and (6.5)[1] . If the prediction on gamma-ray beams by Zhang et al. (2000) is correct, the ratio of radio beam detection probability to that of gamma-ray beam becomes higher with the pulsar spin-down, which does not agree with our assumption.

Another prediction about the gamma-ray beam is shown by Hirotani (2008) [107], which states that the trans-field (vertical to the magnetic field line) thickness of the outer gap becomes wider with the pulsar's spin-down. Therefore the gamma-ray beam does so, too, and the prediction is in favor of our results. However the time evolution of the width

[1] Generally the surface magnetic field does not depend on the rotation period for normal pulsars.

Table 6.2: Weighted means μ and standard deviations σ of spectral parameters.

	Radio-selected		Gamma-selected	
Parameter	μ	σ	μ	σ
X-ray photon index	1.80 ± 0.01	0.19	1.89 ± 0.02	0.41
Gamma-ray photon index	1.73 ± 0.03	0.21	1.33 ± 0.01	0.31
Gamma-ray cutoff energy (GeV)	3.01 ± 0.16	0.71	2.44 ± 0.03	0.91

is not shown. The calculation is reliable because it is based on only the Maxwell and Boltzmann equations and does not depend on any ad-hoc assumptions.

Our results might have some observational implications on the evolution of gamma-ray emission beam. Other kinds of information like light curves and phase-resolved spectra should be added to deepen our knowledge about the emission geometry and its evolution. These factors can affect the population studies of pulsars.

6.2 Comparison of spectral parameters

At first, we checked distributions of the obtained spectral parameters. Figure 6.4 shows the distributions of X-ray and gamma-ray photon indices ($\Gamma_{\rm X}$ and Γ_γ). Figure 6.5 shows the distribution of cutoff energy of gamma-ray spectrum ($E_{\rm cut}$). Errors are shown in the scatter plots. We point out that the correlations between $\Gamma_{\rm X}$ and Γ_γ, and between Γ_γ and $E_{\rm cut}$ are not seen due to the large statistical errors.

We also calculated the weighted means and the standard deviations for each parameter as summarized in Table 6.2. The weighted means are not consistent with each other but we cannot conclude immediately that there are spectral differences between the radio- and gamma-selected pulsars because the parameters may depend on the other parameters such as the spin-down luminosity.

Figure 6.6 shows the variation of the spectral parameters with the spin-down luminosity. In those scatter plots, there seems to be no differences in the distributions of radio- and gamma-selected pulsars. This is the second suggestion that the radio- and gamma-selected pulsars come from the same population.

Correlations can be seen in Figure 6.6. If we handle radio- and gamma-selected pulsars together, empirical model fits resulted in

$$\Gamma_{\rm X} = (2.02 \pm 0.07) - (0.067 \pm 0.022) \times \log_{10}\left(\frac{L_{\rm sd}}{10^{34}\ {\rm erg\ s^{-1}}}\right), \tag{6.6}$$

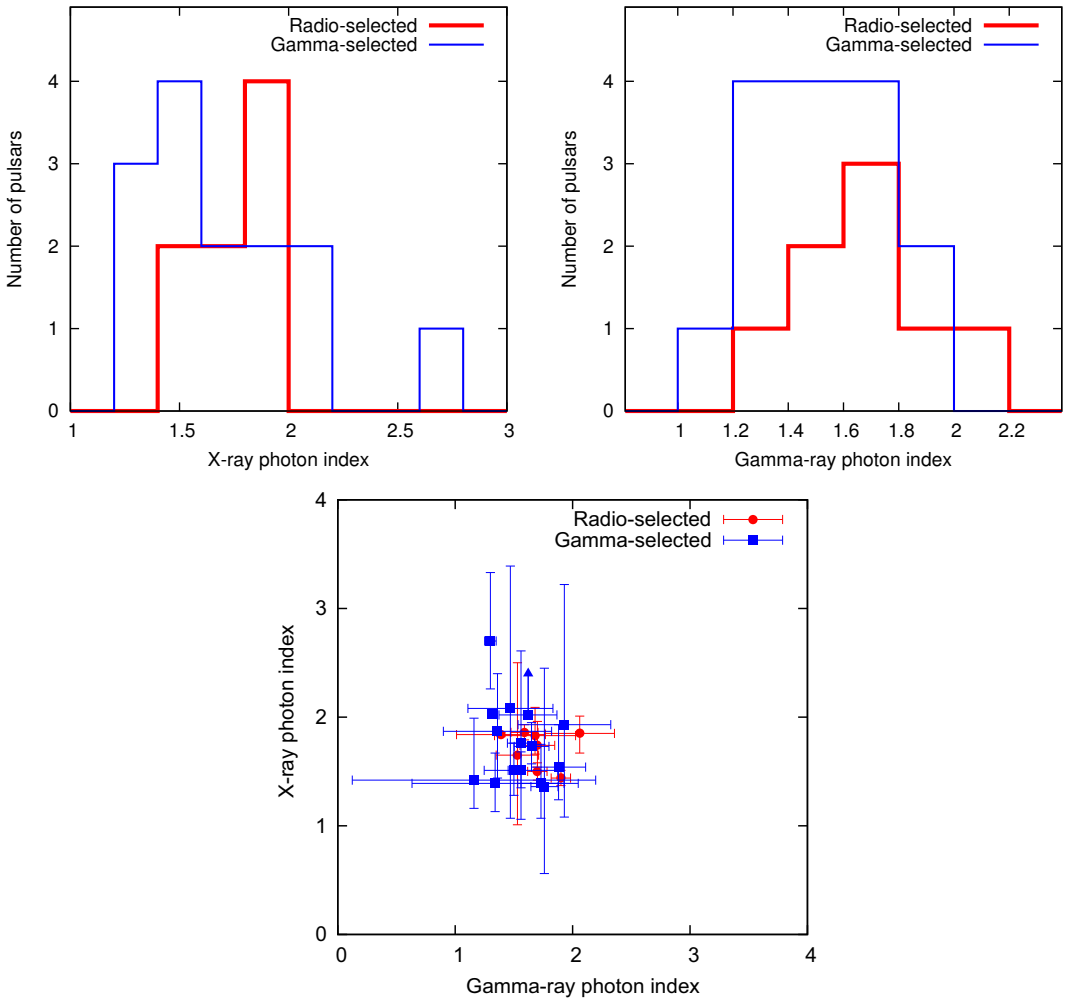

Figure 6.4: (Top left) Distribution of X-ray photon index. (Top right) Distribution of gamma-ray photon index. (Bottom) Scatter plot of X-ray and gamma-ray photon indices. Errors with 90% confidence level are presented.

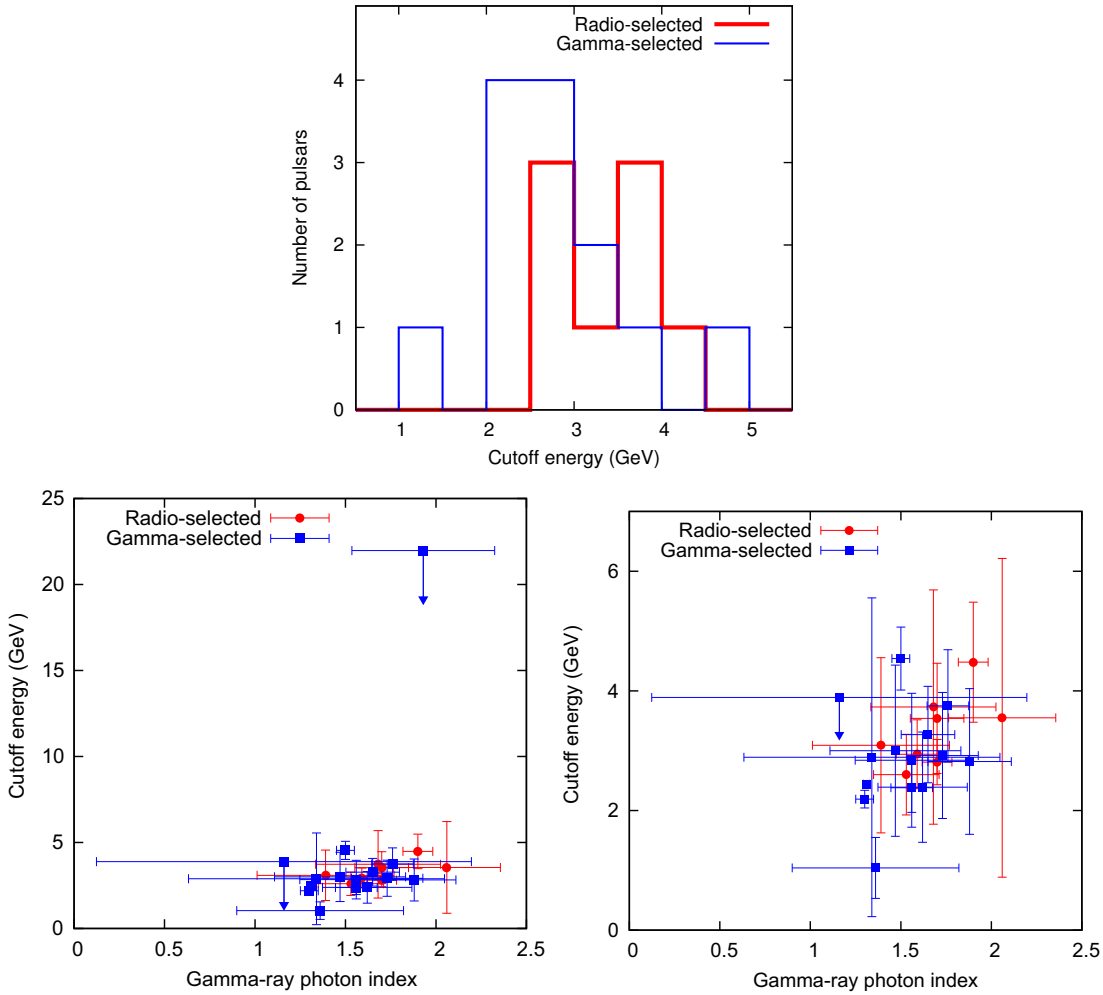

Figure 6.5: (Top) Distribution of the gamma-ray cutoff energy. (Bottom left) Scatter plot of the gamma-ray photon index and the cutoff energy. (Bottom right) Zoomed plot of the bottom left figure between the cutoff energy $0 - 7$ GeV. Errors indicate 90% confidence level.

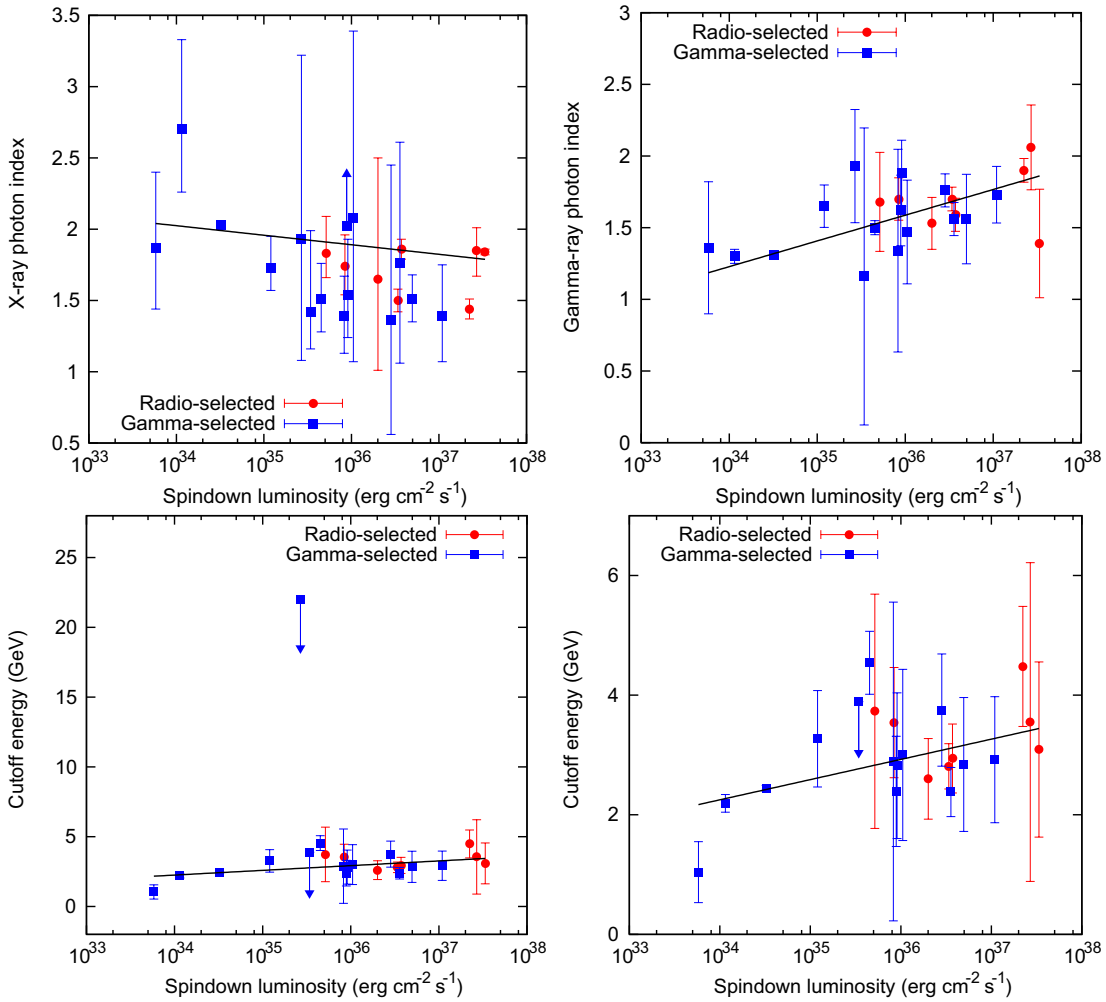

Figure 6.6: Variation of spectral parameters against the spin-down luminosity; X-ray photon index (top left), gamma-ray photon index (top right), cutoff energy (bottom left) and zoomed plot of cutoff energy between 0–7 GeV (bottom right). The solid lines show best-fit empirical functions.

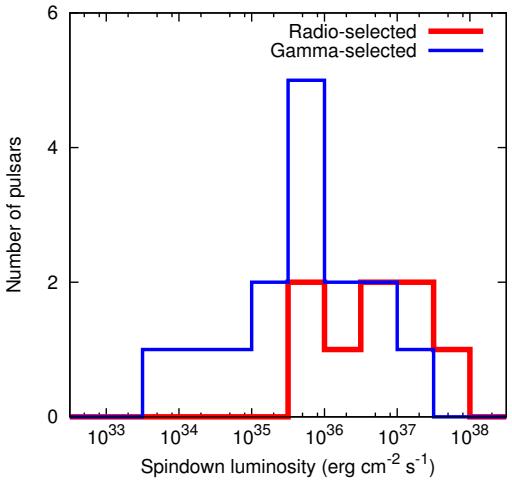

Figure 6.7: Histogram of the spin-down luminosity of analyzed pulsars.

$$\Gamma_\gamma = (1.23 \pm 0.02) + (0.179 \pm 0.015) \times \log_{10}\left(\frac{L_{\rm sd}}{10^{34}\ {\rm erg\ s^{-1}}}\right) \tag{6.7}$$

and

$$E_{\rm cut} = (2.25 \pm 0.08) + (0.338 \pm 0.102) \times \log_{10}\left(\frac{L_{\rm sd}}{10^{34}\ {\rm erg\ s^{-1}}}\right) ({\rm GeV}), \tag{6.8}$$

where 1σ statistical errors are presented. Since the slopes are inconsistent with zero, we consider there are significant correlations between the spin-down luminosity and $\Gamma_{\rm X}$, Γ_γ and $E_{\rm cut}$. The relationship between the spin-down luminosity and $\Gamma_{\rm X}$ can be arisen with two data points with tiny error bars at ($L_{\rm sd}$, $\Gamma_{\rm X}$) = (3.3×10^{34}, 2.03) and (3.4×10^{37}, 1.84). When removing those points, the fit still has a significant slope;

$$\Gamma_{\rm X} = (1.96 \pm 0.18) - (0.126 \pm 0.067) \times \log_{10}\left(\frac{L_{\rm sd}}{10^{34}\ {\rm erg\ s^{-1}}}\right). \tag{6.9}$$

The differences in the histograms shown in Figures 6.4 and 6.5 can be explained with these relationships. Among the analyzed pulsars, radio-selected ones have higher spin-down luminosity as shown in Figure 6.7, and this causes the difference of spectral parameters between the radio- and gamma-selected pulsars. Table 6.3 shows expected averages of the spectral parameters if pulsars obey the empirical relations represented by the above equations. Although they do not absolutely reproduce the observed values of course, they show the trend of the differences shown in Table 6.2.

Next, the obtained empirical relationships are discussed. There are some reports about variation of the X-ray photon index. Becker & Trümper (1997) studied X-ray spectra of pulsars in a wide range of spin-down luminosities ($L_{\rm sd} \sim 10^{32} - 10^{38}$ erg s^{-1}) using *ROSAT* and *ASCA* data. They concluded that photon index does not change with the characteristic age [108]. The constant photon index also has been reported by Saito

Table 6.3: Expected averages of spectral parameters of radio- and gamma-selected pulsars when the fitted empirical relationships are assumed.

Parameter	μ (radio-selected)	μ (gamma-selected)
X-ray photon index	1.85 ± 0.02	1.91 ± 0.02
Gamma-ray photon index	1.71 ± 0.04	1.52 ± 0.04
Gamma-ray cutoff energy (GeV)	3.15 ± 0.08	2.80 ± 0.08

(1998) for X-ray pulsars including newly observed with *ASCA*, whose range of the spin-down luminosity is almost same as that of Becker & Trümper (1997) [109]. On the other hand, Gotthelf (2003) studied nine "Crab-like" pulsars (pulsars embedded in bright X-ray pulsar wind nebulae) with *Chandra* to resolve emission from pulsars and pulsar wind nebulae [110]. He reported that the photon index varies with the spin-down luminosity. The best fit models for photon index of pulsars ($\Gamma_{\rm PSR}$) and pulsar wind nebulae ($\Gamma_{\rm PWN}$) in 2–10 keV band are derived as

$$\Gamma_{\rm PSR} = (2.08 \pm 0.07) - (0.029 \pm 0.003) \times \left(\frac{L_{\rm sd}}{10^{40}\ {\rm erg\ s^{-1}}} \right)^{-1/2} \tag{6.10}$$

and

$$\Gamma_{\rm PWN} = (2.36 \pm 0.33) - (0.021 \pm 0.005) \times \left(\frac{L_{\rm sd}}{10^{40}\ {\rm erg\ s^{-1}}} \right)^{-1/2}. \tag{6.11}$$

Therefore the more energetic a pulsar is, the larger (softer) its photon index is. This trend is opposite to our result. We would like to point out that the samples in Gotthelf (2003) are biased to highest spin-down luminosities ($L_{\rm sd} \sim 10^{36} - 10^{38}$ erg s^{-1}). Li et al. (2008) revisited the relations using 27 pulsars ranging in $L_{\rm sd} \sim 10^{32} - 10^{38}$ erg s^{-1} observed with *Chandra* [111], and found out

$$\Gamma_{\rm PSR} = (5.7 \pm 0.6) - (0.11 \pm 0.02) \times \log_{10} L_{\rm sd} \tag{6.12}$$

and

$$\Gamma_{\rm PWN} = (-5.7 \pm 0.3) + (0.203 \pm 0.008) \times \log_{10} L_{\rm sd}. \tag{6.13}$$

The trend of equation (6.12) agrees with our $L_{\rm sd} - \Gamma_{\rm X}$ relation while the results of Gotthelf (2003) are opposite results to ours. Even though in our observations it is hard to distinguish emission from the pulsar wind nebulae[2] , this result suggests that the pulsar components dominate in our samples.

[2] Especially with *Suzaku*, but even *XMM-Newton* or *Chandra* cannot resolve nebula emission if it is compact, either.)

The outer gap model predicts the X-ray photon index ≈ 1 [17], but not its evolution. When we assume the X-ray emission arises by synchrotron processes, which is expected with the outer gap model, X-ray energy spectrum $\propto E^{-\Gamma}$ reflects the electron energy distribution $\propto \gamma^{-p}$ by

$$\Gamma = \frac{p-1}{2}, \tag{6.14}$$

where γ is the Lorentz factor of the particles [112]. Therefore the larger X-ray photon index have larger fraction of low-energy electrons, which is a natural implication.

Regarding the gamma-ray photon index, Thompson et al. (1994) [113] reported that it decreases with the characteristic age;

$$\Gamma_\gamma = 3.08 - 0.33 \log\left(\frac{\tau_{\rm c}}{1\ {\rm yr}}\right)\ . \tag{6.15}$$

Our result shows the same trend. In the outer gap model, curvature radiation is expected to dominate in the GeV gamma-ray regime. Like the synchrotron process, the photon index of the curvature radiation corresponds to the energy spectrum of electrons;

$$\Gamma = \frac{p-1}{3}. \tag{6.16}$$

Therefore the softer gamma-ray spectrum indicates the softer electron spectrum. The primary electrons from the neutron star surface are predicted to be accelerated in the outer gap region and produce curvature radiation. The intensity of curvature radiation caused by mono-energetic particles with Lorentz factor γ is expressed as

$$I(\nu) \approx \frac{1}{2\pi}\frac{e^2}{c}\frac{c}{\rho}\gamma\left(\frac{\nu}{\nu_c}\right)^{1/3} \qquad (\nu < \nu_c), \tag{6.17}$$

where e is the elementary charge, c is the speed of light and ρ is the curvature radius [114]. ν_c is the critical frequency given by

$$\nu_c \approx \frac{c}{2\pi\rho}\gamma^3. \tag{6.18}$$

Since the curvature radius is approximately the half of the light cylinder radius $R_{\rm lc}$, it is proportional to the rotation period;

$$\rho \approx \frac{R_{\rm lc}}{2} = \frac{cP}{4\pi} \propto P, \tag{6.19}$$

and the maximum Lorentz factor is proportional to $L_{\rm sd}^{1/2}$;

$$\gamma \approx \frac{e\Phi}{m_e c^2} \propto L_{\rm sd}^{1/2}, \tag{6.20}$$

then the intensity of the curvature radiation has a relation given by

$$I(\nu) \propto \frac{\gamma}{\rho} \propto L_{\rm sd}^{1/2} P^{-1}. \tag{6.21}$$

Therefore, in less energetic pulsar system, primary electrons are more difficult to be cooled via the curvature radiation and are expected to have higher energies, which corresponds to the flatter energy distribution. This simple and qualitative explanation agrees with the observed trend of the gamma-ray photon index.

Regarding the trend of cutoff energy, the similar estimation can be adopted with the critical frequency (6.18);

$$\nu_c \propto \frac{\gamma^3}{\rho} \propto L_{\rm sd}^{3/2} P^{-1}. \tag{6.22}$$

In this case, more energetic pulsar can accelerate primary electrons to higher energies, which results in higher cutoff energy in the photon spectrum.

6.3 Luminosity and distance estimation

We calculate X-ray and gamma-ray luminosities for pulsars whose distance is already known. There are 13 samples (8 radio-selected and 5 gamma-selected pulsars) among pulsars we analyzed. We used distances summarized in Table 6.4. The luminosity L is estimated with $L = 4\pi D^2 f F$, where D is the distance to the pulsar, f is the beaming correction factor and F is the observed flux. The beaming correction factor is often used to correct geometrical differences due to the limited solid angle of the emission beam but we assume $f = 1$ (isotropic emission) herein.

Figure 6.8 shows the scatter plots of X-ray and gamma-ray luminosities versus the spin-down luminosity. In the X-ray plot, data points of radio- and gamma-selected pulsars show a strong correlation. This is the third suggestion that the radio- and gamma-selected pulsars belong to the same population. When the all data points are fitted with a power-law function, we obtain

$$\frac{L_{\rm X}}{10^{32}\ {\rm erg\ s^{-1}}} = (2.99 \pm 1.08) \times \left(\frac{L_{\rm sd}}{10^{36}\ {\rm erg\ s^{-1}}} \right)^{1.10 \pm 0.14}, \tag{6.23}$$

with a reduced χ^2 of 1.086 (10.86/10). On the other hand, gamma-ray luminosity has nothing to do with the spin-down luminosity;

$$\frac{L_{\gamma}}{10^{34}\ {\rm erg\ s^{-1}}} = (8 \pm 3) \times \left(\frac{L_{\rm sd}}{10^{36}\ {\rm erg\ s^{-1}}} \right)^{0.06 \pm 0.10}. \tag{6.24}$$

The strong correlation of $L_{\rm sd} - L_{\rm X}$ is well known for radio pulsars but we confirmed that the same relation is also true for gamma-ray pulsars for the first time. Becker & Trümper (1997) reported a roughly fitted function $L_{\rm X} \approx 10^{-3} \times L_{\rm sd}$ in the energy band of $0.1 - 2.4$ keV for 26 pulsars in $L_{\rm sd} \sim 10^{32} - 10^{38}$ erg s^{-1}[108]. Saito (1998) studied the relationship in the higher energy band ($2 - 10$ keV) and obtained a rough trend $L_{\rm X} \approx 10^{-23} \times L_{\rm sd}^{3/2}$

Table 6.4: Used values of distance to pulsars.

JName	Type[a]	Distance (kpc)	Reference
J0007+7303	g	1.4 ± 0.3	[115]
J0205+6449	r	$2.6 \sim 3.2$	[116, 117]
J0633+1746	g	$0.250^{+0.120}_{-0.062}$	[118]
J1028−5819	r	2.33 ± 0.70	[97]
J1048−5832	r	2.71 ± 0.81	[119]
J1418−6058	g	$2 \sim 5$	[120, 121]
J1509−5850	r	2.6 ± 0.8	[122]
J1833−1034	r	4.7 ± 0.4	[101]
J1836+5925	g	< 0.8	[123]
J1952+3252	r	2.0 ± 0.5	[124]
J2021+3651	r	$2.1^{+2.1}_{-1.0}$	[125]
J2032+4127	g	$1.6 \sim 3.6$	[126]
J2229+6114	r	$0.8 \sim 6.5$	[127, 128]

[a] See Table 2.1.

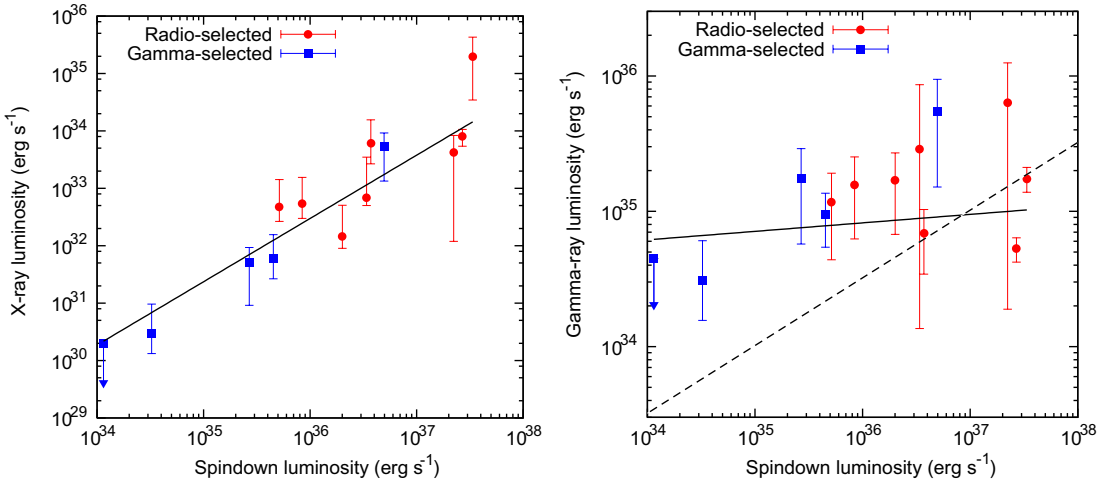

Figure 6.8: Variation of X-ray (left) and gamma-ray (right) luminosities with the spin-down luminosity. The isotropic emission is assumed for the calculation. The solid lines show best fit models (see text). The dashed line is a $L_\gamma \propto L_{\rm sd}^{1/2}$ function shown in Figure 6 of Abdo et al. (2009) [12].

with five samples [109]. None of these studies considered uncertainties on $L_{\rm X}$ from flux and distance errors. In addition, Possenti et al. (2002) performed an intensive survey on this issue with 39 samples and obtained a model $L_{\rm X} = 10^{-15.34\pm1.11} \times L_{\rm sd}^{1.34\pm0.03}$ for the $2-10$ keV band [129]. All these studies handled emission from pulsars and pulsar wind nebulae together, thus the analysis method is similar to that of this work. The trend of our result $\propto E^{1.10\pm0.14}$ is consistent with the result of Becker & Trümper (1997). Using the average X-ray photon index 1.9, their result can be extrapolated into the $0.5-10$ keV band as

$$\frac{L_{\rm X}}{10^{32}\ {\rm erg\ s^{-1}}} \approx 11 \times \frac{L_{\rm sd}}{10^{36}\ {\rm erg\ s^{-1}}}, \tag{6.25}$$

which may be compared to our result (6.23). We do not conclude that the scaling factor is different because the X-ray flux obtained for lower energy band (< 2 keV) may have large uncertainty due to the uncertainty of the interstellar absorption. Our result as well as Becker & Trümper (1997) is theoretically supported by Cheng et al. (1998) based on the outer gap model. Their estimate of the X-ray luminosity is

$$L_{\rm X} \approx 5.5 \times 10^{-4} \left(\frac{\tan\chi}{\tan 55^\circ}\right)^4 \left(\frac{B}{10^{12}\ {\rm G}}\right)^{0.13} \left(\frac{P}{0.1\ {\rm s}}\right)^{-0.80} L_{\rm sd}, \tag{6.26}$$

where χ is the angle between the rotation axis and the magnetic dipole of the pulsar. The fraction of X-ray luminosity to the spin-down luminosity is about $10^{-4} - 10^{-3}$ and our result agrees with the prediction, when the X-ray emission is assumed to be nearly isotropic ($f \approx 1$).

Equation (6.23) is a useful tool to roughly estimate distances to pulsars if one knows their X-ray fluxes. We have ten new gamma-selected pulsars with unknown distances, which we estimated as summarized in Table 6.5. Considering the deviation of an order of magnitude seen in the $L_{\rm sd} - L_{\rm X}$ plot (Figure 6.8), there may be an uncertainty of at least factor of 3 ($\times 1/3 \sim \times 3$). Figure 6.9 shows the variation of pulsars' distance with the characteristic age. Conservative errors (an order of magnitude) are added on the new gamma-selected pulsars with estimated distances. Within 1 kpc from the earth, there are four gamma-selected and two radio-selected pulsars from the older ($\tau_c > 10^5$ yr) population. Although the number of samples are too small, this may imply that the *Fermi* LAT, or the gamma-ray observation, is sensitive to nearby old pulsars, which agrees with the fact that gamma-selected pulsars tends to be less energetic and older in average, as we pointed out in §6.1. Population studies should be performed with including this nature of pulsars.

Gamma-ray luminosities are thought to follow a relation $L_\gamma \propto L_{\rm sd}^{1/2}$ because L_γ is proportional to the particle current $\dot{N} \propto BP^{-2} \propto \dot{P}^{1/2} P^{-3/2} \propto L_{\rm sd}^{1/2}$. The large scatter in the $L_{\rm sd} - L_\gamma$ plot has been reported by Abdo et al. (2009) [12] and commonly understood

Table 6.5: Distances of ten new gamma-selected pulsars estimated based on their X-ray luminosities. The upper and lower limits are evaluated with a 90% confidence level.

JName	Distance (kpc)
J0357+32	0.2
J0633+0632	0.4
J1022−5746	13.4
J1413−6205	2.9
J1459−60	4.0
J1826−1256	3.8
J1907+06	7.3
J1954+2836	< 34
J1958+2846	3.0
J2238+59	> 0.03

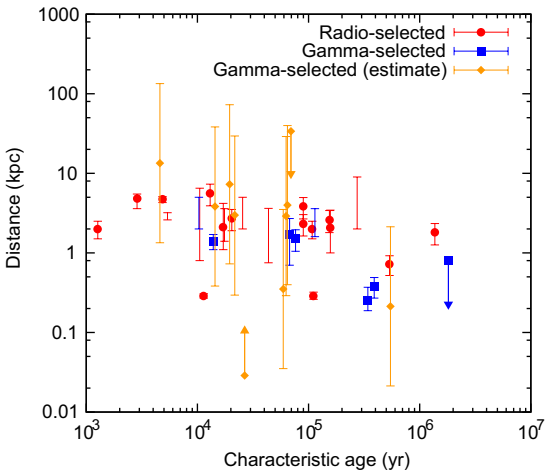

Figure 6.9: Distribution of the distance with the characteristic age. Conservative errors are given to gamma-selected pulsars with estimated distances.

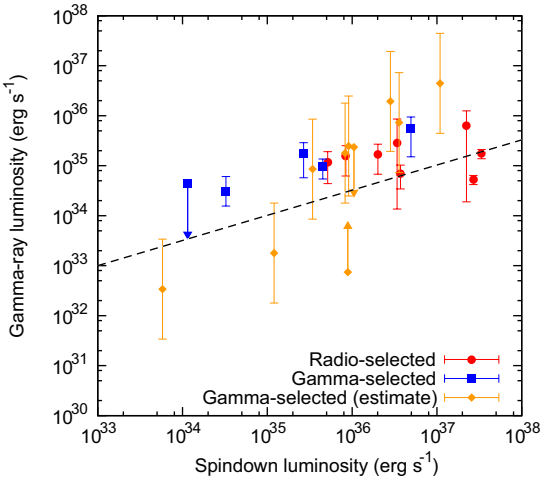

Figure 6.10: Observed and estimated gamma-ray luminosity with the spin-down luminosity. The estimated pulsars have rough uncertainties with an order of magnitude. The dashed line is a heuristic $L_\gamma \propto L_{\rm sd}^{1/2}$ function shown in Figure 6 of Abdo et al. (2009) [12].

as due to a large variety in viewing angles. However we noticed that there are three data points with relatively lower fluxes near or below the heuristic $L_\gamma \propto L_{\rm sd}^{1/2}$ line in Figure 6.8. They are PSR J1833−1034, PSR J0205+6449 and PSR J2021+3651 in order of the spin-down luminosity. It is wondered that radio pulsars tend to have lower gamma-ray luminosity. Since we now have a rough estimation of the new pulsars' distances, they are included in the $L_{\rm sd} - L_\gamma$ plot, too. The resultant plot is shown in Figure 6.10. There three gamma-selected pulsars appear below the $L_\gamma \propto L_{\rm sd}^{1/2}$ line (PSR J1459−60, PSR J0633+0632 and J0357+32, in order of the spin-down luminosity). Thus we conclude that both of radio- and gamma-selected pulsars have the large deviation of observed gamma-ray luminosity.

We have examined variations of X-ray and gamma-ray luminosities for the same 13 pulsar samples. This is the first result that gamma-ray pulsars have a strong correlation of the X-ray luminosity with the spin-down luminosity contrary to the large variety of the gamma-ray luminosity. Therefore it is clear that the X-ray emission does not arise in the same region where the gamma-ray emission does. X-ray emission must be much less beamed than the gamma-ray beam so as not to depend on the individual viewing angles or the geometry of the magnetosphere.

Chapter 7

Conclusion

We examined differences between the pulsars first discovered with radio observations (radio-selected pulsars) and ones first discovered with the *Fermi* LAT (gamma-selected pulsars, including Geminga pulsar).

X-ray observations with *Suzaku* were performed for nine new gamma-selected pulsars and a known radio pulsar PSR J1028−5819. We found probable X-ray counterparts for all of them.

We performed systematic spectral analysis in X-ray and gamma-ray bands for selected 23 pulsar samples, which do not include any millisecond pulsars, with observation data of *Suzaku*, *XMM-Newton*, *Chandra* and *Fermi* LAT. We obtained following results.

1. All X-ray spectra can be modeled with featureless spectral functions – an absorbed power-law or an absorbed power-law and blackbody, and no structures like emission lines are found. The X-ray photon index is less than 2 in most cases, which suggests emission from pulsar magnetosphere, and unabsorbed energy flux of the power-law component is $\sim 10^{-14} - 10^{-10}$ erg cm^{-2} s^{-1} in the $0.5 - 10$ keV band. Gamma-ray spectra are represented with a power-law function with an exponential cutoff. All sources have hard spectra with a photon index of < 2 and a cutoff energy of a few GeV. Typical energy flux is $\sim 10^{-10}$ erg cm^{-2} s^{-1} in $0.1 - 100$ GeV.

2. There are correlations between the spin-down luminosity and the X-ray photon index, the gamma-ray photon index and the cutoff energy. With increasing spin-down luminosity, the X-ray photon index decreases, the gamma-ray photon index increases and the cutoff energy increases. These trends can be explained qualitatively with the outer gap model.

3. There are significant differences between the spectral parameters of radio- and gamma-selected pulsars on average. However they are due to the selection bias;

the radio-selected pulsars have higher spin-down luminosity in our samples.

Among the 23 samples, distances from the earth are known for 13 pulsars (8 radio-selected and 5 gamma-selected). Their X-ray and gamma-ray luminosities are directly derived. The X-ray luminosity has a strong correlation with the spin-down luminosity ($L_{\rm X} \propto L_{\rm sd}^{1.10\pm0.14}$). While the relation is already known in X-ray studies of radio pulsars, we confirmed it is true even for gamma-ray pulsars. Distances for newly found pulsars are estimated using this correlation. In contrast, the gamma-ray luminosity has a large scatter and shows no correlation with the spin-down luminosity possibly due to individual differences of viewing angles. Comparing the $L_{\rm sd} - L_{\rm X}$ and $L_{\rm sd} - L_{\gamma}$ relations, it is observationally confirmed that the X-ray emission is much less beamed than the gamma-ray emission.

We also investigated if all young LAT pulsars (21 radio-selected and 25 gamma-selected ones) have the same distributions of basic physical parameters which can be derived from the rotation period and the spin-down rate. As a result, they have almost the same distributions but their averages are different; the group of gamma-selected pulsars have lower spin-down luminosities and larger characteristic ages on average. For this issue we discussed two possible explanations that (a) the fraction of the gamma-ray luminosity to the radio luminosity or (b) the fraction of the solid angle of the gamma-ray beam to that of the radio beam increases with the pulsar spin-down. While neither of the models cannot be confirmed based on observational results, a theoretical prediction allows the model (b). This study can give suggestions on the time evolution of the gamma-ray beam.

In this survey with X-ray and gamma-ray, we found no evidences implying that radio-selected pulsars and gamma-selected pulsars are pulled from different populations.

Bibliography

[1] A. Hewish et al., Nature 217 (1968) 709.

[2] W. Baade and F. Zwicky, Proceedings of the National Academy of Sciences of the United States of America 20 (1934) 254.

[3] P. Goldreich and W. H. Julian, Astrophysical Journal 157 (1969) 869.

[4] D. J. Thompson et al., Astrophysical Journal 516 (1999) 297.

[5] C. E. Fichtel et al., Astrophysical Journal 198 (1975) 163.

[6] J. P. Halpern and S. S. Holt, Nature 357 (1992) 222.

[7] D. J. Bertsch et al., Nature 357 (1992) 306.

[8] V. M. Malofeev and O. I. Malov, Nature 389 (1997) 697.

[9] R. Ramachandran et al., Astronomy and Astrophysics 339 (1998) 787.

[10] M. A. McLaughlin et al., Astrophysical Journal 512 (1999) 929.

[11] N. E. Kassim and T. J. W. Lazio, Astrophysical Journal 527 (1999) L101.

[12] A. A. Abdo et al., arXiv:0910.1608A (2009).

[13] A. A. Abdo et al., to be submitted to Astrophysical Journal. (Eight gamma-ray pulsars discovered in blind frequency searches of *Fermi* LAT data)

[14] A. A. Abdo et al., submitted to Astrophysical Journal. (Discovery of pulsed gamma-rays from PSR J0034−0534 with the *Fermi* LAT)

[15] F. Camilo et al., Astrophysical Journal 705 (2009) 1.

[16] A. A. Abdo et al., submitted to Astrophysical Journal.

[17] R. W. Romani, Astrophysical Journal 470 (1996) 469.

[18] T. Gold, Nature 218 (1968) 731.

[19] F. Pacini, Nature 219 (1968) 145.

[20] http://www.atnf.csiro.au/research/pulsar/psrcat/

[21] A. G. Lyne et al, Monthly Notices of the Royal Astronomical Society 233 (1988) 667.

[22] R. N. Manchester et al., Nature 313 (1985) 374.

[23] R. N. Manchester and B. A. Peterson, Astrophysical Journal 342 (1989) L23.

[24] A. G. Lyne et al., Nature 381 (1996) 497.

[25] H. Bradt et al., Nature 222 (1969) 728.

[26] R. Browning et al., Nature 232 (1971) 99.

[27] D. A. Kniffen et al., Nature 251 (1974) 397.

[28] D. J. Thompson et al., Astrophysical Journal 200 (1975) L79.

[29] G. Kanbach et al., Astronomy and Astrophysics 90 (1980) 163.

[30] D. J. Thompson, Astrophysics and Space Science Library 304 (2004) 149.

[31] J. M. Fierro et al., Astrophysical Journal 494 (1998) 734.

[32] E. Aliu et al., Science 322 (2008) 1221.

[33] M. A. Ruderman and P. G. Sutherland, Astrophysical Journal 196 (1975) 51.

[34] J. K. Daugherty and A. K. Harding, Astrophysical Journal 252 (1982) 337.

[35] M. G. Baring, Advances in Space Research 33 (2004) 552.

[36] K. S. Cheng et al., Astrophysical Journal 300 (1986) 500.

[37] J. Arons and E. T. Scharlemann, Astrophysical Journal 231 (1979) 854.

[38] A. G. Muslimov and A. K. Harding, Astrophysical Journal 606 (2004) 1143.

[39] A. K. Harding et al., Astrophysical Journal 680 (2008) 1378.

[40] K. Hirotani, submitted to Open Astronomy Journal, arXiv:0809.1283H (2008).

[41] A. A. Abdo et al., Science 322 (2008) 1218.

[42] A. A. Abdo et al., Science 325 (2009) 840.

[43] A. A. Abdo et al., Science 325 (2009) 848.

[44] D. A. Smith et al., Astronomy and Astrophysics 492 (2008) 923.

[45] P. Weltevrede et al., arXiv:0909.5510v1.

[46] W. B. Atwood, et al., Astrophysical Journal 652 (2006) L49.

[47] G. Hobbs et al., Chinese Journal of Astronomy and Astrophysics Supplement 6 (2006) 189.

[48] I.-A. Yadigaroglu and R. W. Romani, Astrophysical Journal 449 (1995) 211.

[49] A. A. Abdo et al., Astrophysical Journal 696 (2009) 1084.

[50] W. B. Atwood et al., Astrophysical Journal 697 (2009) 1071.

[51] A. A. Abdo et al., Astroparticle Physics 32 (2009) 193.

[52] A. A. Abdo et al., Astrophysical Journal Supplement 183 (2009) 46.

[53] A. A. Abdo et al., Astrophysical Journal 700 (2009) 597.

[54] A. A. Abdo et al., Physical Review Letters 102 (2009) 181101.

[55] C. Meegan et al., Astrophysical Journal 702 (2009) 791.

[56] D. J. Thompson et al., Astrophysical Journal Supplement Series 86 (1993) 629.

[57] A. Moiseev et al., Astroparticle Physics 27 (2007) 339.

[58] A. Moiseev et al., Nuclear Instruments and Methods in Physics Research Section A 583 (2007) 372.

[59] W. B. Atwood et al., Astroparticle Physics 28 (2007) 422.

[60] T. Ohsugi et al., Nuclear Instruments and Methods in Physics Research Section A 541 (2005) 29.

[61] R. P. Johnson et al., IEEE Transactions on Nuclear Science 45 (1998) 927.

[62] L. Baldini et al., IEEE Transactions on Nuclear Science 53 (2006) 466.

[63] J. E. Grove et al., in preparation.

[64] A. A. Abdo et al., Astrophysical Journal 707 (2009) 580.

[65] A. A. Abdo et al., Science 323 (2009) 1688.

[66] A. A. Abdo et al., Nature 462 (2009) 331.

[67] A. A. Abdo et al., Astrophysical Journal 706 (2009) L138.

[68] R. Kelley et al., Publications of the Astronomical Society of Japan 59 (2007) S77.

[69] K. Koyama et al., Publications of the Astronomical Society of Japan 59 (2007) S23.

[70] T. Takahashi et al., Publications of the Astronomical Society of Japan 59 (2007) S35.

[71] P. J. Serlemitsos et al., Publications of the Astronomical Society of Japan 59 (2007) S9.

[72] The *Suzaku* Technical Description (Version: October 2009), ISAS/JAXA and the X-ray Astrophysics Laboratory NASA/GSFC (2009), at http://www.astro.isas.jaxa.jp/suzaku/proposal/ao5/suzaku_td/

[73] H. Uchiyama et al., Publications of the Astronomical Society of Japan 61 (2009) S9.

[74] Y. Ishisaki et al., Publications of the Astronomical Society of Japan 59 (2007) S113.

[75] M. J. L. Turner et al., Astronomy and Astrophysics 365 (2001) L27.

[76] L. Stüder et al., Astronomy and Astrophysics 365 (2001) L18.

[77] J. W. den Herder et al., Astronomy and Astrophysics 365 (2001) L7.

[78] K. O. Mason et al., Astronomy and Astrophysics 365 (2001) L36.

[79] *XMM-Newton* Users Handbook (Issue 2.7), J.-U. Ness, M. Ehle et al., at http://xmm.esac.esa.int/external/xmm_user_support/documentation/uhb/index.html

[80] D. A. Schwartz et al., Proceedings of SPIE 4012 (2000) 28.

[81] G. P. Garmire et al., Proceedings of SPIE 4851 (2003) 28.

[82] S. S. Murray et al., Proceedings of SPIE 4012 (2000) 68.

[83] D. O. Pease et al., Proceedings of SPIE 4851 (2003) 157.

[84] C. R. Canizares et al., The Publications of the Astronomical Society of the Pacific 117 (2005) 1144.

[85] The *Chandra* Proposers' Observatory Guide (Version 11.0), *Chandra* X-ray Center, *Chandra* Project Science and *Chandra* IPI Teams, at http://cxc.harvard.edu/proposer/POG/html/

[86] R. J. Hanisch et al., Astronomy and Astrophysics 376 (2001) 359.

[87] http://glast-ground.slac.stanford.edu/DataPortalAstroServer/

[88] http://xmm.esac.esa.int/

[89] http://asc.harvard.edu/

[90] http://glast-ground.slac.stanford.edu/workbook/sciTools_Home.htm

[91] http://heasarc.gsfc.nasa.gov/lheasoft/

[92] http://www.astro.isas.jaxa.jp/suzaku/caldb/

[93] http://heasarc.nasa.gov/docs/xanadu/xspec/

[94] http://xmm.esac.esa.int/external/xmm_data_analysis/

[95] http://asc.harvard.edu/ciao/

[96] http://asc.harvard.edu/caldb/

[97] M. J. Keith et al., Monthly Notices of the Royal Astronomical Society 389 (2008) 1881.

[98] F. Camilo et al., Astrophysical Journal 571 (2002) L41.

[99] G. Hobbs et al., Monthly Notices of the Royal Astronomical Society 352 (2004) 1439.

[100] M. Kramer et al., Monthly Notices of the Royal Astronomical Society 342 (2003) 1299.

[101] F. Camilo et al., Astrophysical Journal 637 (2006) 456.

[102] D. R. Lorimer et al., Monthly Notices of the Royal Astronomical Society 273 (1995) 411.

[103] M. S. E. Roberts et al., Astrophysical Journal 577 (2002) L19.

[104] J. P. Halpern et al., Astrophysical Journal 552 (2001) L125.

[105] J. M. Rankin, Astrophysical Journal 405 (1993) 285.

[106] L. Zhang et al., Astronomy and Astrophysics 357 (2000) 957.

[107] K. Hirotani, Astrophysical Journal 688 (2008) L25.

[108] W. Becker and J. Trümper, Astronomy and Astrophysics 326 (1997) 682.

[109] Y. Saito, PhD Thesis submitted to University of Tokyo (1998).

[110] E. V. Gotthelf, Astrophysical Journal 591 (2003) 361.

[111] X.-H. Li et al., Astrophysical Journal 682 (2008) 1166.

[112] "Radiative Processes in Astrophysics", G. B. Rybicki and A. P. Lightman, John Wiley & Sons (1979).

[113] D. J. Thompson, et al., Astrophysical Journal 436 (1994) 229.

[114] "Classical Electrodynamics", J. D. Jackson, John Wiley & Sons (1962).

[115] S. Pineault et al., Astronomical Journal 105 (1993) 1060.

[116] D. A. Green and S. F. Gull, Nature 299 (1982) 606.

[117] D. A. Roberts et al., Astronomy and Astrophysics 274 (1993) 427.

[118] J. Faherty et al., Astrophysics and Space Science 303 (2007) 225.

[119] S. Johnston, et al., Monthly Notices of the Royal Astronomical Society 279 (1996) 1026.

[120] C.-Y. Ng et al., Astrophysical Journal 627 (2005) 904.

[121] I.-A. Yadigaroglu and R. W. Romani, Astrophysical Journal 476 (1997) 347.

[122] R. N. Manchester et al., Astronomical Journal 129 (2005) 1993.

[123] J. P. Halpern et al., Astrophysical Journal 668 (2007) 1154.

[124] H. Greidanus and R. G. Strom, Astronomy and Astrophysics 240 (1990) 376.

[125] A. Van Etten et al., Astrophysical Journal 680 (2008) 1417.

[126] F. Camilo et al., Astrophysical Journal 705 (2009) 1.

[127] J. P. Halpern et al., Astrophysical Journal 552 (2001) L125.

[128] R. Kothes et al., Astrophysical Journal 560 (2001) 236.

[129] A. Possenti et al., Astronomy and Astrophysics 387 (2002) 993.

Acknowledgments

First of all, I would like to thank my supervisor Prof. Nobuyuki Kawai for his continuous guidance and encouragements throughout my 6-year life in the lab. I am also grateful to Prof. Jun Kataoka, now in Waseda University, for his patient instruction in my experiments and report writing in my early days.

I wish to thank all members of Kawai group. Dr. Yoichi Yatsu and Dr. Takeshi Nakamori kindly helped me for data analysis, discussions and so on. I also acknowledge former members, Dr. Masaru Ueno, Tomoko Ikagawa, Yusuke Kuramoto, Takao Saito and Dr. Makoto Arimoto, for their dedicated supports and advices.

Many thanks go to the *Fermi* LAT Collaboration for their generous supports and constant efforts in the operation, the data archive and software developments. I received many supports from Prof. Tuneyoshi Kamae, Dr. Hiroyasu Tajima, Dr. Tsunefumi Mizuno, Dr. Hideaki Katagiri, Dr. Hiromitsu Takahashi, Dr. Masanori Ohno and Dr. Akira Okumura.

This work utilizes valuable X-ray observation data by *Suzaku, XMM-Newton* and *Chandra*. I acknowledge the *Suzaku* team, the *XMM-Newton* Science Operation Centre and the *Chandra* X-ray Observatory Science Center.

The author has been supported by the JSPS Research Fellowships for Young Scientists for two years since April 2008.